DISSERTATION

ROLE OF ROSSBY WAVE BREAKING IN THE VARIABILITY OF LARGE-SCALE

ATMOSPHERIC TRANSPORT AND MIXING

Submitted by

Chengji Liu

Department of Atmospheric Science

In partial fulfillment of the requirements

For the Degree of Doctor of Philosophy

Colorado State University

Fort Collins, Colorado

Fall 2017

Doctoral Committee:

Advisor: Elizabeth A. Barnes

Thomas Birner
George N. Kiladis
Wayne H. Schubert
Karan Venayagamoorthy

ABSTRACT

ROLE OF ROSSBY WAVE BREAKING IN THE VARIABILITY OF LARGE-SCALE

ATMOSPHERIC TRANSPORT AND MIXING

We demonstrate that Rossby wave breaking (RWB) plays an important role in both horizontal and vertical large-scale transport/mixing in both observations and idealized general circulation models. In the horizontal direction, RWB contributes to a substantial fraction of transient moisture flux into the Arctic. In the vertical direction, RWB modifies thermal stratification near the tropopause which leads to enhanced mass exchange across the tropopause.

In understanding the variability of RWB related transport and mixing, we show that it is essential to separate the two types of RWB – anticyclonic wave breaking (AWB) and cyclonic wave breaking (CWB) – for two fundamental differences between them. The first difference is the opposite relationship between jet positions and their frequencies of occurrence. For both horizontal transport of moisture into the Arctic and vertical mixing of ozone across the tropopause, the robust relationship between jet position and AWB/CWB frequency is of first order importance in explaining the large-scale transport/mixing anomaly patterns influenced by climate variabilities involving jet shifting, such as the El-Niño Southern Oscillation (ENSO) and the North Atlantic Oscillation (NAO).

The second robust difference is the mixing strength exhibited by individual AWB and CWB events. In idealized lifecycle and climate simulations, as well as reanalysis data, CWB consistently exhibits stronger mixing strength than AWB. Combined with the robust relationship between jet variability and AWB/CWB frequency, such a difference is demonstrated to translate into a decrease in total upper troposphere diffusivity as the jet shifts poleward in an idealized climate simulation.

ACKNOWLEDGMENTS

I wish first to thank my advisor, Libby Barnes, for infectious enthusiasm, unlimited inspiration and encouragement throughout my graduate studies. I thank my thesis committee, Thomas Birner, George Kiladis, Wayne Schubert, and Karan Venayagamoorthy for insightful discussions and constructive comments on the thesis work. Much support is provided by Matt Bishop, Mostafa El-Kady, and Ammon Redman on computational problems. I also thank my fellow students for many memorable discussions about both research and life. Special thanks to Marie for being a great officemate and Bryan for the help with Python and many more. Thank you all for making my stay at CSU enjoyable. Lastly, I wish to thank my family, my parents and my wife, for all the unconditional support along the way.

TABLE OF CONTENTS

CHAPTER 1

INTRODUCTION

Tropospheric Rossby waves have horizontal scales of a few thousand kilometers and lifespans of a few days. These Rossby waves break at the late stage of their lifecycle which leads to intensive large-scale irreversible transport and mixing (e.g. Thorncroft et al. 1993; Stone et al. 1999; Polvani and Esler 2007). Since the breaking of Rossby waves occurs ubiquitously in the mid-to-high latitudes on a daily basis, it plays an important role in distributing various constituents globally.

There are two types of Rossby wave breaking (RWB) – anticyclonic wave breaking (AWB) and cyclonic wave breaking (CWB), and the frequency of each is strongly coupled to the midlatitude eddy-driven jet stream. Climatologically, AWB occurs most frequently on the equatorward flank of the jet where the horizontal wind shear is anticyclonic, while CWB occurs most frequently on the poleward flank of the jet. As the jet shifts poleward, the frequency of AWB increases whereas that of CWB decreases and vice versa (e.g. Strong and Magnusdottir 2008; Woollings et al. 2008; Rivière 2011; Barnes and Hartmann 2012). This RWB-jet position relationship is especially important because the jet stream position is very responsive to both internal climate variability such as the El-Niño Southern Oscillation (ENSO) (e.g. Rasmusson and Wallace 1983; Chen and van den Dool 1999; Ren et al. 2008), and external climate forcings such as increasing greenhouse gas concentrations and ozone depletion (e.g. Thompson and Solomon 2002; Butler et al. 2010; Barnes and Polvani 2013). It is through such coupling that RWB is linked to climate variability on different time scales, and thus, drives the variability of global transport and mixing of various chemical tracers.

Studying the transport and mixing associated with AWB and CWB separately is thus key to understanding the variability of the climate-scale distribution of various chemical tracers. To serve this purpose, a dedicated wave breaking detection algorithm (Liu et al. 2014) is used throughout the thesis to identify the two types of wave breaking based on the overturning direction of potential vorticity (PV) contours. By using this algorithm, both composite behavior of the two types of wave breaking and the variability of their occurrence can be quantified.

Quantifying large-scale transport/mixing linked to Rossby waves can be challenging because wavy motions involve largely reversible transport/fluxes. Averaging these reversible fluxes in an Eulerian coordinate introduces artifacts associated with "Stokes drift" (e.g. McIntyre 1980). To avoid these issues, a Lagrangian framework (Nakamura 1995, 1996) is adopted and modified to accurately quantify irreversible mixing linked to RWB in idealized general circulation models.

The transport and mixing associated with Rossby wave breaking occurs approximately along sloped isentropic surfaces (e.g. Shapiro 1980; Thorncroft et al. 1993; Madonna et al. 2014), involving both horizontal and vertical directions. Two chapters of this thesis specifically address these two directions. In particular, Chapter 2 studies the horizontal transport of moisture into the high latitudes and the role Rossby wave breaking plays. Chapter 3 explores the mechanisms through which Rossby wave breaking modifies the thermal stratification near the tropopause and how that influences the vertical mass exchange across the tropopause.

Not all RWB events are created equal. AWB and CWB exhibit strikingly different mixing strength in idealized lifecycle simulations (Polvani and Esler 2007). Focusing on this potential asymmetry, in Chapter 4 we carry out an idealized climate simulation to quantify the isentropic

mixing linked to the two types of wave breaking, for both horizontal and vertical directions. Furthermore, we demonstrate how such an asymmetry can translate into a dependence of total large-scale mixing strength on jet stream variability.

In observations, Rossby wave breaking has been shown to be responsible for extreme ozone concentration in the mid-to-upper troposphere over several days (e.g. Shapiro 1980; Holton et al. 1995; Appenzeller et al. 1996a), but its role in ozone variability on much longer time scales remains unknown. Building on the results from the previous chapters, in Chapter 5 we investigate the role of Rossby wave breaking in low-frequency variability of upper-troposphere ozone using reanalysis ozone data. We focus on month-to-month variability related to the jet shifting and interannual variability influenced by the El-Niño Southern Oscillation (ENSO).

The individual chapters in this thesis correspond to peer-review articles – either published, under review, or in preparation. Therefore, each chapter in this thesis contains a separate introduction to the specific topics addressed. Specifically, Chapter 2 corresponds to Liu and Barnes (2015), Chapters 3 and 4 correspond to Liu and Barnes (2017b) and Liu and Barnes (2017a) respectively, which are both under review. Chapter 5 is in preparation and will be submitted in a few months.

CHAPTER 2

EXTREME MOISTURE TRANSPORT INTO THE ARCTIC LINKED TO ROSSBY
WAVE BREAKING

2.1. INTRODUCTION

The Arctic surface has been warming at a much faster rate than the global average over the past
decades, and this phenomenon is known as "Arctic amplification" (e.g. Chapman and Walsh 1993;
Bekryaev et al. 2010). Climate models project continued Arctic amplification in the future as a
response to greenhouse gas increases (e.g. Holland and Bitz 2003; Hansen et al. 2005). Although
a surface-albedo feedback may play a role in this amplified warming (e.g. Manabe and Wetherald
1975; Manabe and Stouffer 1980), some studies also highlight longwave radiation as another po-
tential culprit (e.g. Winton 2006; Graversen and Wang 2009). As a strong greenhouse gas, water
vapor traps a fraction of outgoing longwave radiation and hence acts to warm the Arctic surface
(e.g. Curry et al. 1995; Francis and Hunter 2006). In addition, water vapor can influence the for-
mation of low-level clouds in the Arctic. On synoptic time scales, these clouds can significantly
influence the longwave radiation reaching the ground and cause warmer Arctic conditions (e.g.
Stramler et al. 2011). In addition to these radiative effects, water vapor can also impact the Arctic
climate through precipitation. The changes in Arctic precipitation can modify the snowfall onto
the nearby continents and ice sheets (Singarayer et al. 2006; Liu et al. 2012), and freshen the sea
water. These changes have a potential to influence the Atlantic meridional overturning circulation
(AMOC) which has a global impact on climate (Kattsov and Walsh 2000; Davies et al. 2014).

On synoptic time scales, variations of the Arctic water vapor are driven by weather systems
transporting moisture from lower latitudes (Rinke et al. 2009; Doyle et al. 2011). Newman et al.

(2012) split the moisture transport into time mean and transient components, showing that the pole-ward transport is dominated by the transient part which is frequently associated with "atmospheric rivers". Of the transient part, they demonstrate that the synoptic transport with periods less than 10 days is important in the mid-to-high latitudes over the two Northern Hemisphere ocean basins. Woods et al. (2013) evaluated the importance of the synoptic transport by identifying extreme moisture intrusions across 70°N, and concluded that they account for 36% of the total transport into the Arctic. These studies combined highlight the importance of extreme synoptic transport events for Arctic water vapor variability.

Extreme moisture transport into the Arctic is associated with a "blocking-like" atmospheric circulation pattern (Woods et al. 2013), which is closely related to Rossby wave breaking (RWB) (e.g. Pelly and Hoskins 2003; Berrisford et al. 2007; Barnes et al. 2012; Masato et al. 2012). RWB in idealized simulations exhibits rapid large-scale transport and mixing on synoptic time scales (Polvani and Esler 2007). In fact, the linkage between "atmospheric rivers" and RWB has been investigated recently over the North Pacific (Ryoo et al. 2013; Payne and Magnusdottir 2014). Al-though these studies focused on the subtropics, their results suggest a possible relationship between extreme moisture transport into the Arctic and RWB events which are abundant in the mid-to-high latitudes (e.g. Strong and Magnusdottir 2008; Liu et al. 2014).

In this study, we aim to explore this possible connection between RWB and moisture trans-port and quantify the importance of RWB events in contributing to the extreme moisture transport into the Arctic. Previous studies have documented that the two types of RWB – anticyclonic wave breaking (AWB) and cyclonic wave breaking (CWB) – have strong but different relation-ships with the midlatitude jet streams (e.g. Strong and Magnusdottir 2008; Woollings et al. 2008; Rivière 2011; Barnes and Hartmann 2012). AWB generally occurs more frequently when the jet

is shifted poleward, and CWB generally occurs more frequently when the jet is shifted equatorward. Given this relationship, one might expect jet variability to explain a significant fraction of the moisture transport variability associated with RWB. One might also expect a high correlation between this transport and the major atmospheric teleconnections involving jet variability, such as the El-Niño/Southern Oscillation (ENSO), and the North Atlantic Oscillation (NAO). We explore these relationships here.

We organize the chapter as follows. A general description of the data and methods is given in section 2.2. Section 2.3 quantifies the importance of extreme moisture transport events and their associated circulations. In Section 2.4, we introduce an algorithm to quantify the moisture flux contributed by RWB, and present the spatial pattern of RWB-related transport and its seasonality. Section 2.5 explores the impacts of atmospheric teleconnections (ENSO and NAO) on the interannual variability of RWB-related transport into the Arctic. Conclusions and a brief discussion will be given in Section 2.6.

2.2. DATA AND METHODS

In this study, we use the 6-hourly Modern-Era Retrospective Analysis for Research and Applications (MERRA) reanalysis data (Rienecker et al. 2011), with a horizontal spatial resolution of $1.25° \times 1.25°$ and 17 vertical levels. Specifically, we analyze the horizontal wind (u,v), temperature (T), and specific humidity (q) over the period from Jan. 1979 to Dec. 2010. To test the sensitivity of our results to the reanalysis data, we have also repeated our analysis with ERA-interim data (Dee et al. 2011) from the European Centre for Medium-Range Weather Forecasts (ECMWF) for the period from Jan. 2006 to Dec. 2010. The results are nearly identical to those obtained from MERRA, and thus we conclude that our results are insensitive to the choice of reanalysis data, and only show those obtained from MERRA here.

In this study, we use "moisture" to mean water vapor only, and thus, we do not include any water in the liquid phase (e.g. cloud and precipitation). To calculate the vertically integrated poleward moisture transport, we use the following formula:

$$\langle v'q' \rangle = \frac{100}{g} \int_{1000}^{0} v'q'dp \qquad (2.1)$$

where the angle bracket denotes the mass weighted vertical integration, and p is the pressure in hPa. The prime denotes anomalies, defined as the deviation from the climatological mean, which is itself defined as the 365-day-calendar-mean smoothed with a 20-day moving average window. We focus here on the transient transport because we are specifically interested in connecting extreme moisture transport with transient RWB events. Additionally, we focus only on positive v' and positive q' fluxes. The reason for this focus on positive poleward moisture flux is that we are most interested in fluxes of moist air into the Arctic ($v' > 0$, $q' > 0$) rather than fluxes bringing dry air out of the Arctic ($v' < 0$, $q' < 0$). While the latter is important in terms of the energy budget, the former is the component that matters in terms of the moisture content and hence the radiative effects of water vapor. As for the equatorward moisture transport ($v'q' < 0$), Serreze et al. (1995) shows that this term is small in the climatological mean. We will further justify in Section 2.3 that transient equatorward moisture transport is much less intense than its poleward counterpart. Unless otherwise stated, we will use the phrase "poleward moisture transport" in this article to mean $\langle v'q' \rangle$ with positive v' and positive q'.

The NAO index used in this study is obtained from the National Oceanic and Atmospheric Administration (NOAA) Climate Prediction Center (Barnston and Livezey 1987). The Niño 3.4 index is used to quantify ENSO variability and calculated from the Hadley Center HadISST sea surface temperature (SST) data as the averaged SST anomaly over 170°W-120°W, 5°S-5°N.

To quantify the contribution of Rossby wave breaking to the poleward moisture transport, we require a way to identify RWB in the reanalysis. Here, RWB events are identified with the Rossby wave identification algorithm of Liu et al. (2014), which is based on Strong and Magnusdottir (2008). Here a brief description is provided. Using 6-hourly MERRA reanalysis data, we first interpolate the potential temperature on the 2 PVU surface (surface with constant potential vorticity of 2 potential vorticity units) which is an approximation for the tropopause in the mid-to-high latitudes. When there is a vertical tropopause fold, we use the uppermost point for interpolation. On the 2 PVU surface, if the potential temperature contours (ranging from 300K to 350K with an interval of 5K) overturn beyond a certain threshold (the overturning contour encloses an area S more than 25 degrees in an equirectangular projection), a RWB event is identified and the center of the event is defined as the centroid of the area S enclosed by the overturning contour. An equivalent length r_e is used to quantify the size of the RWB event and is defined as the radius of a circle with area S. That is, $r_e = \sqrt{S/\pi}$. When multiple overturning contours are associated with the same RWB event, we only record the contour that overturns the farthest. We classify RWB event as either anticyclonic wave breaking (AWB) or cyclonic wave breaking (CWB) according to the direction of the overturning. For additional details of the algorithm, please refer to Strong and Magnusdottir (2008), or Liu et al. (2014).

2.3. EXTREME EVENTS OF POLEWARD MOISTURE TRANSPORT

Figure 2.1a shows a snapshot of the extreme poleward moisture transport event that occurred to the southwest of Greenland on Jan 22, 2007. The maximum transient moisture flux exceeds $600\text{kg·m}^{-1}\text{·s}^{-1}$, which is about 30 times that of the climatological mean transient flux in this region. To further investigate the statistics of the extremes in this region, we average the 6-hourly total transient moisture transport over the small sector near this event indicated by a black line
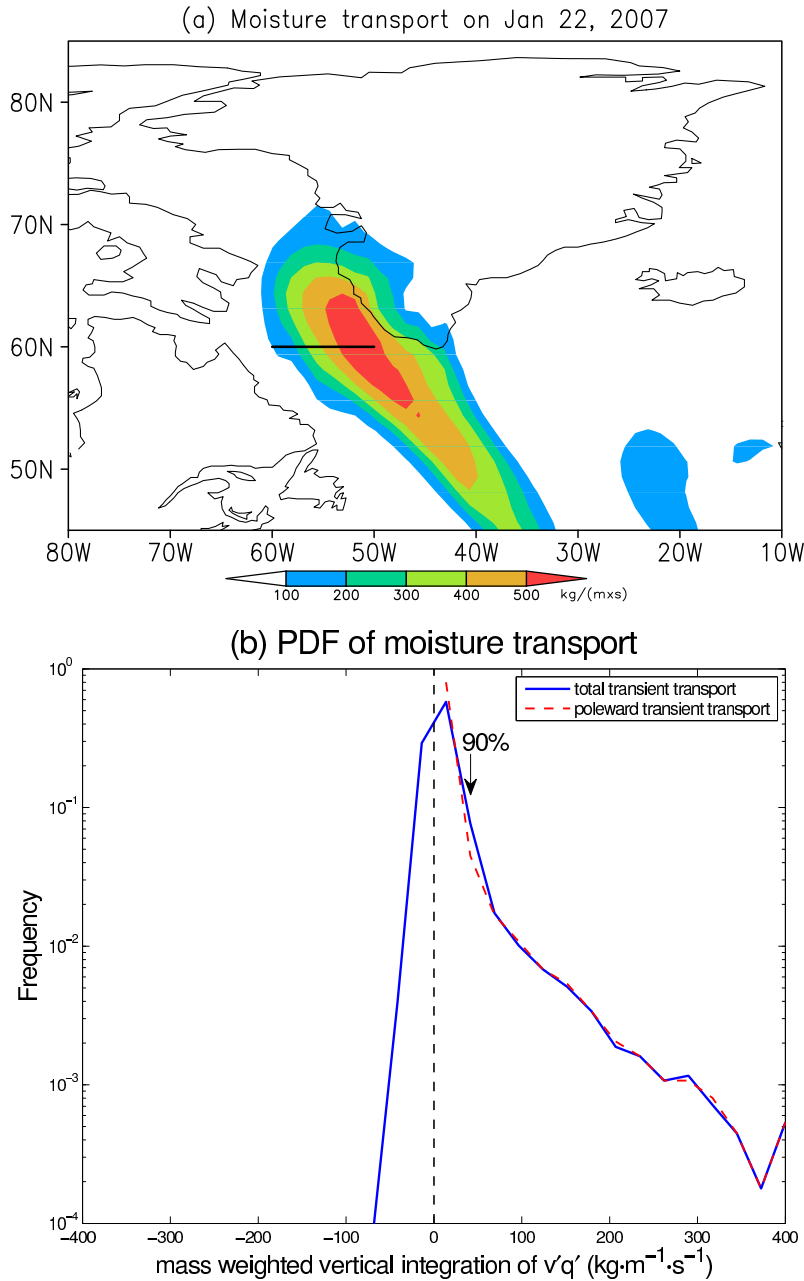
FIG. 2.1. (a) Transient poleward moisture transport on January 22nd, 2007. (b) Normalized probability distribution of the total transient meridional moisture transport (blue solid line) across a 10-degree-longitude line to the southwest of Greenland (indicated by a black solid line in panel (a)). The contribution due to the transient poleward transport ($v' > 0$, $q' > 0$) only is plotted as a red dashed line. Note that the ordinate is logarithmic.

in Figure 2.1a, and show its frequency distribution in Figure 2.1b (blue line). (Note that v' and

q' are not restricted to positive values for this calculation.) There is substantial asymmetry in

the frequency distribution in that positive transports are stronger overall than negative ones. The frequency distribution of the negative transport follows a normal distribution while that of the positive transport has a heavy tail corresponding to the extreme events like the one shown in Figure 2.1a. The average duration of these extreme events (defined as the amount of time the 6-hourly fluxes stay above the 90th percentile continuously) is about one day.

The heavy positive tail in the histogram suggests the importance of extreme events in the total poleward moisture transport. Furthermore, these extreme transport events are due almost entirely to poleward moisture transport with positive v' and q' only (red line in Figure 2.1b). The red line is almost indistinguishable from the blue line on the right tail of the distribution, indicating that these extreme transport events are mostly due to the poleward transport of anomalously moist air, rather than the equatorward transport of anomalously dry air. We have made similar distributions for the northeast Atlantic and the North Pacific across 60°N and the main features are similar (not shown). These results suggest that at the high latitudes, transient moisture transport into the Arctic can be very intense while the transient transport of dry air out of the Arctic occurs during much weaker events. This further justifies our use of positive v' and q' to study the extreme moisture transport into the Arctic.

To quantify the importance of these extreme transport events, we calculate the contribution of extreme transient poleward moisture transport as a fraction of the total transient poleward moisture transport and plot it in Figure 2.2. Specifically, we define "extreme" as the 90th percentile fluxes of $v'q'$ for $v' > 0$, $q' > 0$ at each grid point (similar to Figure 2.1b). We sum up the fluxes of $v'q'$ greater than this extreme threshold and divide it by the sum of all $v'q'$ fluxes at each grid point. Over the entire Northern Hemisphere in Figure 2.2, extreme events account for at least 40% of the total transient poleward transport in either season. The striking feature in Figure 2.2, however, is

Extreme moisture transport
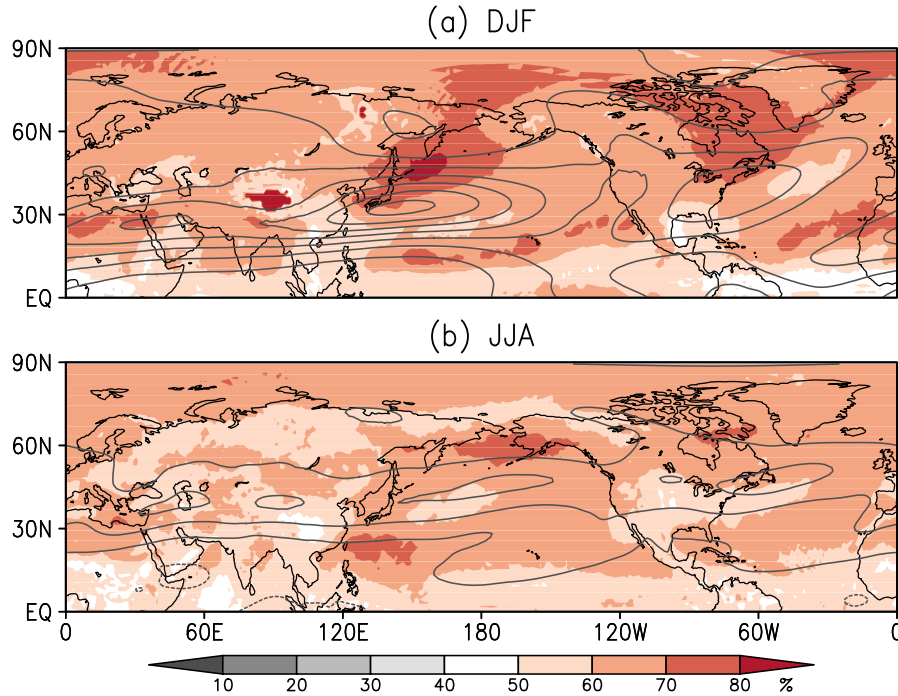(fraction of total transient transport)

(a) DJF

(b) JJA

FIG. 2.2. Contribution fraction of the the 90th percentile of transient poleward moisture transport to the total transient transport ($v' > 0$, $q' > 0$) in (a) DJF (b) JJA. Contours denote the zonal wind at 300hPa, with a contour interval of 10m/s.

that in both winter and summer, extreme transport events account for more than 60% of the total poleward moisture transport in most of the mid-to-high latitudes. Focusing on the high latitudes, extreme events account for 69% of the total transient poleward moisture transport across 60°N in winter and 66% in summer. The 300hPa zonal wind is also plotted in Figure 2.2 as contours. Note that the largest fractions tend to occur on the flanks of the jet streams over the North Pacific and the North Atlantic. This is the location of most frequent synoptic Rossby wave breaking, and we will demonstrate that this extreme transport is linked to synoptic wave breaking events in the next section.

Note that Figure 2.2 shows transient transport ($v'q'$) only, however, the contribution of the extremes to the total poleward moisture transport (vq) as calculated by Woods et al. (2013) is not
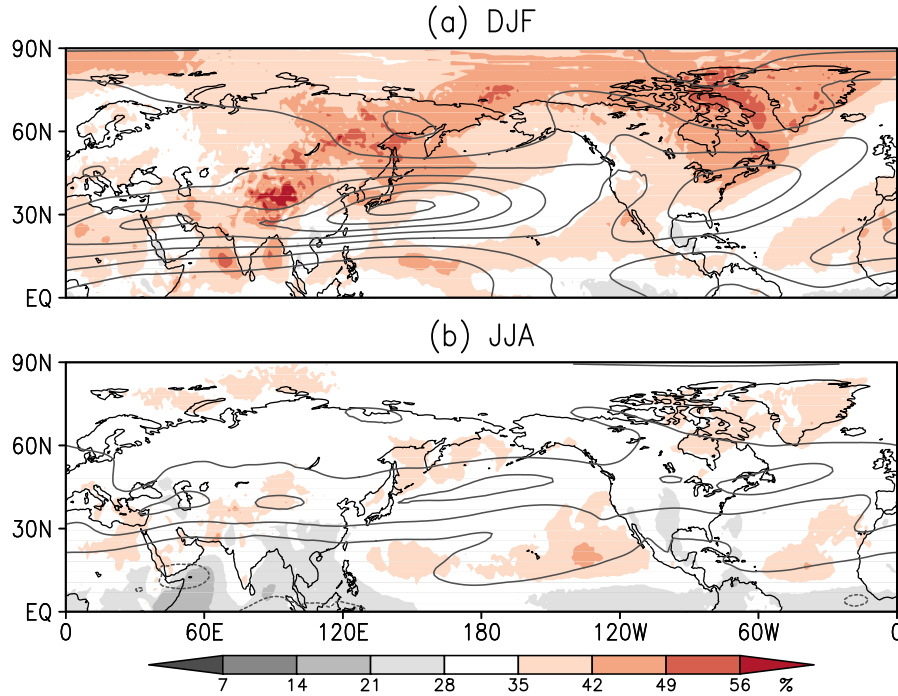
Fig. 2.3. Contribution fraction of the 90th percentile of poleward moisture transport to the total transport ($vq > 0$) in (a) DJF (b) JJA. Contours denote the zonal wind at 300hPa, with a contour interval of 10m/s.

immediately evident from this figure. For ease of comparison with previous studies (e.g. Woods et al. 2013), Figure 2.3 shows the contribution of extreme positive vq as a fraction of total positive vq. In this case, "extreme" is defined as the 90th percentile fluxes of positive vq at each grid point. Thus, Figure 2.3 shows the sum of the fluxes of vq greater than this extreme threshold divided by the sum of all of the positive vq fluxes. The fractional contribution of extremes to the total is lower compared to that in Figure 2.2, but they are still a significant contribution to the total. Focusing on the high latitudes, extreme events account for 38% of the total poleward moisture transport across 60°N in winter and 32% in summer. This value agrees well with Woods et al. (2013), where they found 36% for winter. The general differences between winter and summer are larger in Figure 2.3 than that in Figure 2.2, possibly because the mean meridional circulation (which is included in

Figure 2.3 but not in Figure 2.2) is stronger in summer and hence contributes more to the moisture transport.

In Woods et al. (2013), the circulation associated with extreme moisture transport into the Arctic bears a resemblance to that of RWB events. Here, we wish to demonstrate this linkage between extreme poleward moisture transport and RWB. Rossby wave breaking in the troposphere usually occurs near the tropopause and is identified as overturning potential temperature contours on the dynamical tropopause (the 2 PVU surface). So, we plot the potential temperature on the 2 PVU surface (black contours) in Figure 2.4 composited on times of extreme (stronger than the 90th percentile) poleward moisture transport across 60°N over various longitudinal sectors (thick horizontal black lines). The shading shows the corresponding composites of the extreme poleward moisture transport. The overturning of potential temperature contours is evident in all three examples and is especially striking considering the large sample size for each composite (more than 900 time steps). In Figure 2.4a, extreme transport to the southwest of Greenland [60°W-50°W] is associated with CWB over the northwest Atlantic. (Note that the thick black line in Figure 2.4a is identical to the one in Figure 2.1a). In Figure 2.4b, extreme transport into the Norwegian Sea [30°W-10°W] is coupled to AWB over the northeast Atlantic. The moisture fluxes also exhibit a southwest-northeast tilt that follows the potential temperature contours. Finally, Figure 2.4c shows the extreme transport into the Arctic through the Bering Strait [180°-160°W] and the associated CWB off the coast of Alaska. All of these composites are consistent with the orientations of RWB events occurring in these regions in the climatology. Namely, over the North Atlantic, CWB typically occurs off of the coast of Greenland and AWB tends to occur over Europe (e.g. Strong and Magnusdottir 2008). Over the North Pacific, CWB dominates the high latitudes while AWB tends to occur in the northeastern Pacific and near the west coast of North America (e.g. Liu et al. 2014).
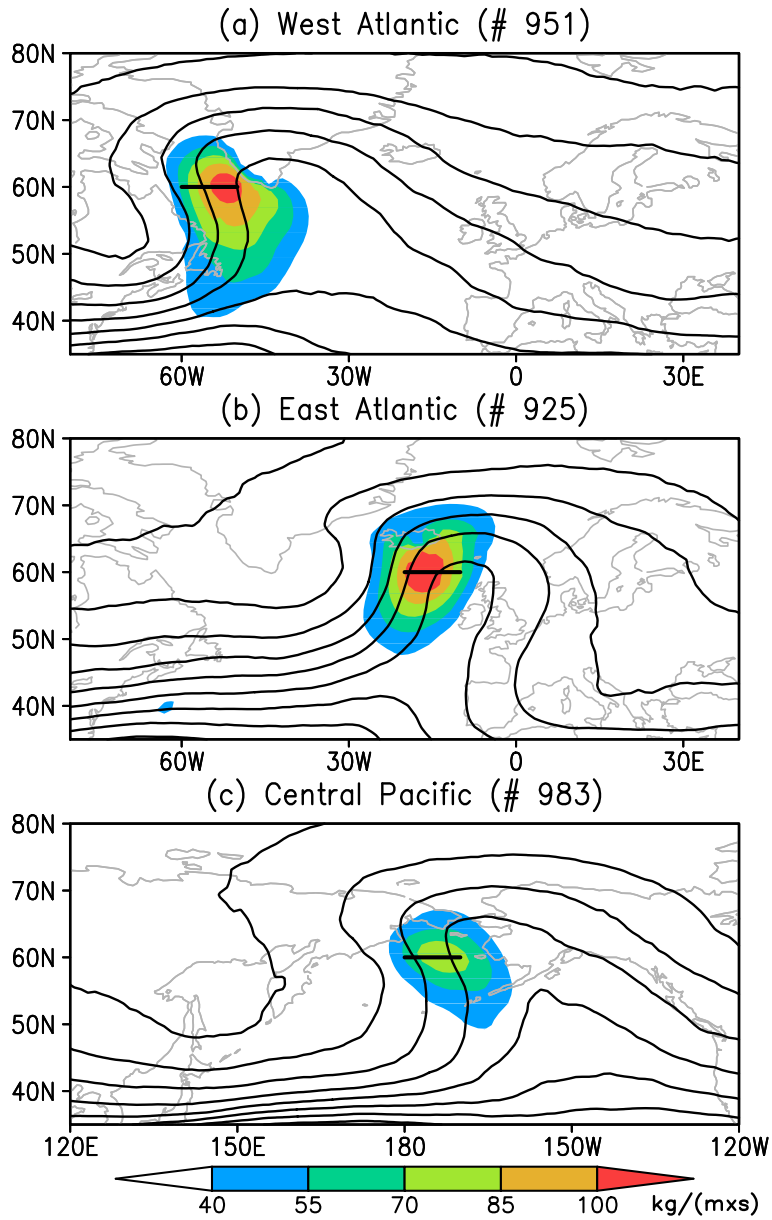
FIG. 2.4. Composite variables for extreme (greater than the 90th percentile) transient poleward moisture transport across 10-degree-longitude bins at 60°N indicated by the black straight lines for the (a) west Atlantic (60°W∼50°W), (b) east Atlantic (20°W∼10°W), (c) central Pacific (180°W∼170°W). The moisture transport is denoted by shading and potential temperature on the 2 PVU surface is denoted by contours. The number of 6-hour timesteps in each composite is denoted in the title of each panel.
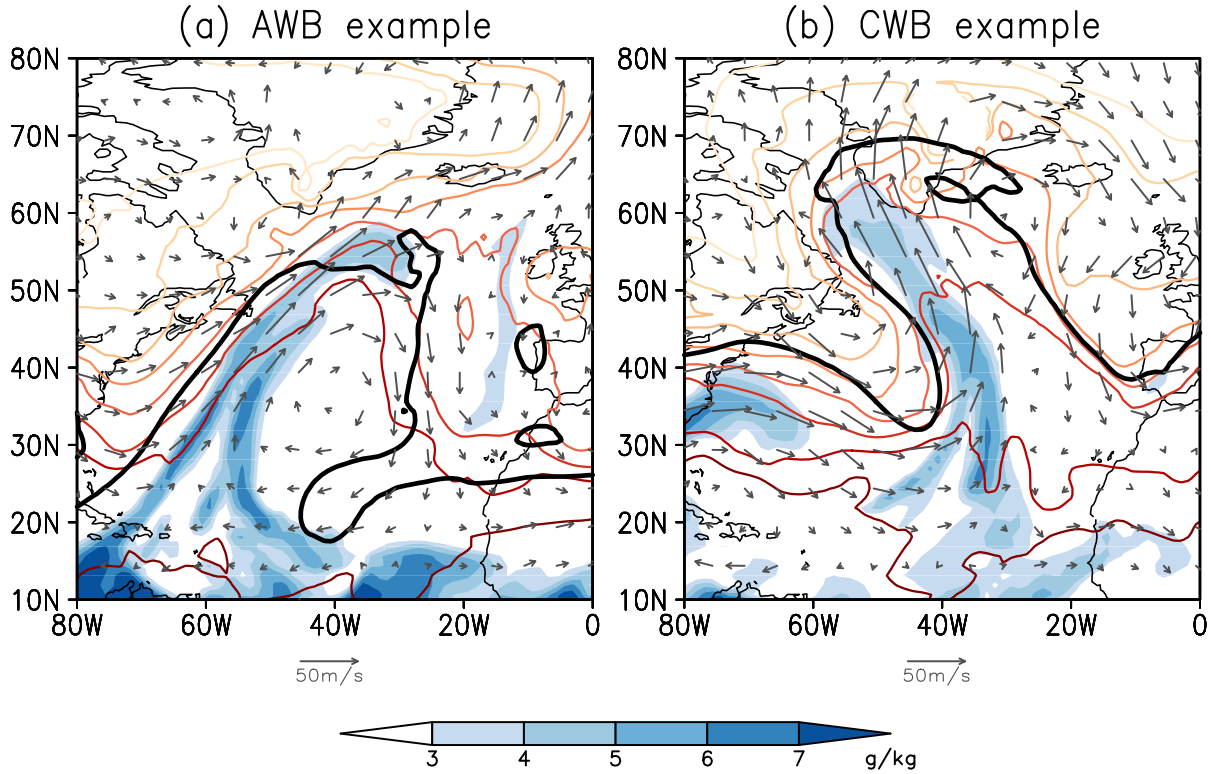
FIG. 2.5. Mixing ratio of water vapor (shading), potential temperature (colored contours), and horizontal wind (arrows) on 700 hPa for (a) an anticyclonic wave breaking on Jan 8, 2006, and (b) a cyclonic wave breaking on Jan 22, 2007. The potential temperature contour interval is 5 K. The thick solid black line is the potential temperature contour on the 2 PVU surface that is used to identify Rossby wave breaking events.

Finally, we end this section with a brief discussion of the basic synoptic situation associated with RWB-related extreme moisture transport. Figures 2.5a-b show two snapshots of wind, temperature and moisture concentration at lower levels during two RWB events. Over the North Atlantic, the strongest winds to a large extent lay along the potential temperature contours on the 2PVU surface. Intense southwesterlies during the AWB event and southeasterlies during the CWB event bring moisture from the subtropics all the way to the high latitudes. The transport paths sit within relatively warm tongues, which prevent a substantial loss of water vapor due to condensation. Further lead-lag centered composites with respect to the size of the RWB event indicate that extreme

moisture transport is typically associated with large RWB events and peaks at the mature phase of RWB when the contours overturn farthest (figures not shown).

2.4. CONTRIBUTION OF ROSSBY WAVE BREAKING

In the previous section, we demonstrated that the bulk of poleward moisture transport is driven by extreme transport events, and composite analysis suggests that at the high latitudes, these extremes are closely related to Rossby wave breaking (RWB). The aim of this section is to quantify this RWB-related transport and to document its seasonality.

Synoptic RWB usually occurs at the late stage of the baroclinic Rossby wave life cycle in the mid-to-high latitudes (Thorncroft et al. 1993), and typically persists for approximately one to five days. Before the breaking begins, a Rossby wave usually has already started to transport moisture poleward (figures not shown). However, it is at the breaking stage that the transport is strongest during the whole life cycle. This is suggested by Figure 2.4. If poleward moisture transport was not maximized during the wave breaking phase, then the composite circulation for the strongest poleward moisture transport (Figure 2.4) would not show a clear RWB pattern. Therefore, this study only focuses on the extreme transport due to breaking waves, but we note that it omits moisture transport associated with other stages of the baroclinic wave life cycle.

2.4.1. ALGORITHM

To quantify the poleward moisture transport due to RWB, we develop an algorithm based on potential temperature contours and the moisture transport field. First, the algorithm only considers the extreme transport stronger than the 90th percentile at each grid point. Second, if a tongue of extreme transport overlaps a potential temperature contour associated with a breaking Rossby wave, the tongue is considered associated with the RWB. The algorithm is illustrated in Figures

2.6a-b for the two case studies already shown in Figure 2.5. An AWB event is evident on Jan 8, 2006 off the coast of Canada (grey contours in Figure 2.6a). At the same time, a tongue of poleward moisture transport (shading) is seen to the west of this AWB. A similar setup is seen in Figure 2.6b for a CWB over the mid-Atlantic. We link AWB and CWB with the extreme transports by identifying their respective overturning segments that intersect the extreme transports. These intersecting contour segments are colored red in the figure. For AWB, the intersecting contour segments are extended from the top of the AWB event to $2 \times r_e$ (r_e is the equivalent length depicting the size of RWB as discussed in Section 2.2) in the zonal direction (Figure 2.6a). As suggested by Figure 2.6, the size of the moisture tongue is proportional to the size of RWB, so we also make the length of the intersecting contour proportional to the size of AWB. The choice of this specific length ($2 \times r_e$) is to some extent subjective, but we have confirmed that our results are not sensitive to the moderate variations of this parameter. For CWB, the intersecting contour is the part that indicates a reversed meridional potential temperature gradient (Figure 2.6b), and its length is proportional to the size of CWB by construction. For both types of RWB, if any part of the moisture tongue overlaps with the intersecting segment, then the whole tongue is considered to be associated with the RWB. For ease of identification, the moisture fluxes identified as linked to RWB are contoured in black in Figures 2.6a-b.

In our algorithm, the selection of intersecting contour segments is based on the assumption that extreme poleward moisture transport occurs to the west of the high potential temperature (low PV) branch of the RWB. Figures 2.6a-b exhibit transports consistent with this assumption in two case studies. To confirm these features are common to most RWB events, we plot the composite poleward moisture transport and potential temperature with respect to RWB over the North Atlantic in Figures 2.6c-d. Before compositing, we shift the fields horizontally so that their
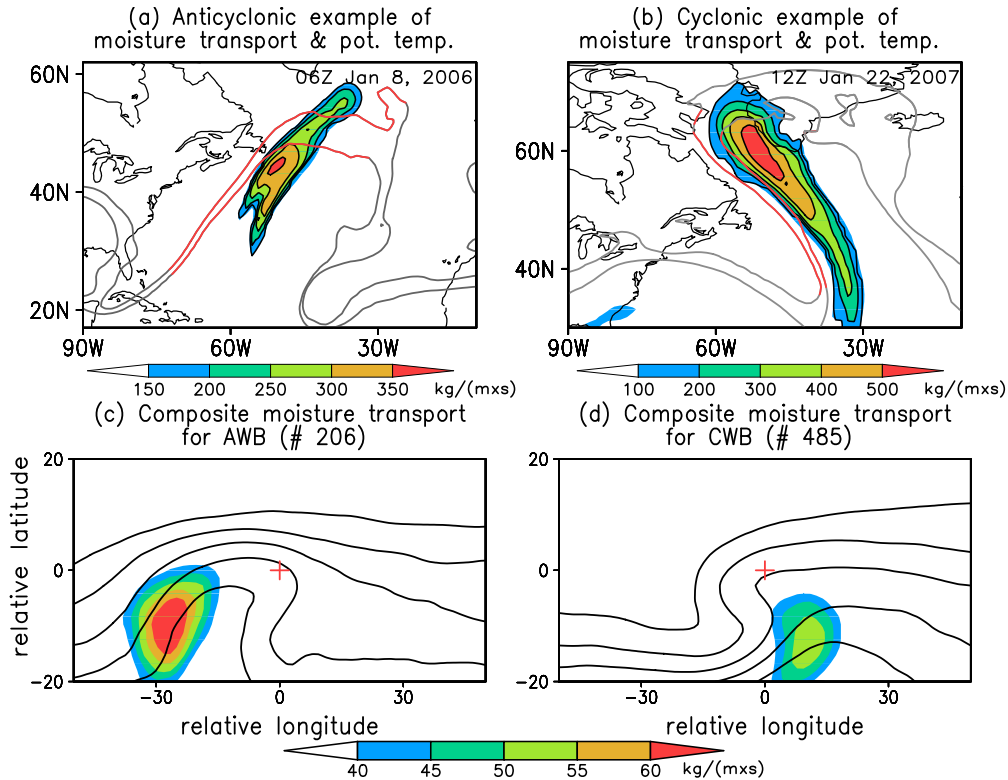
FIG. 2.6. **Upper:** Snapshots of transient poleward moisture transport (shading) and the potential temperature on the 2 PVU surface (grey contour) on (a) January 8, 2006, and (b) January 22, 2007. The red segments of the contours are those used to identify moisture transport associated with RWB in the algorithm. **Bottom:** Northern Atlantic centered composite moisture transport (shading) and potential temperature on the 2 PVU surface (black contour) for RWB events, specifically (a) anticyclonic wave breaking, (b) cyclonic wave breaking. The point (0,0) is indicated by a red cross and corresponds to the centroid of the RWB events. The number of 6-hour timesteps in each composite is denoted in the title of each panel.

corresponding RWB centroids (red crosses in Figures 2.6c-d) overlap. Therefore, the composites

are shown in a coordinate with relative longitude and relative latitude with respect to the RWB

centroid. The similarity between the upper row and the bottom row in Figure 2.6 shows that

our algorithm is based on a robust feature that extreme poleward moisture transport occurs to

the west of the high potential temperature (low PV) branch of RWB. This feature is consistent

with Woods et al. (2013), where they comment that the extreme moisture transport into the Arctic

typically occurs on the west side of a high pressure anomaly (low PV). This is also consistent with

the circulation flow pattern, in that the anomalous poleward flow is strongest to the west of an anomalous anticyclone. Furthermore, the composites in Figure 2.4 and the composites in Figures 2.6c-d are strikingly similar. Note the former composites are with respect to moisture transport while the latter composites are with respect to RWB. The former composites indicate that when extreme moisture transport occurs, the circulation pattern is similar to that of RWB. The latter composites show that when RWB begins, the corresponding poleward moisture transport is likely to be extreme. This further supports the connection between extreme moisture transport and RWB.

Note that in our algorithm the RWB events are identified near the tropopause (the 2 PVU surface), while we know that moisture transport is strongest in the lower troposphere (e.g. Serreze et al. 1995). Although RWB events are most easily defined near the tropopause, their impacts can actually penetrate to the lower troposphere and their associated circulation is equivalent-barotropic. This equivalent-barotropic nature was previously shown by Liu et al. (2014).

To further confirm the utility of our coupling algorithm, we perform a bootstrap test. The null hypothesis is that RWB has no dynamical link to the extreme poleward moisture transport, and that our algorithm is not useful and just randomly samples the moisture transport field. To test this null hypothesis, we randomly re-order the wave breaking field (potential temperature), and then apply the algorithm. If our algorithm just randomly samples the moisture fluxes, this re-ordering should produce similar results to what we will present in the subsequent sections. However, by comparing the climatological mean of moisture transport obtained by this randomly re-ordering (random case) with the original one, we find them different over almost all regions at a significance level of 0.01 (figures not shown). Specifically, the random RWB-related transport significantly underestimates the contribution over most areas due to the lack of coupling between RWB events and moisture

Extreme moisture transport in DJF

(a) Total transport

(b) RWB contribution

(c) AWB contribution

(d) CWB contribution
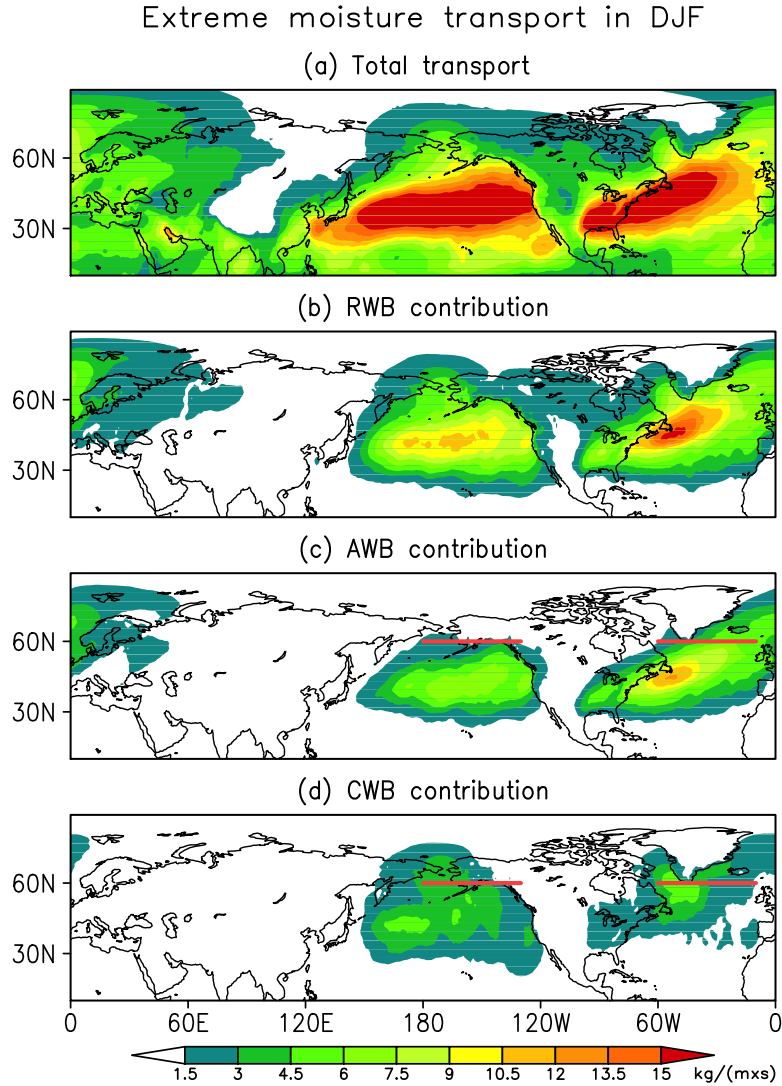
FIG. 2.7. Mean winter (a) total extreme (greater than the 90th percentile) transient poleward moisture transport, and (b) extreme transport associated with Rossby wave breaking (RWB). (c) The same as in (b), but for anticyclonic RWB (AWB) only. (d) The same as in (b), but for cyclonic RWB (CWB) only.

transport. This result not only lends support to our algorithm but also further confirms the coupling between RWB and extreme moisture transport.

2.4.2. SPATIAL DISTRIBUTION

Using the algorithm described above, we quantify how much of the extreme (stronger than the 90th percentile at each grid point) poleward moisture transport is linked to RWB. Recall that

although the extreme transport accounts for only 10% of the total *occurrence* of moisture transport, it accounts for more than 60% of the total *amount* in the mid-to-high latitudes (Figure 2.2).

Figure 2.7 provides a summary of the results for winter (DJF). Figure 2.7a shows that the total extreme poleward transport is strongest in midlatitudes over the two ocean basins where moisture is abundant and synoptic waves are most active. In the high latitudes (poleward of 60°N), there are three main regions where extreme transport maximizes: (1) over the North Pacific around the Bering Strait [170°E-160°W], (2) to the southwest of Greenland near Baffin Bay [60°W-50°W], and (3) from the Norwegian Sea to Scandinavia [30°W-10°E]. Note that these three regions are the same regions on which our composites in Figure 2.4 are based.

The clear overturning of potential temperature contours in Figure 2.4 suggests the dominant role RWB plays in extreme transport in these regions. Figure 2.7b confirms this dominance by showing the contribution of RWB to extreme transport. The RWB-related extreme transport is very similar to the total extreme transport (Figure 2.7a) in the high latitudes. In the midlatitudes, the RWB-related transport is mostly confined to the ocean basins and is strongest in the storm tracks. Overall, RWB-related transport accounts for 68% of the extreme poleward moisture transport across 60°N in winter and 56% in summer. In terms of the total transient transport, RWB accounts for 47% in winter and 37% in summer. Note that the fractions we calculate here are approximations and, if anything, likely underestimate the moisture transport associated with synoptic Rossby waves. As we discussed in Section 2.2, our algorithm does not include the contribution from non-breaking synoptic waves. In addition, although our algorithm has undergone careful inspection, the exact percentages are likely method-dependent and one might obtain slightly different values if another method is used.

Figures 2.7c-d break down the RWB-related transport into the AWB-related and CWB-related transport. The AWB-related transport largely overlaps with the major storm tracks over the North Pacific and North Atlantic basins (Figure 2.7c). Along the west coast of North America, AWB dominates the RWB-related transport (Figures 2.7b-c). This extreme transport is likely associated with the "atmospheric rivers" that occur frequently there, and recent research has linked these extreme moisture transport events with AWB (Ryoo et al. 2013; Payne and Magnusdottir 2014). CWB-related transport tends to be located poleward of the storm track regions and is more dominant in the polar regions and less so in the midlatitudes (Figure 2.7d). Overall, AWB transports more moisture across midlatitudes and the Norwegian Sea-Scandinavia region [30°W-10°E, 55°N-70°N], while CWB transports more moisture across the high latitudes and the Bering Strait [170°E-160°W, 55°N-70°N] and Baffin Bay [60°W-50°W, 55°N-70°N]. These features are also consistent with the composites for extreme poleward moisture transport previously discussed in Figure 2.4.

2.4.3. SEASONALITY

The spatial patterns of RWB-related poleward moisture transport are similar in all other seasons to that of Figure 2.7 (figures not shown) but are of different magnitude. To show the seasonality of the RWB-related transport magnitude, we average the climatological monthly-mean transport across two zonal sectors at 60°N over the two ocean basins (thick red lines in Figures 2.7c-d). We choose 60°N because we are interested in the moisture transport into the Arctic, although we acknowledge that RWB-related transport is strongest at lower latitudes.

The seasonality of RWB-related transport over the North Atlantic is shown as black solid lines in Figure 2.8 and that for the North Pacific in Figure 2.9. All quantities are shown as anomalies, defined as deviations from the annual mean. Over the North Atlantic, AWB-related transport into the Arctic is strongest in early autumn and weakest in spring (Figure 2.8a), while CWB-related

transport is strongest in late autumn and weakest in early summer (Figure 2.8b). AWB-related transport into the Arctic exhibits larger seasonal variations than CWB-related transport. Over the North Pacific, AWB-related transport is strongest from late summer to early autumn and is weakest in spring (Figure 2.9a), while CWB-related transport is strongest from late autumn to winter and is weakest in summer (Figure 2.9b). Similar to the North Atlantic, the seasonal variations are also larger for AWB-related transport in the North Pacific.

2.4.3.1. DECOMPOSITION OF SEASONALITY

Given the results shown above, we ask the question: how much of the seasonality in RWB-related transport is due to the seasonality in the strength of the transport and how much is due to the frequency of the transport events (RWB)? To answer this question, we decompose the seasonality of the total RWB-related transport into two components - one associated with the magnitude of the transport and the other associated with the frequency of the transport events. The climatological monthly-mean transport across the sectors is denoted by T, standing for "total". The climatological monthly-mean frequency of the transport event occurrence is denoted by F standing for "frequency". The mean magnitude of transport per event is obtained by dividing T by F, and is denoted by M, standing for "magnitude". So $T = M \cdot F$ by construction.

In Figures 2.8 and 2.9, we plot the total extreme transport anomaly:

$$T' = (MF)' = MF - \overline{MF}, \tag{2.2}$$

where the overbar denotes the annual mean and prime denotes the deviations from the annual mean. Decomposing M and F into the sum of the mean and deviation from the mean:

$$M = \overline{M} + M' \tag{2.3a}$$

$$F = \overline{F} + F' \tag{2.3b}$$

and substituting them into (2.2), we get

$$(MF)' = \underbrace{M'\overline{F}}_{A} + \underbrace{\overline{M}F'}_{B} + \underbrace{\left(M'F' - \overline{M'F'}\right)}_{C}. \tag{2.4}$$

Under the assumption that term C is negligible compared to terms A and B, we obtain the following approximation for $(MF)'$:

$$(MF)'_{approx} = \underbrace{M'\overline{F}}_{A} + \underbrace{\overline{M}F'}_{B} \tag{2.5}$$

that is, the sum of the magnitude anomaly times the mean frequency and the mean magnitude times the frequency anomaly. $(MF)'_{approx}$ is shown as black dashed lines in Figures 2.8 and 2.9, and closely resembles the seasonality of the total extreme transport (black solid lines), justifying our assumption that term C in (2.4) is negligible. In other words, the deviation of the magnitude anomaly times the frequency anomaly from its mean is small compared to the other terms. Given the validity of this approximation, we can further break down $(MF)'_{approx}$ into two components corresponding to terms A and B in (2.5). The term A is the contribution of the magnitude of transport to the total seasonality and is shown as blue lines in Figures 2.8 and 2.9. The term B is the contribution of the frequency of transport to the total seasonality and is shown as red lines in Figures 2.8 and 2.9.
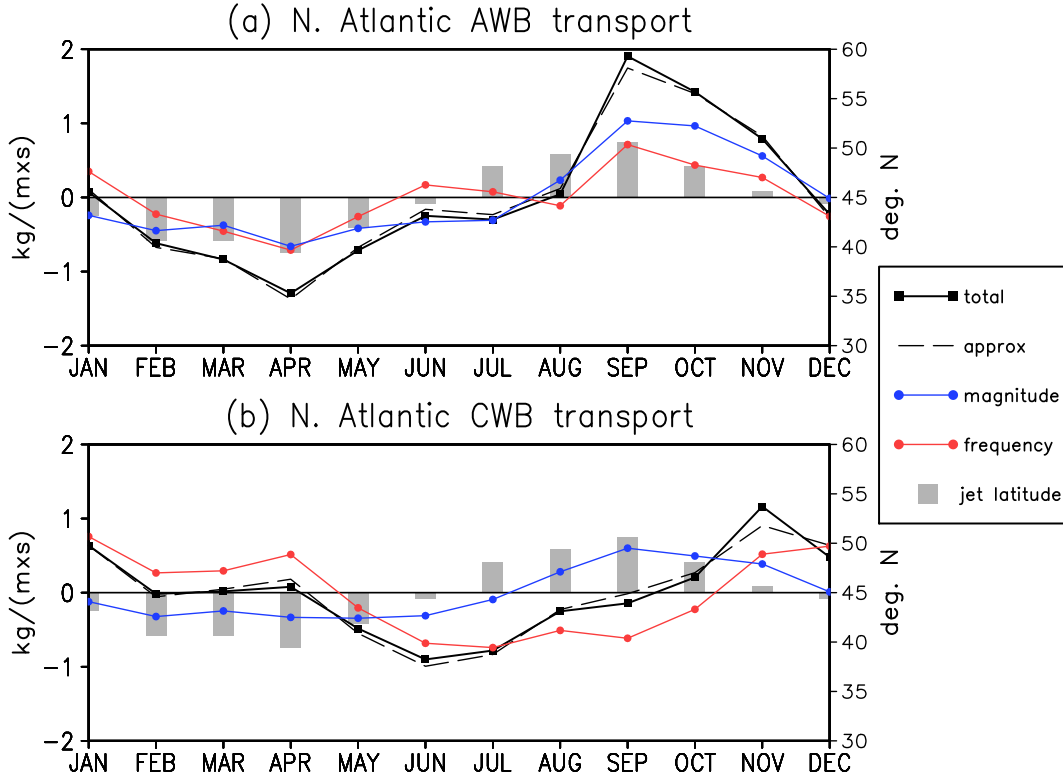
FIG. 2.8. Seasonal cycle of the total (a) anticyclonic and (b) cyclonic RWB-related extreme transient poleward moisture transport across 60°N and contributions from various terms (see text for details). Grey bars denote the midlatitude jet position over the North Atlantic region (80°W-30°W).

2.4.3.2. NORTH ATLANTIC AND NORTH PACIFIC

Over the North Atlantic and the North Pacific, the contribution of magnitude ($M'\overline{F}$; term A) to AWB-related transport and that for CWB-related transport have almost identical seasonality (blue lines in Figures 2.8 and 2.9). For the North Atlantic, the only difference between AWB and CWB is the amplitude of the seasonal variation, which is due to the fact that $\overline{F}$ (average frequency) for AWB is larger than that for CWB over the North Atlantic. Over the two ocean basins, the magnitude of AWB and CWB related transport are both largest in early fall and smallest in spring. The magnitude of transport ($v'q'$) is determined by two components – the circulation anomaly associated with RWB (v') and the moisture anomaly (q'). The latter component is closely related to the background moisture gradient. If the background moisture gradient is large, then the
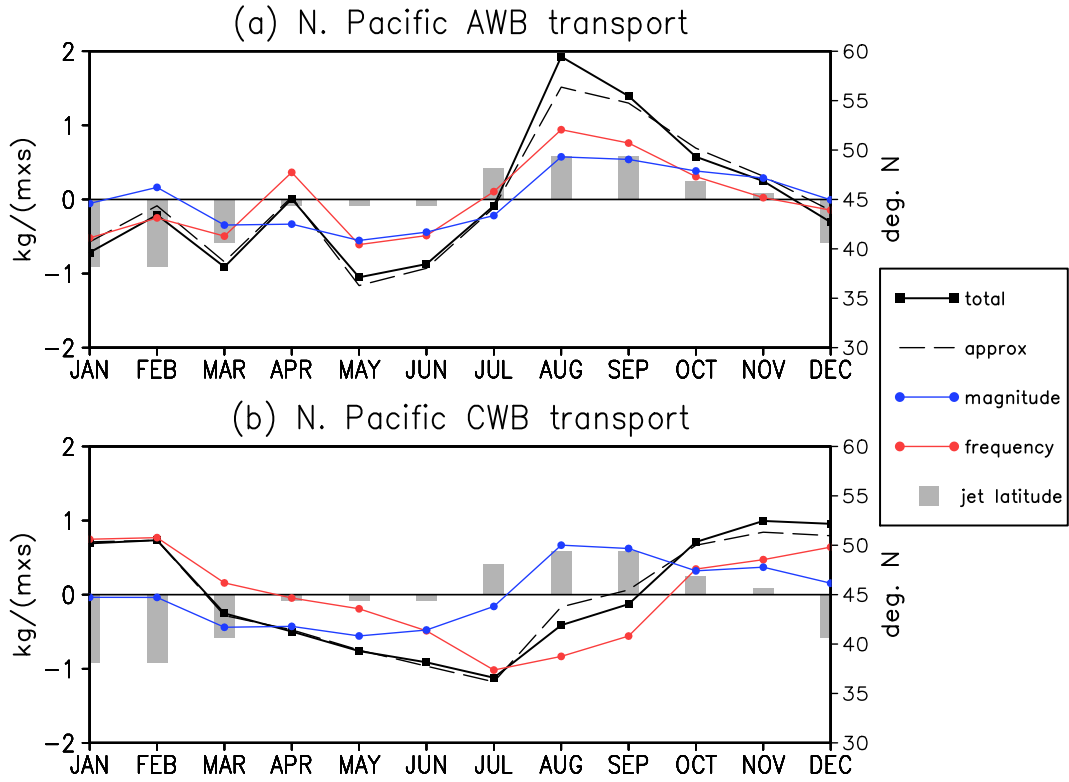
FIG. 2.9. Seasonal cycle of the total (a) anticyclonic and (b) cyclonic RWB-related extreme transient poleward moisture transport across 60°N and contributions from various terms (see text for details). Grey bars denote the midlatitude jet position over the North Pacific region (180°-130°W).

moisture anomaly (q') resulting from transport will be large and vice versa. We have checked the seasonality of the background moisture gradient in the high latitudes for both ocean basins and it is very similar to the seasonality of the magnitude term discussed here (figure not shown). Such similarity suggests, perhaps unsurprisingly, that the magnitude of transport is largely a function of the background moisture gradient.

The frequency of RWB-related transport (red lines in Figures 2.8 and 2.9) contributes a similar amount to the total seasonality as the magnitude (blue lines in Figures 2.8 and 2.9). This highlights the importance of synoptic dynamics to the seasonality of moisture transport. For both the North Atlantic and the North Pacific, the contribution of frequency to AWB-related transport is highest in early fall and lowest in spring, while that to CWB-related transport is highest in winter and lowest

in summer. Previous studies have shown that RWB occurrence is closely linked to the latitude of the eddy-driven jet - AWB (CWB) tends to occur more frequently when the jet is shifted poleward (equatorward) and vice versa (e.g. Strong and Magnusdottir 2008; Woollings et al. 2008; Rivière 2011; Barnes and Hartmann 2012). To see whether the eddy-driven jet position also modulates the frequency of RWB-related transport, we plot the jet latitude in Figures 2.8 and 2.9 as grey bars. The latitude of the jet is calculated as the latitude of maximum 850hPa zonal-mean zonal wind from 80°W to 30°W for the North Atlantic and from 180° to 130°W for the North Pacific. The level of 850hPa is chosen to capture the eddy-driven part of the jet stream (e.g. Barnes and Hartmann 2010; Woollings et al. 2010). For both ocean basins, the seasonality of the AWB frequency is in-phase with the jet latitude (Figures 2.8a and 2.9a) while that of CWB frequency is out-of-phase with the jet latitude (Figures 2.8b and 2.9b), confirming that AWB (CWB)-related transport tends to occur more frequently when the jet is shifted poleward (equatorward). The correlation between the jet latitudes and AWB (CWB)-related transport is 0.72 (-0.73) for the North Atlantic and 0.74 (-0.79) for the North Pacific.

2.4.3.3. SUMMARY OF SEASONALITY

Through a decomposition of the fluxes, we find that the seasonality of RWB-related moisture transport into the Arctic is determined approximately equally by the seasonality of the magnitude of the transport per RWB event (which is largely a function of the background moisture gradient), and the seasonality of the frequency of RWB-related transport occurrence, (which, in turn, is tied to the latitude of the jet stream). The sum of the seasonality of these two contributions constitutes the total seasonality of RWB-related transport.

2.5. MODULATION BY CLIMATE VARIABILITY

As shown in the previous section, the seasonal cycle of RWB-related moisture transport is closely linked to the seasonal cycle of the jet position over the two ocean basins. In this section we try to highlight this connection on interannual time scales. We quantify how transport varies with ENSO/NAO, and we use their influence on jet position to explain the response of the transport. ENSO involves significant changes in the jet stream over the North Pacific (Rasmusson and Wallace 1983; Chen and van den Dool 1999; Ren et al. 2008), while the NAO describes a meridional wobbling of the eddy-driven jet over the North Atlantic (Wittman et al. 2005; Monahan and Fyfe 2006; Woollings et al. 2010). We focus on winter in this section since both teleconnection patterns are most active in winter.

2.5.1. VARIABILITY INFLUENCED BY ENSO

The monthly regression of winter RWB-related poleward moisture transport on the Niño3.4 index is shown in Figure 2.10b. The regression of total poleward moisture transport is also plotted in Figure 2.10a for comparison. The overall spatial patterns are very similar in the two panels except to the south of Japan. In Figure 2.10b, the RWB-related transport significantly decreases (increases) in the North Pacific midlatitudes and in the high latitudes near the Bering Strait [170°W-160°W], while increases (decreases) over western Canada [120°W-100°W] during El-Niño (La-Niña). The regressed magnitude of RWB-related transport (Figure 2.10b) is slightly more than half of that of the total transport (Figure 2.10a; note that the color bar of the two panels are different), and this is mainly due to the fact that RWB-related transport only includes the subset of fluxes stronger than the 90th percentile. To verify this, we have calculated the regression of extreme transport alone (instead of the total as in Figure 2.10a) and it is much more similar to Figure 2.10b in magnitude. To quantify how much of the variability of RWB-related transport is explained by

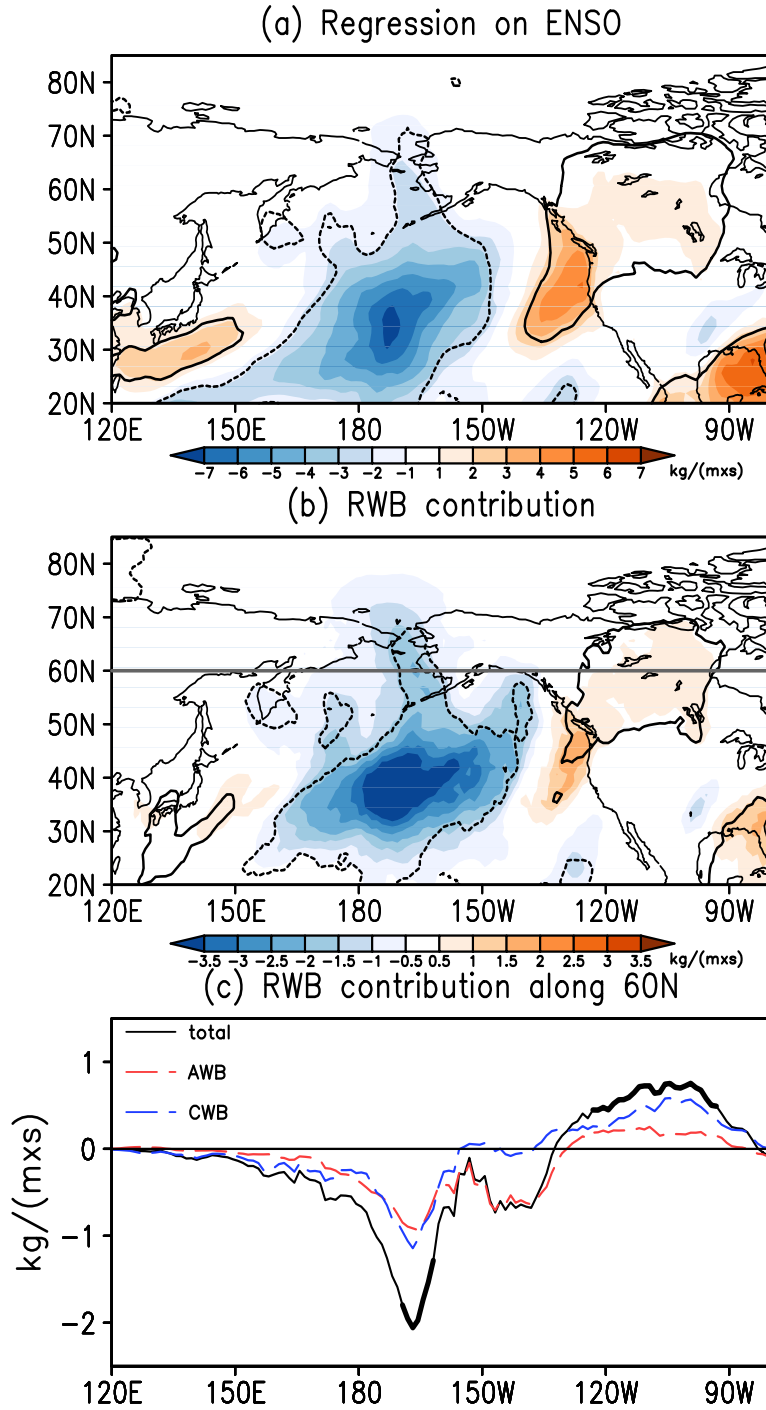FIG. 2.10. Monthly regression of winter (a) total transient poleward moisture transport and, (b) RWB-related transport onto the Niño 3.4 index (shading). The contours enclose anomalies significant at the 95% confidence level. (c) Regression along 60°N in panel (b) split into anticyclonic and cyclonic RWB contributions. Significant values are denoted by a thick black line for the total (thin black line).

ENSO, we calculate the variance explained by ENSO as a fraction of total RWB-related transport variance. The fraction explained is up to 25% in the North Pacific midlatitudes and 10% over western Canada.

Figure 2.10c shows the regression of RWB-related transport along 60°N (solid line in Figure 2.10b), and the contributions from AWB (red dashed line) and CWB (blue dashed line). Along 60°N, the negative transport anomaly near the Bering Strait [170°W-160°W] is half AWB-related and half CWB-related, while the positive anomaly over Canada [120°W-100°W] is dominated by CWB (Figure 2.10c). This result is consistent with Liu et al. (2014) where they showed AWB occurrence decreases over the North Pacific while CWB occurrence increases over southern Canada and the northern U.S. during the canonical El-Niño.

2.5.2. VARIABILITY INFLUENCED BY THE NAO

Similar to ENSO, a comparison between the regression of total and the regression of RWB-related poleward moisture transport onto the NAO index is shown in Figures 2.11a-b. Again, the spatial patterns are very similar and the magnitude of RWB-related extreme transport is half of that of the total. In Figure 2.11b, the RWB-related regression map shows two positive centers near the east coast of the U.S. [70°W-50°W, 35°N-45°N] and near Scandinavia [10°W-30°E, 55°N-70°N], and two negative centers along the west coast of Greenland [60°W-50°W, 55°N-70°N] and to the southwest of Spain [30°W-0°, 30°N-45°N]. Thus, during positive NAO events, there is more RWB-related moisture flux near the east coast of the U.S. and Scandinavia, while there is less RWB-related moisture flux along the west coast of Greenland and to the southwest of Spain. Overall, the NAO can explain up to 30% of the RWB-related transport variance near Baffin Bay, 25% over Scandinavia, and 35% over Spain.

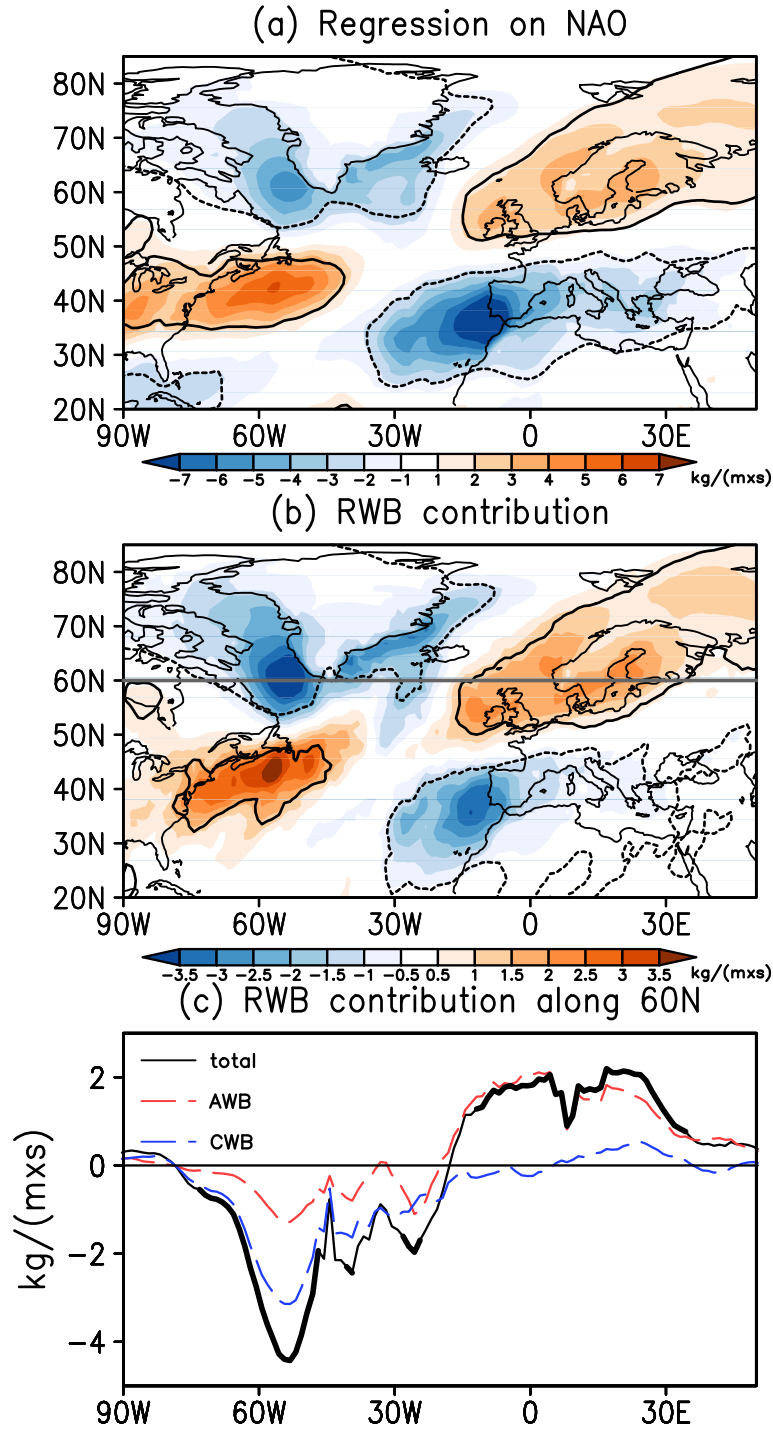FIG. 2.11. Monthly regression of winter (a) total transient poleward moisture transport and, (b) RWB-related transport onto the NAO index (shading). The contours enclose anomalies significant at 95% confidence level. (c) Regression along 60°N in panel (b) split into anticyclonic and cyclonic RWB contributions. Significant values are denoted by a thick black line for the total (thin black line).

Along 60°N, Figure 2.11c demonstrates that CWB dominates the decrease (increase) in RWB-related transport near Greenland [65°W-45°W] while AWB dominates the increase (decrease) over Norwegian sea and Scandinavia [20°W-30°E] during positive (negative) NAO. This is consistent with the results from previous studies that AWB tends to occur more frequently and CWB tends to occur less frequently during positive NAO and vice versa (e.g. Strong and Magnusdottir 2008; Woollings et al. 2008). Since the two anomalies along 60°N associated with the NAO are of opposite sign and of similar magnitude, the NAO variability does not appear to significantly influence the total extreme moisture transport into the Arctic, although it plays an important role in the regional transport of water vapor.

2.6. CONCLUSIONS AND DISCUSSION

Using 6-hourly MERRA reanalysis data, we document the contribution of Rossby wave breaking (RWB) events to the extreme moisture transport into the Arctic, focusing both on the seasonality as well as interannual variability. We focus only on the transient poleward moisture transport with positive v' and positive q', and the main results are summarized bellow.

(1) *Transient moisture transport into the Arctic (across 60°N) is the result of a small number of extreme transport events.*

   We find that the histograms of transient moisture transport into the Arctic feature very heavy positive tails which indicate extreme poleward transport events. We show that the bulk of poleward moisture transport across 60°N is driven by these extreme (greater than the 90th percentile fluxes) transport events. The extreme transport accounts for 69% of the total transient poleward moisture transport in winter and 66% in summer.

(2) *A substantial fraction of the extreme transient moisture transport into the Arctic is tied to synoptic Rossby wave breaking (RWB).*

Composites based on extreme transport events reveal a tight connection to Rossby wave breaking. Using a RWB tracking algorithm, we determine that in winter, AWB contributes significantly to the moisture flux in the mid-latitude storm track regions and the high-latitude Norwegian Sea and Scandinavia regions [30°W-10°E, 55°N-70°N]. CWB dominates the moisture flux over the Aleutian Islands [170°E-160°W, 55°N-70°N] and off the west coast of Greenland [60°W-50°W, 55°N-70°N]. The zonal-mean RWB transport across 60°N contributes 68% of the total extreme moisture transport in winter and 56% in summer.

(3) *The seasonality of RWB-related extreme transport into the Arctic is determined equally by contributions from both the magnitude of each transport event (magnitude of v'q') and the frequency of occurrence of transport events (frequency of RWB).*

The magnitude of the RWB-related transport is largely a function of the background moisture gradient, while the frequency of the RWB-related transport occurrence is tied to the seasonal variation of the latitude of the jet stream – AWB (CWB) related transport occurs more frequently when the jet is shifted poleward (equatorward) and vice versa. The relatively equal contribution from the two components to the total seasonality highlights the importance of both dynamics and available moisture in determining the transient extreme moisture flux.

(4) *The interannual variability of RWB-related extreme transport into the Arctic in winter is modulated by climate variability, namely, ENSO and the NAO.*

In the positive (negative) phase of ENSO, AWB transports less (more) moisture across the Bering Strait [170°W-160°W] and CWB transports more (less) across western Canada [120°W-100°W]. In the positive (negative) phase of the NAO, AWB transports more (less)

moisture through the Norwegian Sea [20°W-30°E] and CWB transports less (more) along
the west coast of Greenland [65°W-45°W].

The observed climate variability captured by ENSO and the NAO are not well reproduced in climate model projections. For example, in coupled general circulation models, the anomalous SST signal related to ENSO is usually shifted westward compared to the observations (e.g. Neelin et al. 1992; Latif et al. 1993; Davey et al. 2002), and this could impact the location of moisture transport by changing the location of RWB. In addition, the latitude of the eddy-driven jet over the North Atlantic in climate models exhibits an equatorward bias (e.g. Kidston and Gerber 2010; Barnes and Polvani 2013), similar to a negative NAO state. This could potentially lead to a bias in moisture flux into the Arctic with a similar pattern to that associated with a negative NAO. Given the results presented in this chapter, we argue that it is necessary for models to accurately simulate synoptic variability in the midlatitudes in order to accurately simulate moisture transport into the Arctic. Furthermore, model biases in the jet position will likely translate to biases in high-latitude water vapor transport.

In the future, climate models project increased moisture transport into the Arctic (e.g. Kug et al. 2010; Bengtsson et al. 2011). Focusing only on the zonal-mean transport, studies show that thermodynamic effects contribute more than dynamics to this increased transport (e.g. Skific et al. 2009b,a; Skific and Francis 2013). However, the moisture transport into the Arctic has substantial zonal variations, being strongest in several preferred regions (Serreze et al. 1995). We've shown in this work that the variability of moisture transport into the Arctic in these regions is closely related to the mid-latitude Rossby wave dynamics, which is, in turn, tied to the jet variability. We argue that if the jet streams shift poleward in the future as projected by climate models (e.g. Yin 2005;

Miller et al. 2006; Swart and Fyfe 2012), Rossby wave dynamics will play an essential role in the

regional long-term changes of moisture transport into the Arctic.

CHAPTER 3

SYNOPTIC FORMATION OF DOUBLE TROPOPAUSES

3.1. INTRODUCTION

The tropopause marks an interface between two dynamically and chemically distinct parts of the atmosphere – the stratosphere and the troposphere. The transport and mixing of compositions across this interface has profound consequences for the global climate and chemistry. For example, the variation in greenhouse gases such as water vapor and ozone near the tropopause is strikingly efficient in altering the radiative forcing and hence the global surface temperature (e.g. Forster et al. 1997; Solomon et al. 2010; Riese et al. 2012). Furthermore, the variability of stratosphere-to-troposphere ozone flux can translate to the variability of the health-related ultraviolet index (e.g. Hegglin and Shepherd 2009). In addition to its radiative impact, ozone is itself detrimental to human health and its surface concentration is currently regulated by the U.S. Environmental Protection Agency (U.S. EPA) (2006).

The structure of the tropopause is thus of great interest due to its ability to influence the exchange between the stratosphere and the troposphere. Particularly, the vertical folding of the tropopause is an important candidate for enhancing this exchange (e.g. Shapiro 1980). When observed via sounding profiles, this folding structure appears as "double tropopauses" (e.g. Kochanski 1955; Seidel and Randel 2006), featuring the vertical stacking of two stable tropopause layers separated by a less stable layer (Fig. 3.1a). Double tropopauses occur in both hemispheres and all seasons, with their highest frequencies in winter (e.g. Randel et al. 2007a; Añel et al. 2008; Peevey et al. 2012). During double tropopause events, radiosonde and satellite observations above the first tropopause show less stratospheric trace gases and more tropospheric trace gases compared to

single tropopause events (e.g. Randel et al. 2007a; Schwartz et al. 2015), indicating strengthened transport and mixing between the two tropopauses. However, to our knowledge no quantitative comparison has been done regarding the role of double tropopauses in enhancing stratosphere-troposphere exchange. Quantitatively addressing this question is one of the goals of this study.

The occurrence of double tropopauses has been shown to be associated with extratropical synoptic disturbances. Studies show an eastward propagation of double tropopauses events in Hovmöller diagrams (e.g. Castanheira and Gimeno 2011; Peevey et al. 2012), indicating their association with baroclinic Rossby waves embedded in westerly flow. Peevey et al. (2014) documented the linkage between double tropopauses and warm conveyer belts, a common feature in baroclinic disturbances. Wang and Polvani (2011) demonstrated in idealized simulations that it is the breaking of these waves that creates the largest coverage of double tropopauses. In observations this linkage between Rossby wave breaking and double tropopauses, however, has only been shown in individual case studies (e.g. Pan et al. 2009). In this work, we present the statistical relationship between double tropopauses and synoptic Rossby wave breaking by applying a wave breaking detection algorithm to satellite observations and reanalysis data.

The specific mechanisms responsible for the formation of double tropopauses remain unknown, despite the many clues alluded to in previous studies. The clues include baroclinic wave activity and the tropopause inversion layer (TIL) (e.g. Wang and Polvani 2011; Peevey et al. 2014), which is a thin layer with very strong stratification right above the tropopause (e.g. Birner et al. 2002; Birner 2006). Following these clues, we explore possible mechanisms with a focus on adiabatic synoptic processes. In particular, we propose that double tropopauses can be formed by either *advection* of existing tropopauses or *creation* of new tropopauses above old ones. We demonstrate
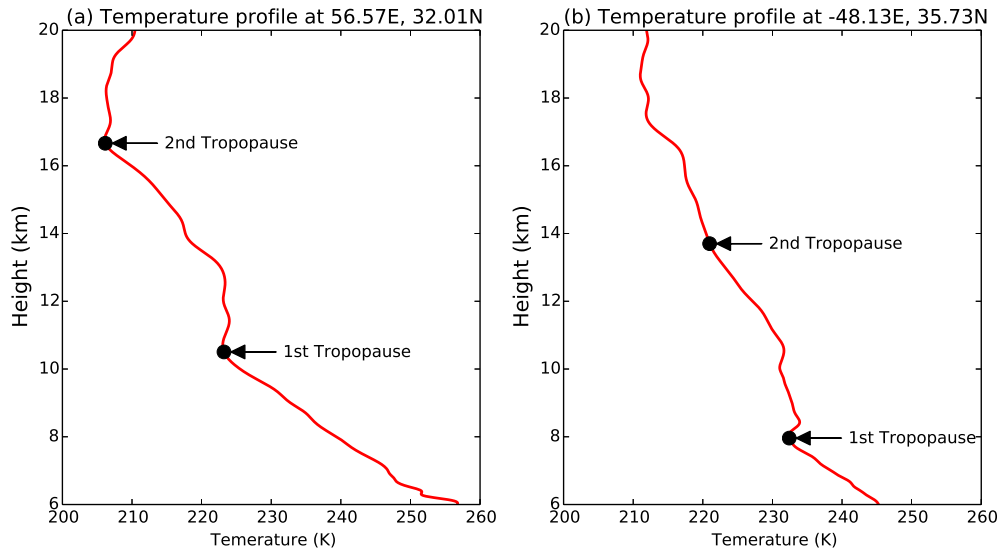
FIG. 3.1. Temperature profiles from COSMIC GPS data on (a) Jan 24, 2007, and (b) Jan 22, 2007.

these two mechanisms in satellite observations, reanalysis, and model simulations, and show how baroclinic waves and a TIL help form double tropopauses by advecting and creating tropopauses.

We address three questions in this study: (1) What are the statistical relationships between double tropopauses and Rossby wave breaking in the observations? (2) What are the mechanisms responsible for double tropopause formation? (3) How do double tropopauses impact stratosphere-troposphere exchange?

The dataset and diagnostic methods used to address these questions are described in Section 3.2. Sections 3.3 to 3.5 address the three questions above in order. Section 3.6 summarizes the main conclusions and discusses how our results relate to those of previous studies.

3.2. DATA AND METHODOLOGY

3.2.1. GPS RADIO OCCULTATION DATA

GPS radio occultation measurements (hereafter GPS data) provide accurate temperature observations with high vertical resolution (e.g. Liou et al. 2007), which reveal finer and more realistic

tropopause structure compared to reanalysis (e.g. Birner et al. 2006; Son et al. 2011). We use GPS data from the Constellation Observing System for Meteorology, Ionosphere, and Climate (COSMIC) which started in late 2006. The temperature profiles were retrieved by the University Corporation for Atmospheric Research (UCAR) from 2007 to 2013. We use only dry retrievals over this period which are of the highest quality in regions with low water vapor concentration such as the tropopause layers (e.g. Wickert et al. 2005).

To study the spatial pattern of double tropopauses and their corresponding stratification, we transform thousands of temperature profiles over the entire globe each day into regularly gridded data with a horizontal resolution of $2.5° \times 2.5°$ and vertical resolution of 500m by linear barycentric interpolation. Such a horizontal resolution is chosen as a balance between the need for relative fine structure and a limited number of profiles. From these gridded daily temperature profiles, we calculate the potential temperature θ, the Brunt-Väisälä frequency $N^2 = g\partial(ln\theta)/\partial z$, and the height of the tropopauses using the definition of the World Meteorological Organization (1957). Specifically, the first tropopause is defined as the lowest level at which the lapse rate decreases to 2K/km, provided that the average lapse rate between this level and any level above within 2km is not greater than 2K/km. Above the first tropopause, if the average lapse rate between any level and all higher levels within $1km$ exceeds 3K/km again, a second tropopause is defined using the same criteria as the first.

3.2.2. REANALYSIS DATA

To characterize the dynamical features of double tropopauses, we use potential vorticity (PV) from ERA-Interim reanalysis data (Dee et al. 2011) over the period from January 2007 to December 2013. The PV field has a horizontal resolution of $1.5° \times 1.5°$ and 15 isentropic levels ranging

from 265K to 850K. We apply two diagnostics to the isentropic PV field, which are described in the following subsections.

3.2.2.1. EQUIVALENT LATITUDE ANOMALY

Since PV contours on isentropic surfaces are material lines for adiabatic motion in the absence of friction, PV is an ideal field for characterizing advection by synoptic disturbances. Inspired by Pan et al. (2009), we first map PV (q) at each grid point to its corresponding equivalent latitude (ϕ_e) value according to Butchart and Remsberg (1986):

$$\phi_e\left[q(\lambda,\phi),\theta\right] = \arcsin\left[1 - \frac{A(q,\theta)}{2\pi a^2}\right] \tag{3.1}$$

where $A(q,\theta)$ is the area enclosed by a q contour on an isentrope θ and a is the radius of the earth. By this definition, $\phi_e(q,\theta)$ is the latitude circle that encloses the same area as the q contour. Figure 3.2 shows the $q=3$ PVU contour on 350K isentrope and its equivalent latitude ϕ_e (dashed line). As shown in Fig. 3.2, an air parcel's equivalent latitude can be thought of as the latitude it comes from. Accordingly, the difference between an air parcel's actual latitude and its equivalent latitude:

$$\phi_a(\lambda,\phi,\theta) = \phi - \phi_e(\lambda,\phi,\theta) \tag{3.2}$$

can be used to measure the meridional excursion experienced by an air parcel due to synoptic adiabatic disturbances. Figure 3.2 illustrates the ϕ_a (shading) enclosed by wave lobes associated with the $q=3$ PVU contour. Positive ϕ_a (red shading) represents poleward advection, whereas negative ϕ_a (blue shading) represents equatorward advection.
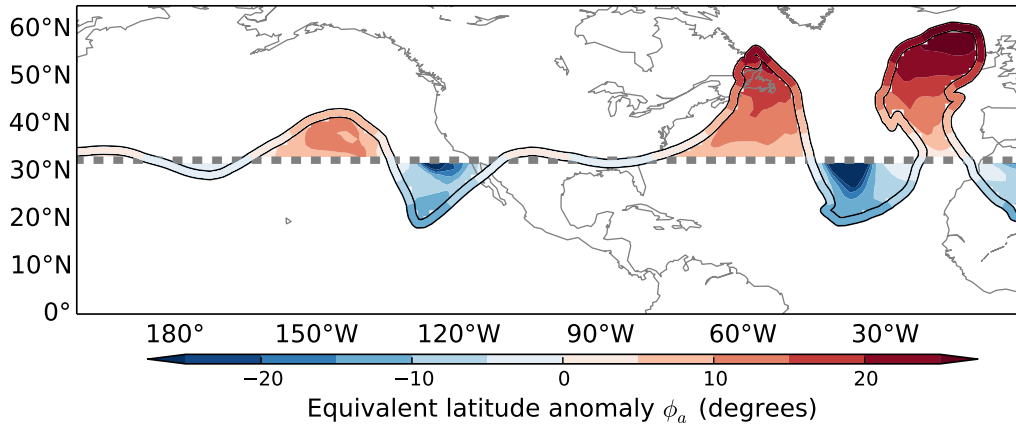
FIG. 3.2. Potential vorticity of 3 PVU (solid contour) on 350K isentropic surface on Jan 26, 2010 and its corresponding equivalent latitude ϕ_e (dashed line) from ERA-Interim. The equivalent latitude anomaly ϕ_a (color shading) between the 3 PVU contour and the equivalent latitude ϕ_e is also plotted.

3.2.2.2. ROSSBY WAVE BREAKING DETECTION

As shown in Fig. 3.2, PV contours are good at depicting the morphology of large-scale Rossby waves. In particular, wave breaking is featured in Fig. 3.2 by the horizontal overturning of the PV contour over the central and eastern North Atlantic. To study these breaking events and their connections to double tropopauses, we apply the PV-based wave breaking detection algorithm described in Liu et al. (2014). The algorithm detects wave breaking by searching for overturning of circumpolar 2 PVU contours on isentropic surfaces ranging from 300K to 350K with an interval of 5K. According to the direction of overturning, wave breaking is classified into anticyclonic wave breaking and cyclonic wave breaking. For example, the overturning in Fig. 3.2 between $40°W$ to $20°W$ is cyclonic, whereas the overturning between $20°W$ to $0°W$ is anticyclonic. For each wave breaking event, the centroid of the overturning anticyclonic lobe is assigned as its center. Throughout this paper, all composites with respect to wave breaking are translated so that the wave breaking centers overlap with each other. For more details, we refer readers to Liu et al. (2014).

3.2.3. BAROCLINIC EDDY LIFECYCLE SIMULATIONS

One of the goals of this study is to quantify how much the occurrence of double tropopauses enhances stratosphere-troposphere exchange compared to situations without a double tropopause. To serve this goal, we construct a control eddy lifecycle simulation with no double tropopause and a series of contrasting lifecycle simulations with varying areal coverage of double tropopauses following Wang and Polvani (2011) (hereafter WP11). The advantage of these simulations is that the only difference among them is the tropopause structure so that we can cleanly isolate any enhancement of stratosphere-troposphere exchange due to the occurrence of double tropopauses. Note that we use a different model from WP11, the Geophysical Fluid Dynamics Laboratory (GFDL) spectral dry dynamical core with a horizontal resolution of T85, and 60 uneven sigma levels. The initial conditions for the simulations are described in Section 3.2.3.1, and the setup for passive tracers is discussed in Section 3.2.3.2.

3.2.3.1. INITIAL CONDITIONS

We prescribe baroclinically unstable initial conditions largely following WP11, with some minor modifications due to the fact that we use a different model. We describe the procedure briefly here with a focus on the differences from WP11. For the omitted details that are common to WP11, we refer readers to the Appendices in their paper.

As in WP11, the temperature field is determined by the lapse rate field $\Gamma(\phi, z)$ which blends a low-latitude tropical profile $\Gamma^L(z)$ with a high-latitude one $\Gamma^H(z)$. Both profiles carry a parameter that determines the strength of the TIL: c_L and c_H respectively. The blending in the meridional direction takes the form:

$$\Gamma(\phi, z) = \Gamma^L(z) + \left(\Gamma^H(z) - \Gamma^L(z)\right) \left[\frac{1}{2} + \frac{1}{2}\tanh\left(\frac{\phi - \phi_0}{\phi_D}\right)\right] \tag{3.3}$$

which is almost the same as WP11 except that we replace metric distances Y, Y_0, and Y_D with latitudes ϕ, ϕ_0, ϕ_D, and set $\phi_0 = 45°$, $\phi_D = 10°$. The initial temperature field (T) is then obtained by integrating the lapse rate from the top of the atmosphere where $T = 220K$.

With the initial temperature field defined, the zonal wind (U) can be obtained by utilizing the thermal wind balance on a sphere:

$$-\frac{R}{H}\frac{\partial T}{\partial \phi} = (af + 2U \tan \phi)\frac{\partial U}{\partial z} \tag{3.4}$$

where R is the ideal gas constant, H is the scale height, and a is the radius of the earth. This differs from the thermal wind balance in WP11 where an f-plane model was used. The zonal wind can be solved for by iterating the vertical integration of (3.4) as:

$$U^{i+1}(\phi, z) = \int_0^z -\frac{R}{H\left(af + 2U^i(\phi, z^*)\tan \phi\right)}\frac{\partial T}{\partial \phi}dz^* \tag{3.5}$$

where we set $U(\phi, 0) = 0$. With an initial guess of $U^0(\phi, z) = 0$, the U^i converges very quickly for the initial temperature field employed here (within a few iterations).

WP11 was able to increase the area of double tropopauses by increasing the strength of the initial high-latitude TIL strength c_H. The reason why a strong high-latitude TIL helps form a double tropopause is one subject of this study and will be revisited in Section 3.4.2. To increase the coverage of double tropopauses, we follow WP11 except that we increase the strength of the low-latitude TIL c_L by the same amount, so that the resulting jet streams have nearly the same strength under both the weak and strong TIL cases. We carry out five simulations with c_H values ranging from 0K/km to 4K/km with an interval of 1K/km. For the low-latitude TIL strength, we always set it as $c_L = c_H + 3$K/km. These five simulations are referred to by the high-latitude TIL

strength (TIL0 through TIL4). To study the mechanisms of double tropopause formation, two of these simulations – TIL0 and TIL3 – are also used in Section 3.4.2.

3.2.3.2. TRACER SETUP

To quantify the influence of double tropopauses on stratosphere-troposphere exchange, we initialize two passive tracers S and T following Polvani and Esler (2007). In particular, we pick the $N_{tp}^2 \equiv 3.5 \times 10^{-4} s^{-2}$ contour as the initial tropopause. We then initialize the two tracers on isentropes ranging from 290K to 500K as:

$$S = \mathcal{H}(N^2 - N_{tp}^2) \tag{3.6a}$$

$$T = \mathcal{H}(N_{tp}^2 - N^2) \tag{3.6b}$$

where $\mathcal{H}()$ is the Heaviside function:

$$\begin{cases} \mathcal{H}(x) = 1, & x \geq 0 \\ \mathcal{H}(x) = 0, & x < 0 \end{cases}$$

$S + T = 1$ at all times by construction. After $t = 0$ we use the contour of $S = T = 0.5$ as the natural tropopause. The mass of S in the troposphere is viewed as the accumulated stratosphere-to-troposphere (STT) tracer mass flux and the mass of T in the stratosphere is viewed as the accumulated troposphere-to-stratosphere (TTS) tracer mass flux:

$$STT = \oint \mathcal{H}(T - 0.5)S\rho dV \tag{3.7a}$$

$$TTS = \oint \mathcal{H}(S - 0.5) T \rho dV \qquad \text{(3.7b)}$$

3.3. THE SYNOPTIC FEATURES OF DOUBLE TROPOPAUSES

Although conforming to the same WMO definition, the actual vertical temperature profiles of double tropopauses can vary substantially. Figure 3.1 exemplifies two types of double tropopause profiles from the COSMIC GPS data. In Fig. 3.1a, both the first and the second tropopauses mark a discontinuity in the thermal stratification in a similar way. Between the two tropopauses, there is a layer (13-16km in altitude) with a tropospheric lapse rate of $5 - 6$K/km, similar to the lapse rate below the first tropopause. In some ways, the stratification around the second tropopause looks like a replication of that around the first tropopause. This suggests that the second tropopause in Fig. 3.1a may have existed before and the double tropopause was formed by horizontal advection. In Fig. 3.1b, the second tropopause does not mark a discontinuity, but a threshold defined by the WMO as the lapse rate increases gradually with height back above 2K/km. In this case, the second tropopause seems more likely to have been created by local changes in the thermal stratification. In this section, we focus on the general features of double tropopauses first and address two possible formation mechanisms in Section 3.4.

Using COSMIC GPS data, the wintertime climatology of double tropopauses occurrence from 2007 to 2013 is shown in Fig. 3.3a (shading) along with the corresponding height of the first tropopause (contour). The double tropopauses generally occur in the subtropics within the 30°N to 40°N band where the climatological tropopause slope is most steep (grey contours). Their most frequent occurrence is located over North America and the northwest Atlantic, which is consistent with Randel et al. (2007a). Away from the subtropics, double tropopauses also occur at higher latitudes over the North Atlantic, maximizing near the Norwegian Sea and the Greenland Sea.
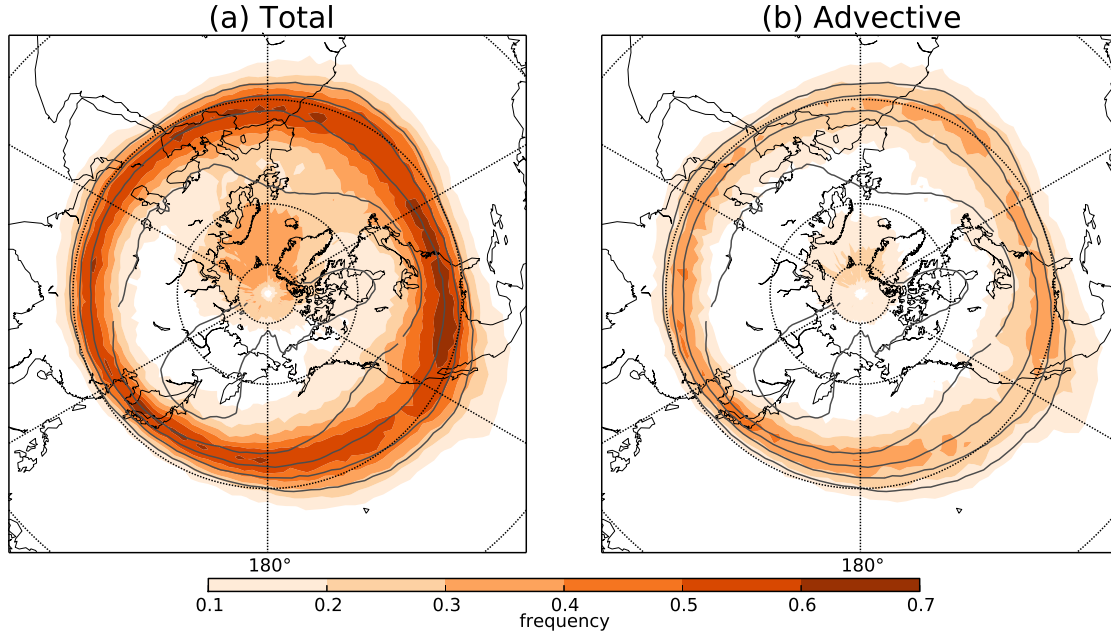
FIG. 3.3. Climatology of double tropopause frequency (shading) in the Northern Hemisphere during winter for (a) total occurrence, and (b) occurrence due to differential advection (see Section 3.4.1 for details). Grey contours denote the climatological height of the first tropopause with an interval of 1.5km, with the largest being 15.5km.

To illustrate the synoptic features associated with double tropopauses, we show snapshots of two individual events in the two columns of Fig. 3.4. The upper row shows the meridional cross sections of thermal stratification N^2 (shading) and the equivalent latitude contour of $\phi_e = 30°N$ derived from PV. The black dots denote the tropopauses identified by the WMO definition. The lower row shows potential temperature on the 2PVU surface, representing the dynamical tropopause. For the event on Jan 24 (left column of Fig. 3.4), the stacking of two tropopauses occurs between 25°N to 45°N, with the tropopauses vertically separated by a distance of about 6km. Corresponding to this tropopause structure, the N^2 field exhibits a clockwise folding. The cause of this folding is revealed by the $\phi_e = 30°N$ contour, which reaches 45°N at the higher tropopause level. Assuming the air on the contour is from 30°N, this indicates a substantial poleward advection of the higher tropopause which then overlapped with the extratropical lower tropopause that remained relatively
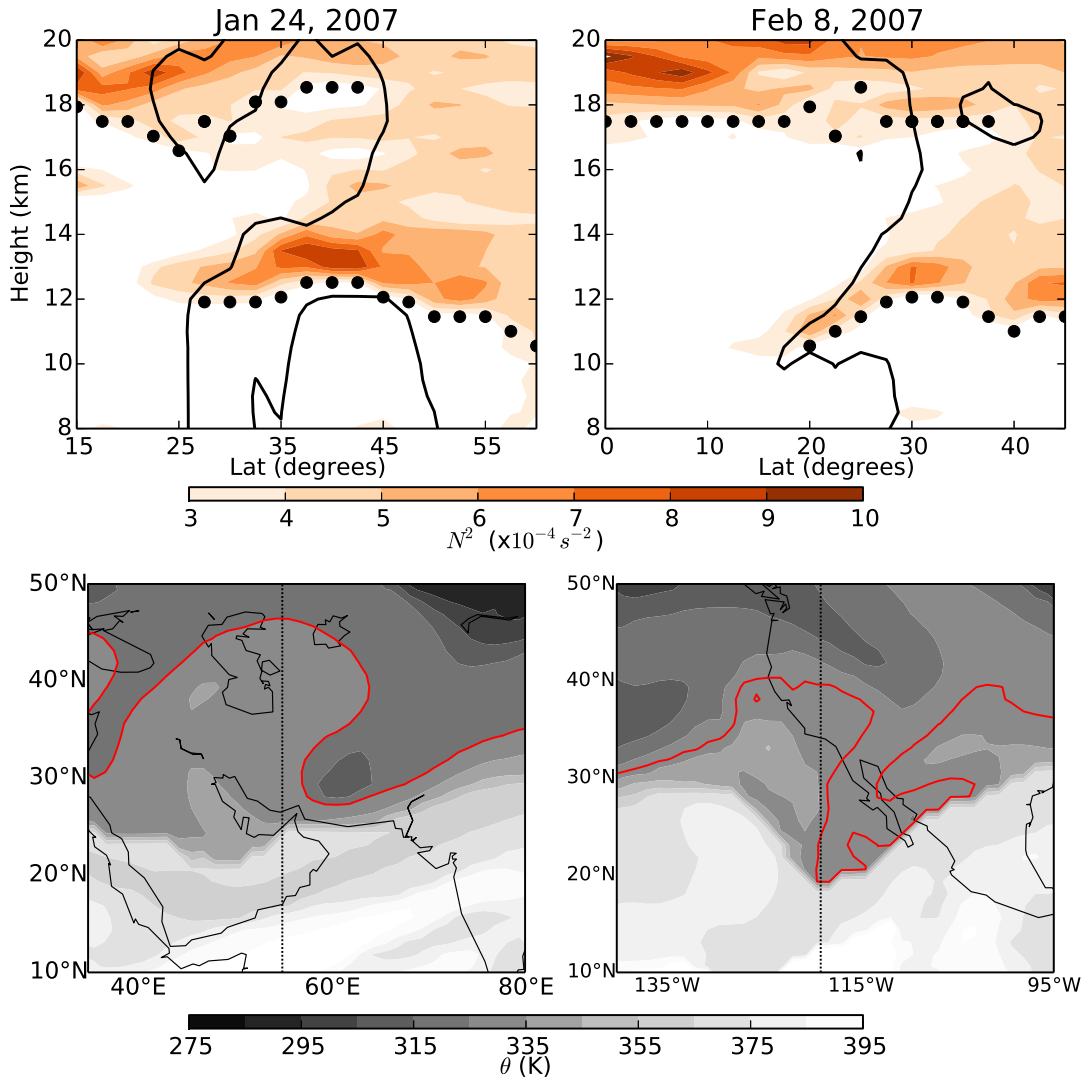
FIG. 3.4. The left column shows an event on Jan 24, 2007 and the right column shows an event on Feb 8, 2007. **Upper row:** Snapshots of the Brunt-Väisälä frequency N^2 (shading) from GPS temperature data and equivalent latitude contour $\phi_e=30°$ (black contour) from ERA-Interim reanalysis. The black solid circles denote the tropopause identified by GPS temperature data. **Lower row:** Potential temperature θ (grey shading, unit: K) on the 2 PVU surface which represents the dynamical tropopause. The dotted lines denote the longitude at which those cross sections are taken and shown in the upper row. The red contours accent the overturning of θ.

stationary. In the lower panel of Fig. 3.4, we show that the strong poleward intrusion at the higher

tropopause level happened as a result of horizontal overturning corresponding to an anticyclonic

wave breaking event.

The event on Feb 8 makes an interesting comparison with the event on Jan 24 and is shown in the right column of Fig. 3.4. The vertically stacked tropopauses are separated by 5-7km and a clockwise folding of N^2 contour is also seen. As in the previous case, the shape of the $\phi_e = 30°N$ contour aligns well with the N^2 contour, indicating that differential advection caused the folding of the $\phi_e = 30°N$ contour. However, the difference is that this event was dominated by an equatorward intrusion, rather than a poleward intrusion. Specifically, the air at the lower tropopause level was advected from 30°N equatorward to 20°N while the air at the higher tropopause barely moved from its equivalent latitude. The result is that the lower extratropical tropopause moved equatorward and overlapped with the tropical tropopause above. Examining the horizontal advection pattern (lower panel of Fig. 3.4), we also find an antiycyclonic wave breaking event providing the critical equatorward intrusion. But the intrusion was associated with the breaking wave's equatorward lobe, rather than the poleward lobe.

The two examples above suggest a possible link between Rossby wave breaking and double tropopauses. We further support this linkage by compositing PV with respect to the occurrence of double tropopauses in specific regions (Fig. 3.5). Specifically, PV is composited for days when more than 80% of the GPS temperature profiles within the red rectangle exhibit double tropopauses. Both composites in Fig. 3.5 exhibit large-scale horizontal overturning of PV contours indicative of Rossby wave breaking. In particular, the double tropopauses over the subtropical northeastern Pacific tend to occur in the equatorward lobe of anticyclonic wave breaking (Fig. 3.5a), whereas those over the Labrador Sea tend to occur in the equatorward lobe of a cyclonic wave breaking (Fig. 3.5b).

As Rossby wave breaking is shown to be linked to double tropopauses climatologically, we ask "what are the mechanisms through which they are linked". The snapshots in Fig. 3.4 suggest
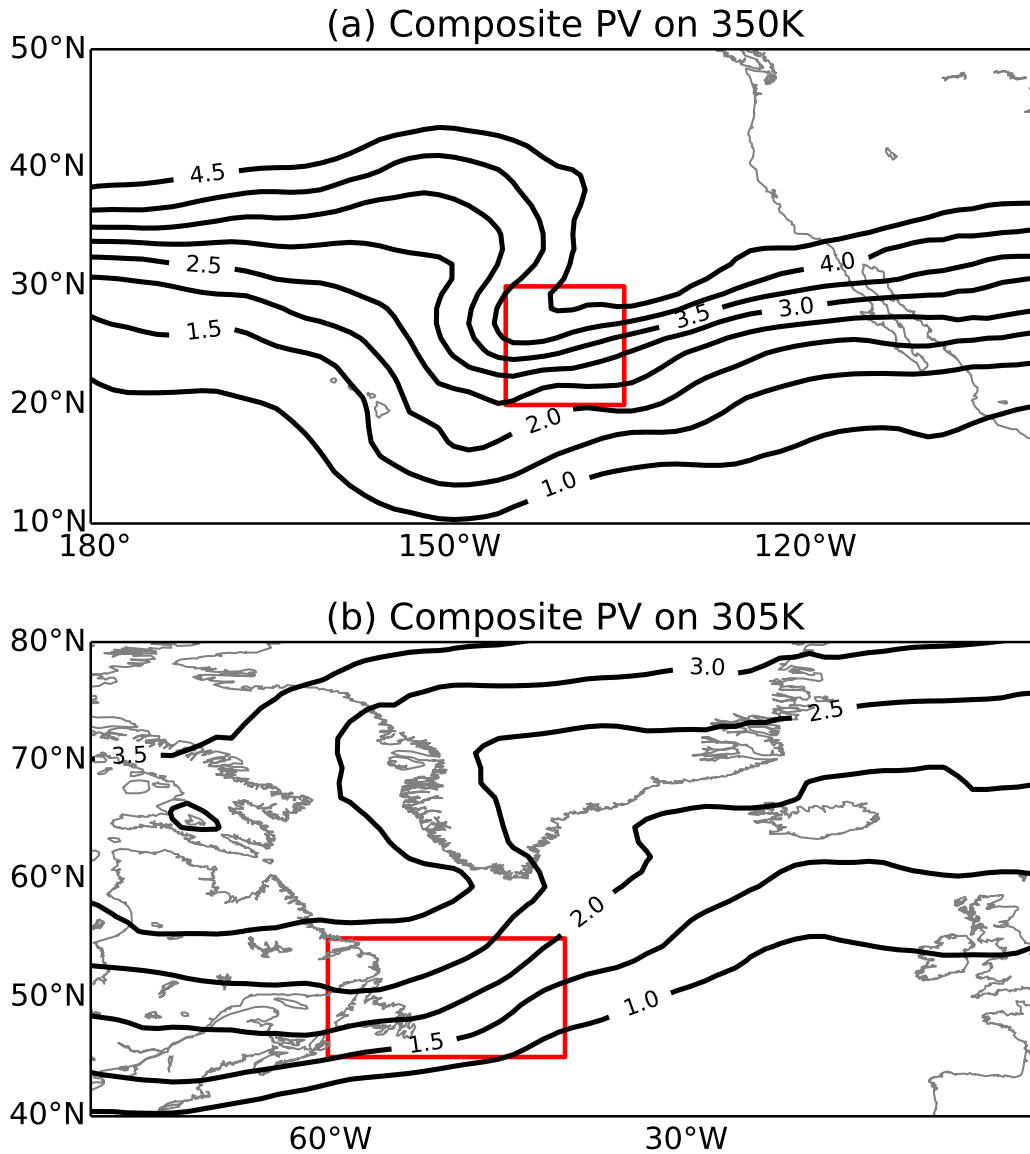
FIG. 3.5. Composite potential vorticity (in PV unit) on isentropes for days when more than 80% of profiles within the red rectangle exhibit double tropopauses.

that wave breaking may help form double tropopauses by providing vertically differential advection, either stronger poleward advection of the higher tropical tropopause or stronger equatorward advection of the lower extratropical tropopause. We will further investigate this hypothesis in the next section.

3.4. MECHANISMS FOR THE ADIABATIC FORMATION OF DOUBLE TROPOPAUSES

Since double tropopauses are defined by thermal stratification, looking at its budget should provide clues to the formation of double tropopauses. Below is the adiabatic prognostic equation of N^2 using the approximation of thermal wind balance for large-scale flow:

$$\frac{\partial N^2}{\partial t} = \underbrace{-\mathbf{V} \cdot \nabla N^2}_{A} + \underbrace{N^2 \frac{\partial w}{\partial z}}_{B} \tag{3.8}$$

The terms on the RHS correspond to two physical processes that contribute to the local change in N^2, as alluded to in Fig. 3.1. The first is the advection term (A) and the other is the compression/stretching term (B) that produces/destroys N^2. When the production term B is small, N^2 behaves like a passive tracer and the formation of double tropopause can be mainly attributed to differential horizontal advection. When the production term is not small, double tropopauses can be formed even in the absence of differential advection. We explore these two mechanisms in the next two subsections.

While the evolution of N^2 is likely always a mixture of both A and B, we aim to understand the behavior of tropopause evolution under each separately as a stepping stone to understanding more complex scenarios. In addition, we illustrate in observations and model simulations that the formation of double tropopause can at times be predominantly determined by one of these two mechanisms.

3.4.1. DIFFERENTIAL ADVECTION

Snapshots in Fig. 3.4 illustrate a possible mechanism by which Rossby wave breaking helps form double tropopauses – providing differential advection. To examine how robust this mechanism is in climatology, we composite variables for the two types of Rossby wave breaking events in Fig. 3.6. The upper row shows the composite double tropopause frequency anomaly (shading) and the lower row shows the the corresponding thermal stratification and advection pattern. The composites are made by horizontally shifting the fields about the wave breaking centers, so the x and y axes are relative longitude and latitude respectively. We only use centers with a latitude between 30°N and 55°N, to focus on the region where the climatological tropopause is steep and differential advection is most likely to operate.

Double tropopauses occur significantly more frequently than climatology to the north of anticyclonic wave breaking (Fig. 3.6a). Higher frequencies of double tropopauses also occur to the south of anticyclonic wave breaking's equatorward lobe, but with much weaker strength. To visualize the vertical structure of stratification associated with the anomalous double tropopause formation shown in Fig. 3.6a, we plot a meridional cross section of N^2 (contours) along $-17.5°$ relative longitude in Fig. 3.6c. The N^2 contours folds substantially in the composite, demonstrating the robustness of this double tropopause structure. To see if the folding is related to differential advection, we color the folding contours by their anomalous equivalent latitude ϕ_a. The red shading indicates poleward advection and the blue shading indicates equatorward advection. The folding in Fig. 3.6c is mainly associated with extensive poleward advection at 16km height and little advection near 13.5km, depicting a major role for differential advection in the formation of these double tropopauses in a composite sense. Comparing Fig. 3.6a and Fig. 3.6c, one can see the poleward
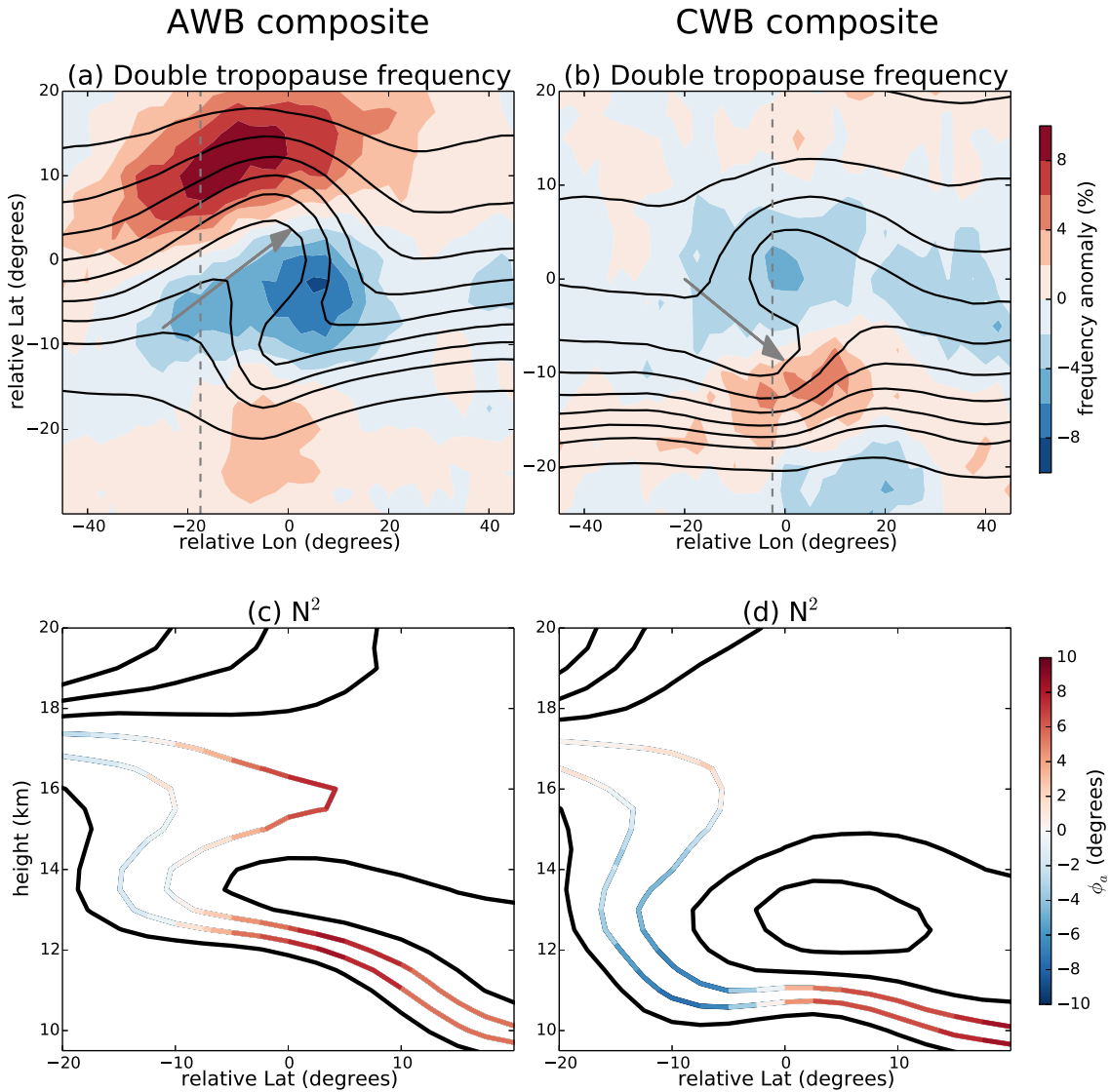
FIG. 3.6. Composite variables for anticyclonic wave breaking (AWB) in the left column and cyclonic wave breaking (CWB) in the right column. The fields are moved horizontally so that the centers for each type of wave breaking overlap. The longitude and latitude shown on axes are relative to the wave breaking centers. **Upper row:** Anomalous frequency of double tropopause occurrence (shading) and potential temperature θ (contour) on the 2 PVU surface which represents the dynamical tropopause. **Lower row:** Cross section of N^2 (contour) taken along the dashed lines in the upper row. The color shading is added to the folding contours and denotes the equivalent latitude anomaly ϕ_a. The interval of the N^2 contours is $0.5 \times 10^{-4} s^{-2}$, and the value for the two colored contours are $3.5 \times 10^{-4} s^{-2}$, $4 \times 10^{-4} s^{-2}$ respectively.

advection north of -10° relative latitude is provided by the poleward advection of anticyclonic wave breaking, as is also exemplified in the left column of Fig. 3.4.

For cyclonic wave breaking, the largest positive anomaly of double tropopause frequency occurs at the south edge of its equatorward lobe (Fig. 3.6b). To visualize the meridional structure of thermal stratification associated with the largest anomaly, another cross section is taken along $-2.5°$ relative longitude and shown in Fig. 3.6d. Similar to anticyclonic wave breaking, N^2 contours fold substantially, indicating the robustness of the double tropopause anomalies. What is different, however, is that the folding is dominated by equatorward advection of the lower tropopause near the height of 11km. The dominating equatorward advection to the south of -5° relative latitude is provided by the equatorward lobe of cyclonic wave breaking. Comparing Fig. 3.6c with Fig. 3.6d, it is evident that the double tropopauses formed in the cyclonic lobe by equatorward advection are more vertically separated than those formed in the anticyclonic lobe by poleward advection, which is also alluded in Figs. 3.4a and 3.4b. This is consistent with Wirth (2001) who studied the double tropopauses resulting from idealized differential advection of PV.

The composites for wave breaking along with snapshots in Fig. 3.4 demonstrate that differential advection can dominate the formation of double tropopauses in a composite sense. We proceed by addressing how often this happens, regardless of the occurrence of wave breaking. To answer this, we classify each double tropopause occurrence into advective and non-advective using the equivalent latitude ϕ_e field. In words, for each second tropopause, we test if it still overlaps with a lower tropopause after we move all the tropopauses meridionally to their equivalent latitudes. If it does, we classify it as a non-advective double tropopause. Otherwise we mark it as advective.

The result of the classification is shown in Fig. 3.3b. Advective double tropopause occurrence is more confined in the tropopause break region than the total occurrence. This supports the hypothesis that the advective mechanism is most likely to operate in the tropopause break region. In particular, the most frequent occurrence of advective double tropopauses is located over east Asia and the North Pacific near Japan where the tropopause slope is steepest. Summing up the total occurrence of advective double tropopauses, differential advection appears to account for 47% of the total occurrence of double tropopauses in the Northern Hemisphere.

Besides differential advection, previous studies have also focused on the direction of the mean advection above the first tropopause (e.g. Pan et al. 2009; Añel et al. 2012; Schwartz et al. 2015; Wang and Polvani 2011). We next quantify how favorable various advection patterns are for double tropopause formation. Specifically, we take all the GPS profiles and calculate the frequency of double tropopause as a function of both mean advection (ϕ_a^{mean}) and differential advection (ϕ_a^{diff}) associated with the profiles (Fig. 3.7). Positive and negative ϕ_a^{mean} indicates poleward and equatorward mean advection respectively. Positive and negative ϕ_a^{diff} indicate clockwise and counterclockwise folding respectively. The four corners of Fig. 3.7 correspond to the four combined advection patterns which are illustrated by schematics at their corresponding corners. For detailed definitions of ϕ_a^{mean} and ϕ_a^{diff}, we refer readers to Appendix A.1.

In Fig. 3.7, the occurrence of double tropopauses is largely dictated by differential advection ϕ_a^{diff}. That is, the frequency of double tropopauses is mainly stratified in the vertical direction of the plot, becoming increasingly more frequent as the value of ϕ_a^{diff} increases for any ϕ_a^{mean} bin. Particularly large increases occur near the transition from negative ϕ_a^{diff} to positive ϕ_a^{diff}, the latter of which represents the favorable shear direction for forming double tropopauses. When the shear direction is in favor of double tropopauses ($\phi_a^{diff} > 0$), poleward mean advection ($\phi_a^{mean} > 0$) is
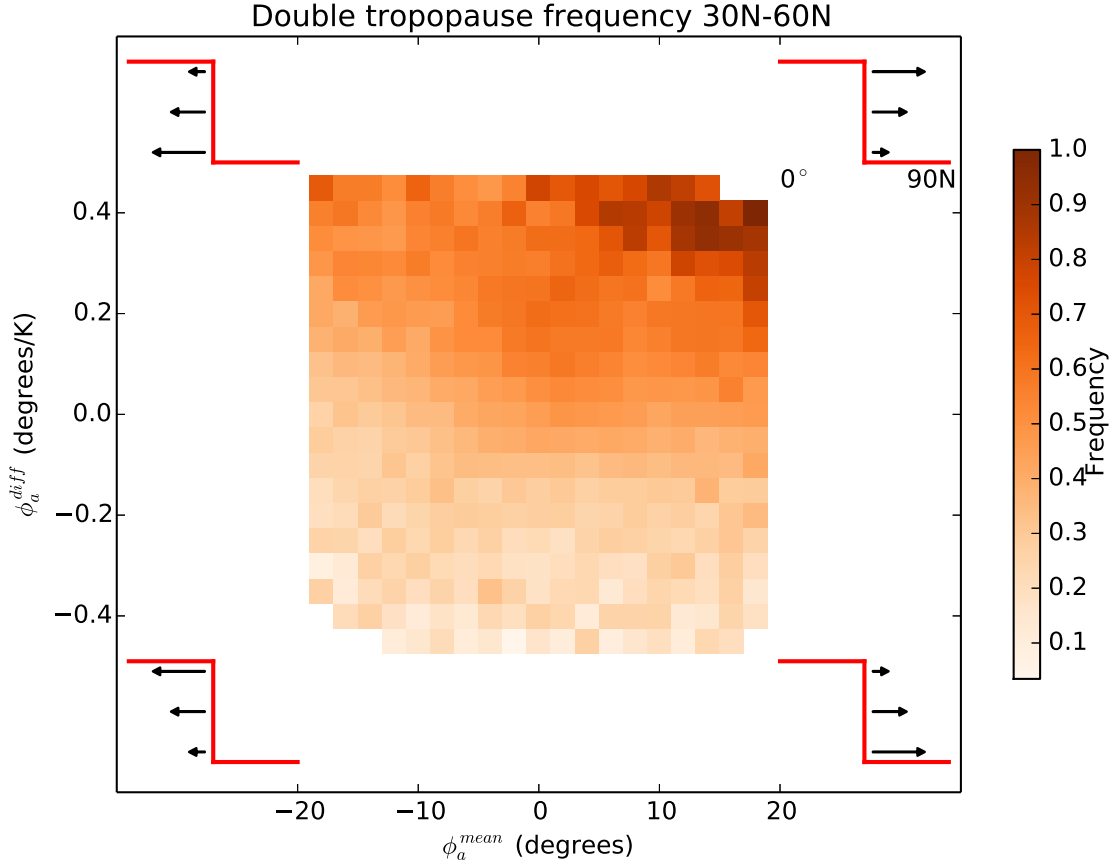
FIG. 3.7. The frequency of wintertime double tropopauses for COSMIC GPS profiles binned by mean equivalent latitude anomaly ϕ_a^{mean} (x-axis) and the vertical shear of equivalent latitude anomaly ϕ_a^{diff} (y-axis). ϕ_a^{mean} and ϕ_a^{diff} are calculated from ERA-Interim reanalysis. The meridional advection patterns corresponding to the four corners are illustrated by schematics, with red lines denoting the tropopauses and black arrow denoting the meridional wind.

more likely to form double tropopauses than equatorward mean advection ($\phi_a^{mean} < 0$). Physically, this means that double tropopauses are more likely to be formed by the poleward advection of the higher tropopause than the equatorward advection of the lower tropopause. This is consistent with Castanheira and Gimeno (2011) where they found the poleward edge of double tropopause area is better correlated with the meridional extent of double tropopauses than the equatorward edge. The preferred poleward advection of tropospheric air is also suggested by Castanheira et al. (2012) where lower total column ozone is found for double tropopauses. Since ozone is rich in
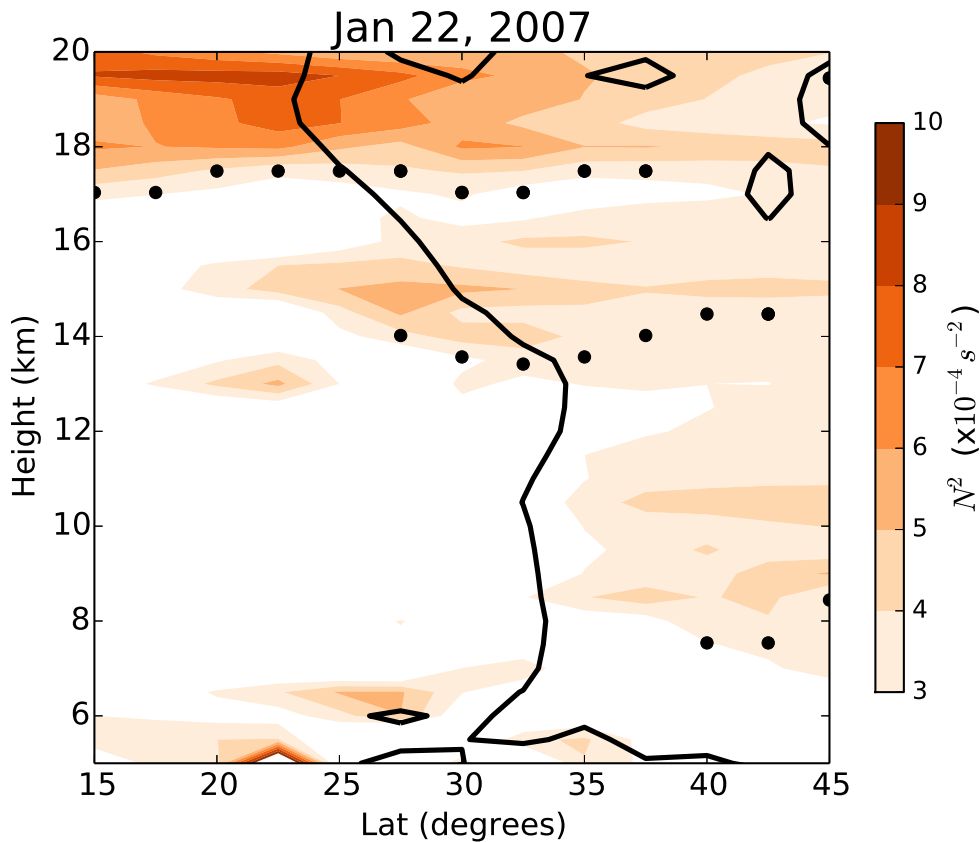
FIG. 3.8. Snapshots of the Brunt-Väisälä frequency N^2 (shading) from GPS temperature data and equivalent latitude contour ϕ_e=35° (black contour) from ERA-Interim reanalysis on Jan 22, 2007. The black solid circles denote the tropopause identified by GPS temperature data.

the stratosphere, lower column ozone indicates more tropospheric air in the column and hence

suggests a poleward tropospheric intrusion into the stratosphere.

3.4.2. DESTABILIZATION/VERTICAL STRETCHING

In the previous section we showed that approximately half of double tropopauses are formed

directly by differential advection. In this section we explore possible mechanisms for the formation

of the other 50%. Figure 3.8 shows a cross section of a double tropopause event that is not directly

caused by differential advection. The stacking of tropopauses occurs between 27°N and 38°N

where the N^2 field (shading) shows a clockwise folding. However, the equivalent latitude (ϕ_e)

contour of 30°N (contour) shows a counterclockwise folding. This contrasts with the cases shown in Figs. 3.4 where the ϕ_e contour approximately aligned with the N^2 contours, indicating that N^2 behaved largely as a passive tracer. In Fig. 3.8, the non-passive behavior of N^2 indicates that production/destruction processes of thermal stratification might be responsible for this double tropopauses event, such as the vertical stretching term B of (3.8).

Since stretching/compression is the only destruction/production process for adiabatic N^2, we quantify the accumulated effect of this stretching/compressing process by comparing N^2 with its passive counterpart in adiabatic situations. In particular, we conduct adiabatic eddy lifecycle simulations as described in Section 3.2.3 and initialize a passive tracer N_P^2 that has the same initial value as N^2. Then the difference $\Delta N^2 = N^2 - N_P^2$ quantifies the accumulated destruction/production of N^2, namely the effect of stretching/compression that destabilizes/stabilizes the thermal stratification . We further normalize ΔN^2 by N^2 to get the fractional change of N^2 due to stretching/compression.

The quantification of destabilization/stabilization and its role in forming double tropopauses during the eddy lifecycle simulations is summarized in Fig. 3.9. The left column shows a simulation with no TIL (hereafter TIL0) and the right column shows a simulation with a TIL of strength $c_H = 3K/km$ (hereafter TIL3). The upper row shows that TIL3 has double tropopauses in the cyclonic lobe of wave breaking (red shading) whereas TIL0 does not. Note that the identification of double tropopauses is the same as in WP11, replacing the 3K/km criteria in the WMO by 2K/km. Also shown in the upper row is N_P^2 (contour) which depicts the horizontal advection pattern. Despite the difference in double tropopause coverage between TIL0 and TIL3, there is no obvious reason that this difference is due to difference in the horizontal advection pattern. This suggests
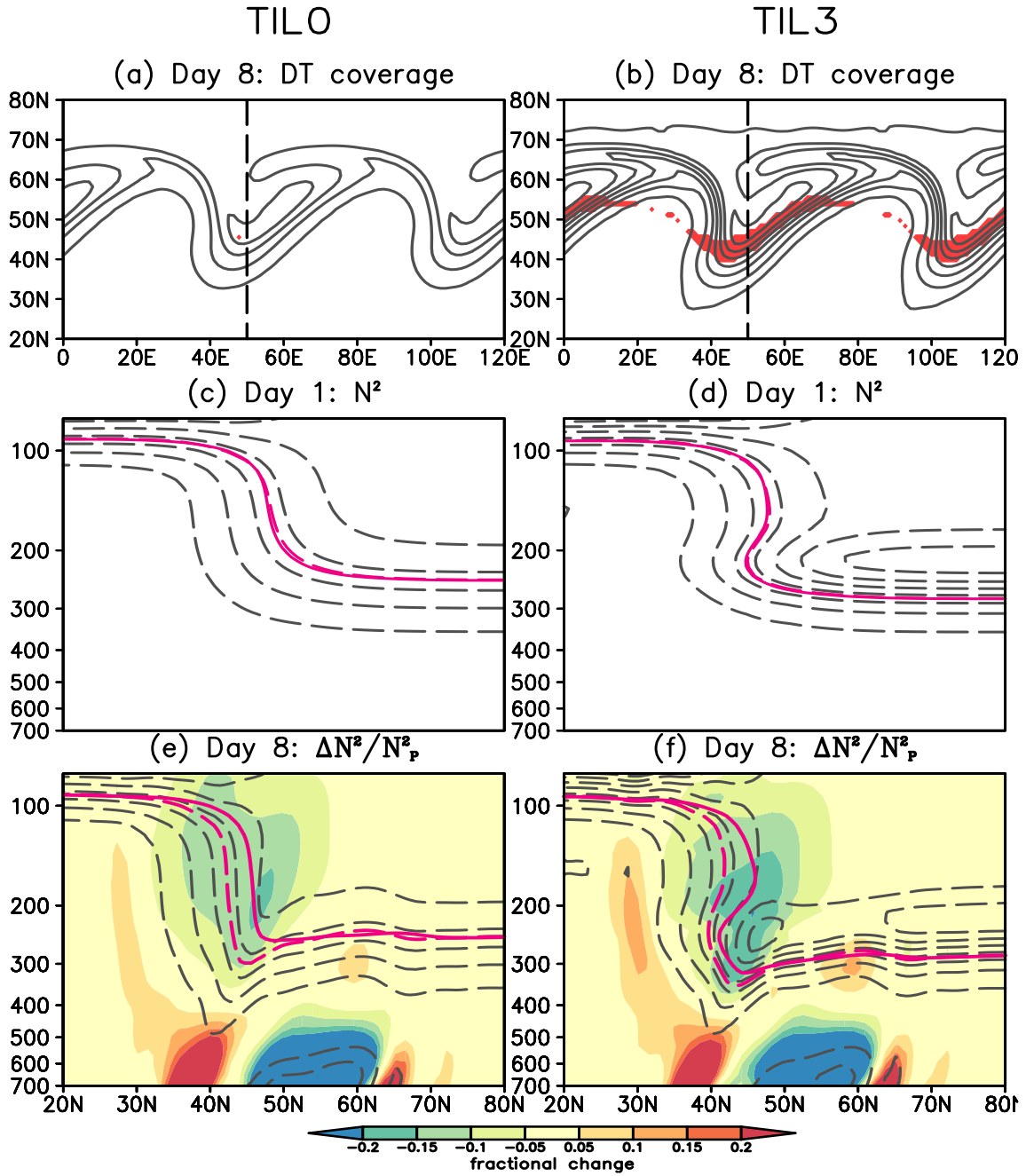
FIG. 3.9. **Left column:** (a) Concentration of N_P^2 tracer (contour) and the location of double tropopauses (red shading) in the simulation without an extratropical TIL. (c) Cross section of N_P^2 (dashed contour) and N^2 (solid line) along the dashed line shown in (a) on day 1. The contour of $3.3 \times 10^{-4} s^{-2}$ represents the thermal tropopause and is colored magenta. Black contours have an interval of $0.5 \times 10^{-4} s^{-2}$. (e) The contours are the same as in (c) but for day 8. The shading is the fractional material change in thermal stratification $\Delta N^2 / N_P^2$. **Right column:** The same as the left column, except for the simulation with an extratropical TIL.

that TIL may influence the formation of double tropopauses through some other mechanisms than horizontal advection.

The middle and bottom rows of Fig. 3.9 contrast cross sections of N^2 (solid contour) along with N_P^2 (dashed contour) on day 1 and day 8. The tropopause value ($3.3 \times 10^{-4}s^{-2}$) is colored by magenta for both N^2 and N_P^2 contours, so the solid magenta contour denotes the actual tropopause and the dashed magenta contour denotes the hypothetical tropopause if there were no stretching/compression. The two tropopause contours are same on day 1 but differ on day 8 in the tropopause break region between 40°N and 50°N. The fractional stretching/compression ($\Delta N^2/N_P^2$) that leads to such a change is plotted as shading in the bottom row. In particular, for both TIL0 and TIL3 it is the stretching (blue shading in Figs. 3.9e-f) in the tropopause break region that destabilizes the thermal stratification and hence causes the actual thermal tropopause to deviate from its hypothetical counterpart. However, the specific deviations are not the same for TIL0 and TIL3, as the former does not increase tropopause folding whereas the latter does. Interestingly, this is not due to the stretching (ΔN^2) but the initial N^2 that ΔN^2 adds to. In the case of TIL0, the stretching/destabilization destroyed the initial tropopause and created a new one above it between 40°N and 50°N, so that the net effect was to move the tropopause upward (Fig. 3.9e). In the case of TIL3, while the stretching created a new tropopause at higher levels, it was not able to destroy the lower initial tropopause because of the strong initial stratification (N^2) (Figs. 3.9d and 3.9f). The result is the stacking of two tropopauses between 40°N and 45°N. Due to these differences in the initial stratification – with or without a TIL – destabilizations of similar strength and spatial pattern lead to very different modification of the thermal tropopause.
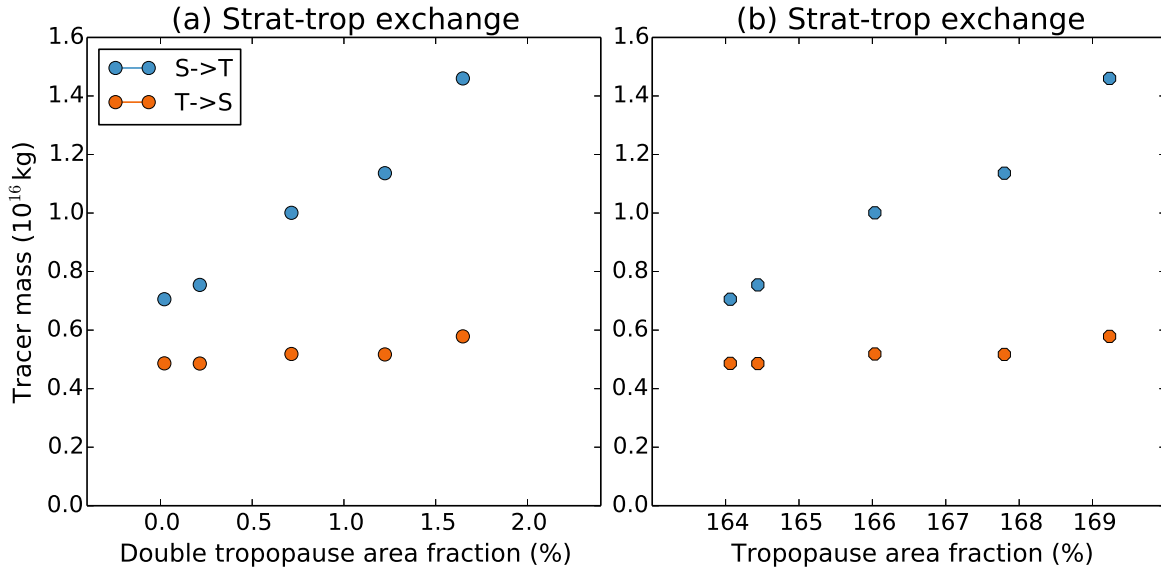
FIG. 3.10. Accumulated tracer mass flux between the stratosphere (S) and the troposphere (T) in idealized eddy lifecycle simulations as a function of (a) area fraction of double tropopauses coverage, and (b) area fraction of the tropopause. The area fraction is a unitless value defined as area divided by the global surface area.

3.5. ENHANCEMENT OF STRATOSPHERE-TROPOSPHERE EXCHANGE

Both double tropopauses and wave breaking are important processes that enhance the stratosphere-troposphere exchange by disturbing the tropopause interface. While detailed quantification of exchange during idealized wave breaking simulations was performed by Polvani and Esler (2007), the impact of double tropopauses on stratosphere-troposphere exchange has not been quantified to the best of our knowledge. Here, we ask to what extent the occurrence of double tropopauses enhances the stratosphere-troposphere exchange during wave breaking events. To answer this question, we use the same setting as in the previous section to generate idealized model simulations with various extents of double tropopauses. In particular, we simulate five eddy lifecycles (TIL0-TIL4) featuring initial TIL strength ranging from 0K/km to 4K/km (see Section 3.2.3.1 for details), with TIL0 and TIL3 also being used to study the formation mechanisms of double

tropause in Section 3.4.2. Then we apply the method of Polvani and Esler (2007) to quantify the corresponding strength of the stratosphere-troposphere exchange. In words, we quantify the amount of stratospheric tracer in the troposphere and the amount of tropospheric tracer in the stratosphere as the two-way mass exchange across the tropopause (see 3.2.3.2 for details). The results are plotted in Fig. 3.10a as a function of double tropopause area fraction (the coverage area divided by global surface area $4\pi a^2$). As the area fraction of double tropopauses increases, the troposphere-to-stratosphere exchange stays largely unchanged but the stratosphere-to-troposphere exchange increases substantially, as much as double the magnitude when no double tropopause is present.

One way double tropopauses may amplify the stratosphere-to-troposphere exchange during wave breaking is by increasing the area of the tropopause by vertical folding. As the tropopause area increases, there exists a larger interface between the stratosphere and the troposphere for transport and mixing to occur and thus, this might lead to more exchange of air mass. We test this by calculating the total tropopause area (A_{TP}) as the area of the isosurface S=T=0.5 during these experiments. We then plot the mass exchange as a function of $A_{TP}/4\pi a^2$ in Fig. 3.10b. As the tropopause area increases, the troposphere-to-stratosphere exchange stays largely unchanged but the stratosphere-to-troposphere exchange increases significantly, similar to Fig. 3.10a. This provides evidence that the increase in the tropopause area is the mechanism by which double tropopauses enhance the stratosphere-troposphere exchange. Combining this with the results shown in Fig. 3.9b, we argue that the increased tropopause area by double tropopauses in wave breaking lobes can substantially enhance the strength of stratosphere-to-troposphere exchange.

3.6. CONCLUSIONS AND DISCUSSION

Using COSMIC GPS data, ERA-Interim reanalysis, and eddy lifecycle simulations of the GFDL dynamical core, we investigate the synoptic features and transport/mixing strength of double tropopauses, as well as the adiabatic mechanisms responsible for their formation. In particular, we address three questions with their summarized answers below:

(1) *What is the relationship between double tropopauses and Rossby wave breaking in the observations?*

In a composite sense, anticyclonic and cyclonic wave breaking are both linked to increased double tropopause occurrence (Fig. 3.6), and double tropopause occurrence in certain regions also shows the signature of both types of wave breaking (Fig. 3.5).

(2) *What are the mechanisms responsible for double tropopause formation?*

We propose two mechanisms. The first one is differential advection of thermal stratification that leads to the folding of the thermal tropopause (Fig. 3.4). In particular, Rossby wave breaking helps form double tropopauses by providing such differential advection in the observations (Fig. 3.6). Climatologically, approximately 50% of all the double tropopauses are formed by this mechanism (Fig. 3.3). The second mechanism is the creation of the tropopause by destabilizing the thermal stratification in the presence of a TIL (Fig. 3.9).

(3) *How do double tropopauses impact stratosphere-troposphere exchange?*

In idealized eddy lifecycle simulations, the occurrence of double tropopauses substantially enhances the stratosphere-to-troposphere exchange (Fig. 3.10), whereas the troposphere-to-stratosphere exchange is largely unchanged. We suggest that the enhancement is due to increased tropopause area corresponding to the folding tropopause.

Previous research suggested that cyclonic flow is preferred near double tropopauses (e.g. Randel et al. 2007a; Wang and Polvani 2011). The destabilization/stretching mechanism can potentially explain this preference. When an air parcel is adiabatically stretched/destabilized, the pseudo-density $\sigma = -\frac{1}{g}\frac{\partial p}{\partial \theta}$ increases. To conserve $PV = (f + \zeta)/\sigma$, absolute vorticity $f + \zeta$ has to increase. For baroclinic waves, this increase is a result of an increase in relative vorticity ζ rather than f (not shown). Therefore, relative vorticity is likely to be positive in the presence of adiabatic stabilization.

In the eddy lifecycle simulations, double tropopauses only enhance the equatorward stratosphere-to-troposphere exchange, which is inconsistent with the dominant poleward advection associated with double tropopauses in the observations. The reason for the equatorward enhancement in our idealized simulation may be that the double tropopauses only occur in the equatorward lobe of the breaking wave where the exchange across the tropopause is dominated by an equatorward flux (not shown). However, in observations double tropopauses occur in both poleward and equatorward lobes of wave breaking (Fig. 3.6) and poleward advection is more favorable for double tropopauses (e.g. Randel et al. 2007a; Pan et al. 2009; Castanheira and Gimeno 2011). Therefore, double tropopauses in the observations may actually predominantly enhance poleward mixing of tropospheric air into the stratosphere. More research is needed to test this.

Our study focuses on adiabatic mechanisms of double tropopause formation by synoptic waves. However, there are certainly other mechanisms that are relevant. One example is mean advection. Specifically, we depict the advection we are interested in by equivalent latitude anomaly ϕ_a, which excludes the influence of mean advection. Birner (2010) showed that the climatological mean meridional structure of N^2 exhibits slight folding in the subtropics and mean advection contributes to this folding. Another component we neglect is the diabatic change in thermal stratification by

radiative processes involving ozone and water vapor. Studies have shown their role in forming a TIL (e.g. Randel et al. 2007b; Ferreira et al. 2015; Kunkel et al. 2016). It is possible these diabatic processes can influence the formation of double tropopauses directly, or indirectly by their ability to modify TIL.

Among the results, perhaps the most striking one is how much double tropopauses can enhance the stratosphere-to-troposphere exchange in idealized eddy lifecycles which are themselves strong in transport and mixing to begin with (e.g. Polvani and Esler 2007). Given the ubiquitousness of double tropopauses in the observations, they likely play a significant role in the stratosphere-troposphere exchange and account for its variability at least on synoptic time scales. Our results regarding their linkage to wave breaking and their formation mechanisms may then help advance understanding of the variability of the global stratosphere-troposphere exchange.

CHAPTER 4

QUANTIFYING ISENTROPIC MIXING LINKED TO ROSSBY WAVE BREAKING IN

A MODIFIED LAGRANGIAN COORDINATE

4.1. INTRODUCTION

Atmospheric transport and mixing play a fundamental role in the global distribution of chemical pollutants and moisture. In the extratropics, transport and mixing by eddies are known to mainly operate along isentropic surfaces, i.e. constant potential temperature (θ) surfaces. Within the troposphere, warm conveyer belts embedded in extratropical cyclones transport warm moist air poleward and upward along sloped isentropes (e.g. Thorncroft et al. 1993; Madonna et al. 2014). These transport events are responsible for poleward moisture transport (e.g. Eckhardt et al. 2004) and pollutant transport into the Arctic (e.g. Raatz and Shaw 1984; Barrie 1986). In the upper troposphere, vigorous exchange between stratospheric and tropospheric constituents happens along isentropes across a folding tropopause (e.g. Shapiro 1980). Such exchange is an important source of ozone in the troposphere (e.g. Lelieveld and Dentener 2000) where it is considered a pollutant and is detrimental to human health (e.g. Lippmann 1989). This exchange also injects anthropogenic trace species such as chlorofluorocarbon (CFC) into the stratosphere (Holton et al. 1995).

Due to the dominance of isentropic transport and mixing in the extratropics, θ is often used as the vertical coordinate in quantifying these processes. Under the adiabatic approximation, θ can be considered a material surface and hence a Lagrangian coordinate. A Lagrangian coordinate is a more natural choice than a Eulerian one for transport and mixing since it avoids the need for Stokes correction for artifacts arising from the Eulerian-mean (McIntyre 1980). With θ being the vertical coordinate, reversible vertical oscillations are absent and any vertical flux is associated

with diabatic heating. Along these same lines, it is natural to also choose a conserved variable as the meridional coordinate so that any meridional flux in such a coordinate is only associated with non-conservative processes, such as horizontal diffusion. Examples include using potential vorticity (PV) or the concentration of a passive tracer as the meridional coordinate (e.g. Butchart and Remsberg 1986). By integrating quantities between contours of a conserved quantity, a general description of the irreversible mixing is possible without expensive trajectory calculations (e.g. Nakamura 1995, 1996; Haynes and Shuckburgh 2000a).

As there are many ways to quantify isentropic mixing, there are many physical processes that drive them. Among them, Rossby wave breaking (RWB) is an important one both within the troposphere and across the tropopause. Near the tropopause, RWB has been shown by numerous studies to be associated with the exchange of mass or chemical tracers between the stratosphere and the troposphere (e.g. Appenzeller and Davies 1992; Trepte et al. 1993; Chen 1995; Appenzeller et al. 1996a; Jing et al. 2004). Especially strong exchange occurs in the presence of a double tropopause (e.g. Randel et al. 2007a; Pan et al. 2009; Liu and Barnes 2017b) which is a feature related to RWB (e.g. Wang and Polvani 2011; Liu and Barnes 2017b). In the troposphere, we will show that RWB is also closely linked to isentropic mixing.

RWB can be classified into two distinct types – anticyclonic wave breaking (AWB) and cyclonic wave breaking (CWB), and the frequency of each is strongly coupled to the midlatitude jet stream. Climatologically, AWB occurs most frequently on the equatorward flank of the jet where the horizontal wind shear is anticyclonic, while CWB occurs most frequently on the poleward flank of the jet. As the jet shifts poleward, the total frequency of AWB increases whereas that of CWB decreases (e.g. Strong and Magnusdottir 2008; Woollings et al. 2008; Rivière 2011; Barnes and Hartmann 2012). This RWB-jet position relationship is especially important because the jet

stream position is very responsive to both internal climate variability such as the El-Niño Southern Oscillation (ENSO) (e.g. Rasmusson and Wallace 1983; Chen and van den Dool 1999; Ren et al. 2008), and external climate forcings such as increasing greenhouse gas concentrations and ozone depletion (e.g. Thompson and Solomon 2002; Butler et al. 2010; Barnes and Polvani 2013). It is through such coupling that RWB is linked to climate variability on different time scales, and thus, can drive the variability of global transport and mixing of various chemical tracers.

Quantifying the isentropic mixing by RWB is thus key to understanding the variability of the climate-scale distribution of various chemical tracers. Polvani and Esler (2007) (hereafter PE07) quantified the two-way mixing across the tropopause associated with the two types of RWB in idealized eddy lifecycle simulations. They found that CWB exhibits stronger mixing from the stratosphere to the troposphere compared to AWB. Considering the coupling of the jet stream position and AWB vs. CWB frequency, such a difference has significant implications since it may translate into a change in total mixing when the jet stream shifts. In this work, we explore these implications by asking two questions: (1) Is there a robust asymmetry in isentropic mixing efficiency between AWB and CWB? (2) How does this asymmetry, if it exists, translate into a dependence of total mixing on jet variability?

The paper is organized as follows. A description of the numerical simulations is given in section 4.2. In section 4.3, we describe a modified Lagrangian (MLM) framework to quantify isentropic mixing. Section 4.4 explores mixing linked to both types of RWB, and tests the robustness of the difference between AWB and CWB. Section 4.5 shows how such a difference can impact total mixing as the the jet-stream shifts. Conclusions are given in section 4.6.

4.2. MODEL SETUPS

All simulations in this study are performed by integrating a primitive equation model with no topography. The specific model used is the Geophysical Fluid Dynamics Laboratory (GFDL) spectral dry dynamical core with a horizontal resolution of T42, and an integrating time step of 1200 seconds. The model uses ∇^8 horizontal hyperdiffusion for dynamical variables such as temperature, vorticity and divergence. There is no explicit vertical diffusion for any variable in this model.

With the same model setup described above, we carry out two different sets of simulations. The first set of simulations are idealized eddy lifecycle simulations with initialized passive tracers that follow PE07 (to be discussed in detail). The second simulation is an idealized climate run based on Held and Suarez (1994).

4.2.1. IDEALIZED EDDY LIFECYCLE SIMULATION

Following PE07, we reproduce the two idealized eddy lifecycles (LC1 and LC2) first introduced by Thorncroft et al. (1993). The model is configured with 30 unevenly spaced vertical layers and no diabatic heating during the 20-day run. In both the LC1 and LC2 simulations, only the initial conditions are prescribed. For LC1, a baroclinically unstable jet is prescribed on day 1 and the eddies grow and break anticyclonically at the late stages of the lifecycle, which corresponds to AWB in the real atmosphere. The initial zonal wind is given by:

$$u_1(\phi, z) = U_0 F(\phi)[(z/z_T)e^{-[(z/z_T)^2 - 1]/2}] \tag{4.1a}$$

$$
F(\phi) = \begin{cases} [sin(\pi(sin\phi)^2)]^3, & \text{for } \phi > 0 \\ \\ 0, & \text{for } \phi < 0. \end{cases} \tag{4.1b}
$$

where $z \equiv H \log(p_0/p)$ is the log-pressure height. For LC2, the initial zonal wind is obtained by

adding a bottom-heavy cyclonic shear u_s to the initial wind profile for LC1,

$$
u_2(\phi, z) = u_1(\phi, z) + u_s(\phi, z) \tag{4.2a}
$$

$$
u_s(\phi, z) = -U_s e^{-z/z_s} [sin(2\phi)]^2 [\frac{\phi - \phi_s}{\Delta_s}] e^{-[\frac{\phi - \phi_s}{\Delta_s}]^2} \tag{4.2b}
$$

In the LC2 simulation the eddies grow and break cyclonically at the late stages of the lifecycle,

which corresponds to CWB. The constants appearing in (4.1) and (4.2) are the same as those in

PE07. For both lifecycles, the initial conditions for temperature and surface pressure are set to be

in thermal wind balance with the zonal wind profiles prescribed in (4.1) and (4.2). In addition to

the balanced temperature profile, a wavenumber-6 perturbation centered at $45°$N is added to the

initial temperature field to give rise to the growing eddies.

For both the LC1 and LC2 simulations, the tracer setup is similar to PE07 in that we ini-

tialize two passive isentropic tracers: a stratospheric tracer (S) and a tropospheric tracer (T) on

isentropes ranging from 290K to 380K. The initial tropopause is defined (as in PE07) as a nearly

vertical boundary that partitions isentropes into a poleward half (stratosphere) and a equatorward

half (troposphere) (see Fig. 5 in PE07). The initial concentrations of the two tracers are set such

that poleward of the initial tropopause $S = 1$ and $T = 0$, while equatorward of it $T = 1$ and

$S = 0$. Since the simulations are adiabatic, $S + T = 1$ on isentropes from 290K to 380K at all

times by construction. During the simulations, the tropopause is defined by an evolving boundary between the two tracers as the contour of $S = T = 0.5$. Both S and T are spectral tracers and a ∇^8 hyperdiffusion is applied at each time step. We refer readers to PE07 for additional details.

4.2.2. IDEALIZED CLIMATE SIMULATION

We perform a climate simulation forced by the idealized diabatic heating scheme proposed by Held and Suarez (1994). Specifically, we set the diabatic heating as a relaxation to a prescribed zonally-symmetric equilibrium temperature profile:

$$T_{eq} = max \left\{ 200K, \; \left[315K \underbrace{-(\Delta T)_y sin^2\phi}_{A} \underbrace{-(\Delta \theta)_z log \left(\frac{p}{p_0} \right) cos^2\phi}_{B} \underbrace{-\epsilon sin\phi}_{C} \right] \underbrace{\left(\frac{p}{p_0} \right)^\kappa}_{D} \right\} \quad (4.3)$$

For this relaxation scheme, the individual terms in (4.3) are equivalent to constant heating or cooling terms. Idealized as it is, (4.3) includes the most essential elements of climate forcing – heating in low latitudes and cooling in high latitudes, as represented by term A. Term B is a modification for the tropics, as manifested by the $cos^2\phi$ factor. Without term B, but with the inclusion of factor D, (4.3) would yield an atmosphere that was stratified dry adiabatically. Term B thus can be thought of as a representation of stabilization by moist convection in the tropics which is not represented explicitly in this model setup. Term C adds a hemispheric asymmetry to the equilibrium temperature that accounts for seasonality in radiative forcing. In this study we set $\epsilon = 10$ which represents winter conditions in the Northern Hemisphere. We focus on winter because the eddy activity is strongest in winter when the baroclinicity is largest. In addition, the low frequency variability that modulates eddy activity (e.g. the annular mode) is also strongest in the winter.

While the equilibrium temperature profile given in (4.3) leads to a midlatitude circulation that is generally representative of that is observed, there are still noticeable differences, especially in the

tropics. For example, the Hadley cell in this dry general circulation model (GCM) is substantially weaker than in observations (e.g. Walker and Schneider 2006). However, the main purpose of this simulation is not to reproduce the observed circulation exactly (there is no topography, for example), but to serve as a stepping stone between the unforced eddy lifecycle simulation and reality by removing the complexities of full GCMs that are not essential for isentropic mixing.

To study isentropic mixing, we initialize a spectral tracer that serves as our Lagrangian coordinate. The tracer can be thought of having a source in the boundary layer from $60°$S to $60°$N and a sink that includes the entire free atmospheric column at the poles so that an equator-to-pole gradient in tracer concentration is maintained along isentropic surfaces. As will be explained in the next section, this monotonic meridional gradient of the tracer is required for our tracer coordinate system. In the sink region anywhere poleward of $85°$N or $85°$S, the tracer concentration is damped exponentially with an e-folding timescale of 6 hours. In the source region within the boundary layer, the tracer concentration is set to

$$\frac{1}{4.5}\left[3.7 - P_2(sin\phi) - P_4(sin\phi)\right] \tag{4.4}$$

where P_2 and P_4 are the second and fourth order Legendre polynomials respectively. (4.4) is qualitatively similar to a tracer concentration of 1 from $60°$S to $60°$N and 0 elsewhere in the boundary layer, but with a gradual transition from 1 to 0 on the edges, which prevents spurious tracer concentration during integration due to the Gibbs effect. The tracer is otherwise passive throughout the rest of the atmosphere. As in the lifecycle simulations, a ∇^8 hyperdiffusion is used for the spectral tracer.

With the setup described above, the model is run with 20 evenly spaced sigma levels for 25 years. We use the last 22 years for analysis which allows for a spin-up period of about 1000 days. All of the variables are output every 6 hours.

4.3. QUANTIFICATION OF ISENTROPIC MIXING

4.3.1. MODIFIED-LAGRANGIAN-MEAN FRAMEWORK AND THE TRACER EQUATION

Viewed in an Eulerian framework, the distribution of a passive tracer can be accounted for by two processes: advective fluxes and diffusive fluxes. The idea of a modified Lagrangian coordinate is to reformulate the Eulerian tracer equation in a flow-following two-dimensional coordinate so that reversible advective fluxes are absent. Specifically, we can choose potential temperature (θ) as the vertical coordinate, and the concentration of a passive tracer (q) as the meridional coordinate. As shown by Nakamura (1995), under such a coordinate transformation, the mass continuity equation becomes:

$$\left.\frac{\partial \mathcal{M}\{1\}}{\partial t}\right|_{q,\theta} = -\left.\frac{\partial \mathcal{M}\{\dot{q}\}}{\partial q}\right|_{\theta,t} - \left.\frac{\partial \mathcal{M}\{\dot{\theta}\}}{\partial \theta}\right|_{q,t} \tag{4.5}$$

where $\dot{q}$ and $\dot{\theta}$ are the material derivatives of q and θ, and

$$\mathcal{M}\{\ \} \equiv \iint\limits_{q^* \leqslant q} \{\ \}\sigma dA \tag{4.6}$$

in which $\sigma \equiv -g^{-1}\frac{\partial p}{\partial \theta}$ is the pseudo-density in isentropic coordinates. Note that in the climate simulation q decreases with latitude as determined by the sources and sinks of our passive tracer. On the *lhs* of (4.5) is the mass tendency within a contour of q. The first term on the *rhs* of (4.5) accounts for horizontal transport of mass across a contour of q due to diffusion, while the second

term represents the differential vertical transport of mass across isentropic surfaces due to diabatic heating.

To obtain a tracer equation from (4.5), we largely follow Nakamura (1996) except that we utilize the one-to-one relationship between a tracer contour q and the *mass* enclosed by it $m \equiv \mathcal{M}\{1\}$, rather than *area* enclosed. In particular, on each isentrope one can obtain the following relationship between q and m by holding $m(q,t)$ fixed over time:

$$\frac{dm(q,t)}{dt} = \left.\frac{\partial m}{\partial t}\right|_q + \frac{\partial m}{\partial q}\left.\frac{\partial q}{\partial t}\right|_m = 0 \tag{4.7}$$

Plugging (4.7) into (4.5) leads to the tracer equation in the mass coordinate:

$$\left.\frac{\partial q}{\partial t}\right|_{m,\theta} = \left.\frac{\partial \mathcal{M}\{\dot{q}\}}{\partial m}\right|_{\theta,t} + \frac{\partial q}{\partial m}\left.\frac{\partial \mathcal{M}\{\dot{\theta}\}}{\partial \theta}\right|_{q,t} \tag{4.8}$$

Note that this is equivalent to the tracer equation used in Leibensperger and Plumb (2014) but without further coordinate transformation. On the *lhs* is the time tendency of the value of a tracer contour that encloses a fixed mass m. The first term on the *rhs* is the convergence of diffusive tracer flux which is down-gradient in general. The second term represents the contribution of diabatic mass circulation and is analogous to "advection" in an advection-diffusion sense (Leibensperger and Plumb 2014).

In the case of non-divergent barotropic flow ($\sigma = \sigma_0$), the second term on the *rhs* of (4.8) vanishes. The diffusive term $\mathcal{M}\{\dot{q}\}$ then accounts for the tracer distribution alone and is the one closely linked to Rossby wave breaking (to be shown later). In this study, we focus on this diffusive term not only due to its linkage to wave breaking, but also due to its dominance in the midlatitudes in determining zonally averaged tracer distributions (e.g. Plumb and Mahlman 1987).

The diffusive nature of term $\mathcal{M}\{\dot{q}\}$ can be revealed by such a flux-gradient relationship assuming $\dot{q} = \kappa \nabla^2 q$ (Nakamura 1996):

$$\mathcal{M}\{\dot{q}\} = \sigma_0 \kappa L_{eq}^2 \frac{\partial q}{\partial A} \tag{4.9}$$

where $A(q, \theta, t)$ is the area enclosed by a contour q, and

$$L_{eq}^2 = \frac{\partial}{\partial A} \iint |\nabla_\theta q|^2 dA / (\frac{\partial q}{\partial A})^2 \tag{4.10}$$

L_{eq} is called equivalent length and leads to the definition of effective diffusivity (Haynes and Shuckburgh 2000a):

$$\kappa_{eff}^* = \kappa \frac{L_{eq}^2}{(2\pi a cos\phi)^2} \tag{4.11}$$

Since L_{eq}^2 is positive definite, the sign of flux $\mathcal{M}\{\dot{q}\}$ is down-gradient in this instance. In other word, $\mathcal{M}\{\dot{q}\}$ is diffusive in nature.

4.3.2. CALCULATION OF THE ISENTROPIC DIFFUSIVITY

To calculate the diffusive flux term in (4.8), we need to first determine the mass values to use as coordinates. For both idealized eddy lifecycle simulations and the climate simulation, we pick 16 values of m for each isentropic level in the Northern Hemisphere by their one-to-one relationship with equivalent latitude ϕ_e:

$$m(\phi_e) = \iint\limits_{\phi \geq \phi_e} \overline{\sigma} dS \tag{4.12}$$

where $\overline{\sigma}$ is the climatological mean pseudo density. Specifically, we first evenly pick 16 ϕ_e values ranging from $0°N$ to $85°N$ and then obtain 16 corresponding m by applying (4.12).

The diffusive flux $\mathcal{M}\{\dot{q}\}$ in (4.8) is then calculated as area integral of $\sigma\dot{q}$ at each $\phi_e(m)$. $\dot{q}$ is calculated as the 4th order hyperdiffusion in the model, and we output 6-hourly accumulated $\dot{q}$

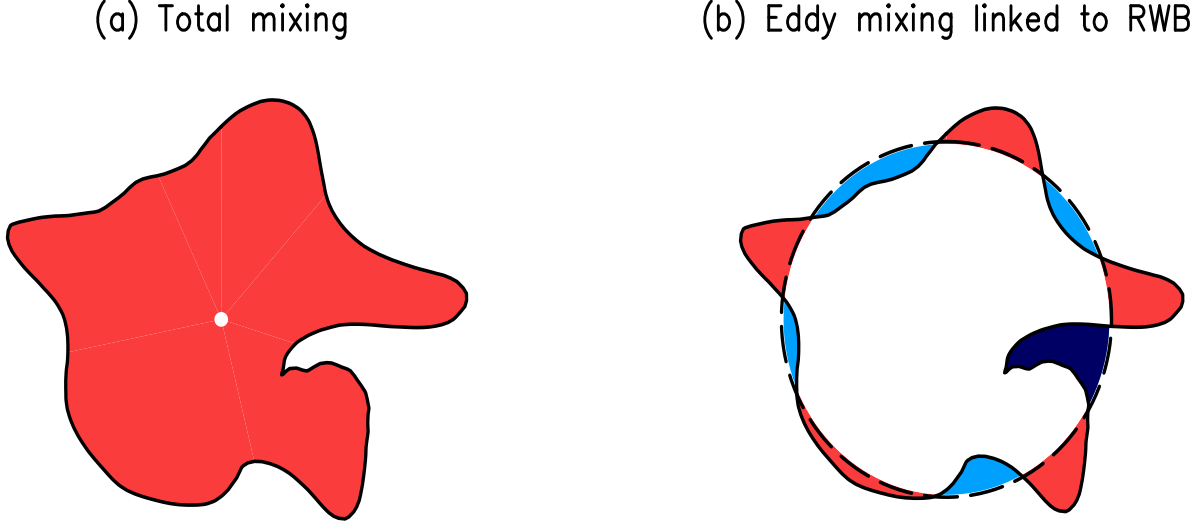(a) Total mixing   (b) Eddy mixing linked to RWB

FIG. 4.1. Schematics depicting the integration area for total mixing (left) and eddy mixing (right) terms. (a) illustrates the calculation of total mixing. (b) illustrates the mixing by waves (all shading), and the part related to Rossby wave breaking (dark blue shading). See text for additional details.

and interpolate it and σ on isentropic surfaces following the interpolation scheme of Edouard et al. (1997). The integration area for $\mathcal{M}\{\dot{q}\}$ is illustrated in Fig. 4.1a. For the climate simulation, we are especially interested in mixing driven by eddies. To serve this purpose, we partition the integration of $\mathcal{M}\{\dot{q}\}$ into two parts following previous studies (e.g. Nakamura and Zhu 2010; Chen and Plumb 2014):

$$\mathcal{M}\{\dot{q}\} = \overline{\mathcal{M}}\{\dot{q}\} + \Delta\mathcal{M}\{\dot{q}\} \tag{4.13}$$

The first term is $\overline{\mathcal{M}}\{\dot{q}\}$ which represents the integration poleward of an equivalent latitude circle (ϕ_e). The integration area for this term is indicated by the black dashed circle in Figs. 4.1b. This term is driven only by diffusion. The second term is $\Delta\mathcal{M}\{\dot{q}\}$ which is driven by zonal asymmetries in the flow (i.e. eddies). The integration area of this term is indicated by the shading in Fig 4.1b where the red area is weighted by 1 and the blue area is weighted by -1. $\Delta\mathcal{M}\{\dot{q}\}$ (from now on referred to as eddy mixing) is the component we focus on here.

As suggested by (4.9), eddy mixing flux $\Delta\mathcal{M}\{\dot{q}\}$ is determined by both dynamics (diffusivity) and specific tracer distributions (tracer gradient). We are only interested in the more general dynamical part since its behavior is transferable to any other tracer. This part is referred to as eddy diffusivity and can be calculated as $\Delta\mathcal{M}\{\dot{q}\}$ normalized by the tracer gradient and mean mass density suggested by (4.9) and (4.11), that is, $\Delta\mathcal{M}\{\dot{q}\}/(\overline{\sigma}^L\frac{\partial q}{\partial\phi_e})$, where $\overline{\sigma}^L$ is the average pseudo-density over a tracer contour in the climatological mean. Note that this expression of eddy diffusivity is very similar to that of Chen and Plumb (2014). The main difference is that they employ a hybrid Eulerian-Lagragian coordinate whereas we use a Lagrangian coordinate. In the rest of the paper, we use this eddy diffusivity to represent isentropic mixing strength.

4.3.3. LINKING ISENTROPIC MIXING TO ROSSBY WAVE BREAKING

In this study, we separate mixing by the overturning direction of Rossby wave breaking – anticyclonic and cyclonic – due to the robust dynamical relationship between the two types of wave breaking and the jet streams (e.g. Barnes and Hartmann 2012). Note that Nakamura (2004) separates mixing into a poleward and an equatorward component. Since cyclonic and anticyclonic wave breaking events are comprised of a combination of poleward and equatorward mixing, our approach is distinct from this earlier work. For our idealized lifecycle simulations, linking isentropic mixing to the two types of wave breaking is straightforward. As in PE07, we assume all of the mixing in the LC1 simulation is linked to AWB while all of the mixing in the LC2 is linked to CWB. However, for the climate simulation in which AWB and CWB coexist every day along with other non-breaking waves, we need a dedicated algorithm to separate the contribution from the two types of wave breaking from all of the other processes. To serve this purpose, we first detect the two types of RWB in the model output. Unlike some previous studies where contours of potential vorticity (PV) on isentropes are used to identify wave breaking events (e.g. Strong and

76

Magnusdottir 2008; Liu et al. 2014; Liu and Barnes 2015), we base our algorithm on the tracer contours themselves. In fact, the contours of the tracer q in our climate simulation align well with PV contours on isentropic surfaces and thus our method is very similar to that of previous studies (not shown). The reason we favor q over PV for RWB detection is that our quantification of the mixing is based on q contours already. Thus, using q to detect RWB is natural for linking mixing to RWB events in this framework.

Specifically, we detect RWB based on wave lobes illustrated in Fig 4.1b. If the leftmost/rightmost point of one lobe is to the left/right of its base line (shown as black dashed segments), then we identify the lobe as overturning. We require the extent of overturning be at least $5.5°$ of longitude to exclude small scale disturbances that are not linked to large-scale RWB. Then, according to the direction of overturning, we partition the overturning lobes into AWB and CWB. For example, in Fig 4.1b the overturning lobe is identified as CWB and marked by dark blue shading. The eddy mixing $\Delta \mathcal{M}(\dot{q})$ associated with this CWB lobe is the integration over the dark blue area in Fig 4.1b. The frequency of occurrence of RWB is defined as the ratio of RWB area to the total wave area (e.g. dark blue versus all shading in Fig 4.1b). We compared the climatology of RWB frequency obtained by this method with that obtained by an algorithm using PV contours (Liu et al. 2014; Liu and Barnes 2015). They agree well with each other (not shown), thus further supporting our use of q contours for identifying RWB in this study.

A caveat should be raised about local RWB contribution to isentropic mixing. Since the divergence theorem does not hold for local integration, (4.9) does not necessarily hold for the RWB contribution. In other words, the local contribution to mixing is not guaranteed to be down-gradient although the total mixing is, provided that the diffusion takes the form of $\dot{q} = \kappa \nabla^2 q$.

4.4. ISENTROPIC MIXING LINKED TO THE TWO TYPES OF ROSSBY WAVE BREAK-ING

Figure 4.2 illustrates distinct mixing features associated with the two types of Rossby wave breaking by showing snapshots of tracer S on the 335K isentrope in the two idealized wave breaking simulations. Orange indicates the stratosphere and blue indicates the troposphere. On day 8, the anticyclonic overturning in LC1 is depicted by the blue shading equatorward of the tropopause (denoted by the black dashed line), and the cyclonic overturning in LC2 is depicted by orange shading poleward of the tropopause (Fig. 4.2c and 4.2d respectively). It is evident in Fig. 4.2c and 4.2d that CWB in LC2 is much more active in stretching and overturning the tropopause compared to AWB in LC1. As a result, there is a larger interface between the S and T tracers for mixing to work on for CWB. Consistent with this picture, PE07 documented 50% stronger stratosphere-to-troposphere mixing in LC2 than in LC1.

Our goal for this section is to paint a more comprehensive picture for the mixing features linked to the two types of wave breaking provided by a more realistic climate simulation. By applying a wave breaking detection algorithm and modified-Lagrangian-mean diagnostic for mixing, we investigate the spatial distribution and efficiency of RWB-driven mixing on isentropes ranging from the troposphere to the lower stratosphere.

Figure 4.3 shows the climatology of isentropes (solid line) in pressure coordinates from the idealized climate simulation. The shading denotes the range of isentropes (270K-350K) on which we quantify mixing of the idealized tracer. We further divide the shaded area into the middle-world (green shading, 300K-350K) and the underworld (pink shading, 270K-295K) (e.g. Shaw and Austin 1930; Hoskins 1991). The underworld is defined by isentropes that are always below the tropopause denoted by a black dashed line, while the middleworld is defined by isentropes
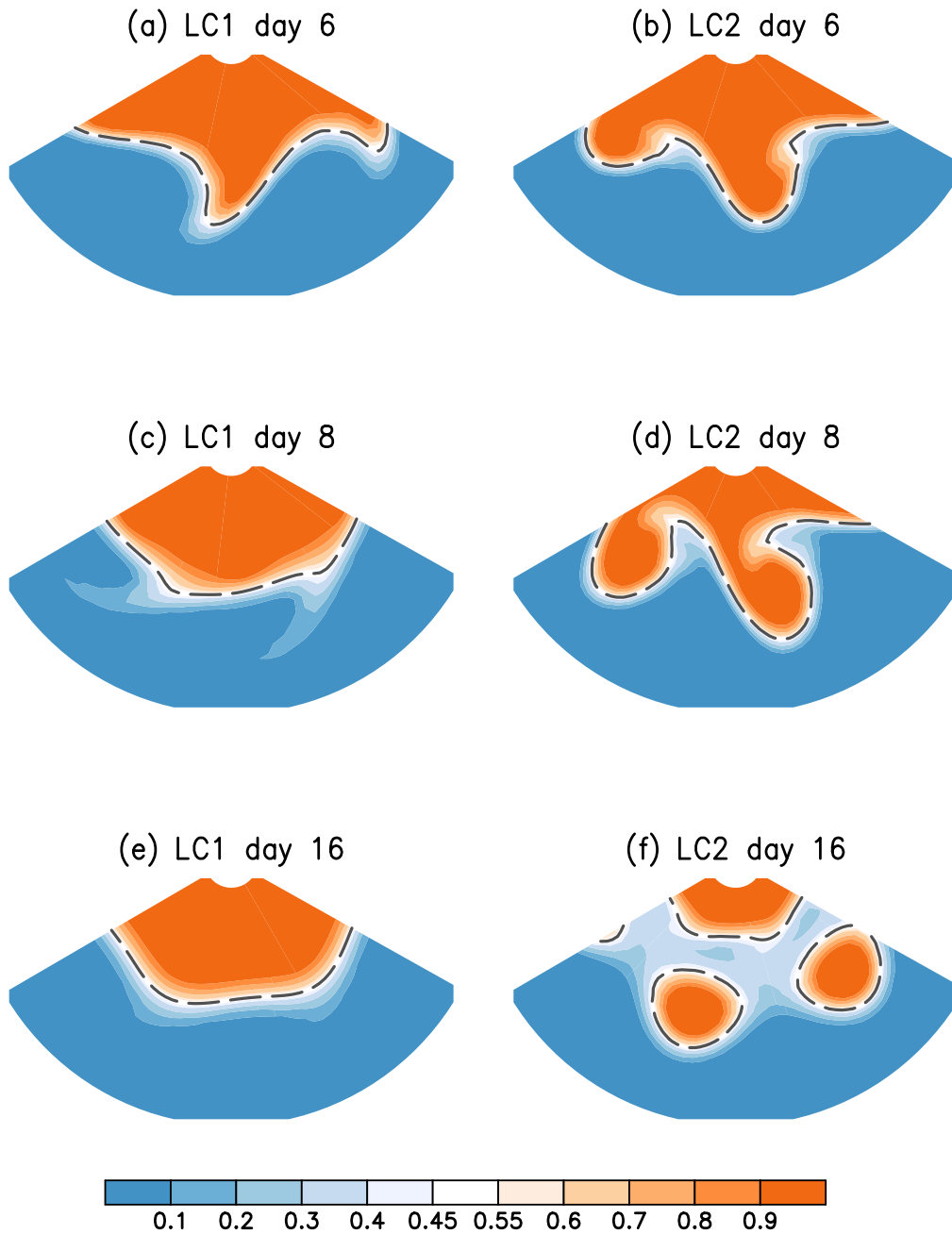
FIG. 4.2. Snapshots of the concentration of the stratospheric tracer (shading) on the 335K isentrope in the idealized LC1 (left column) and LC2 (right columns) simulations. Dashed contours denote the tropopause defined as the 0.5 contour of the stratospheric tracer.
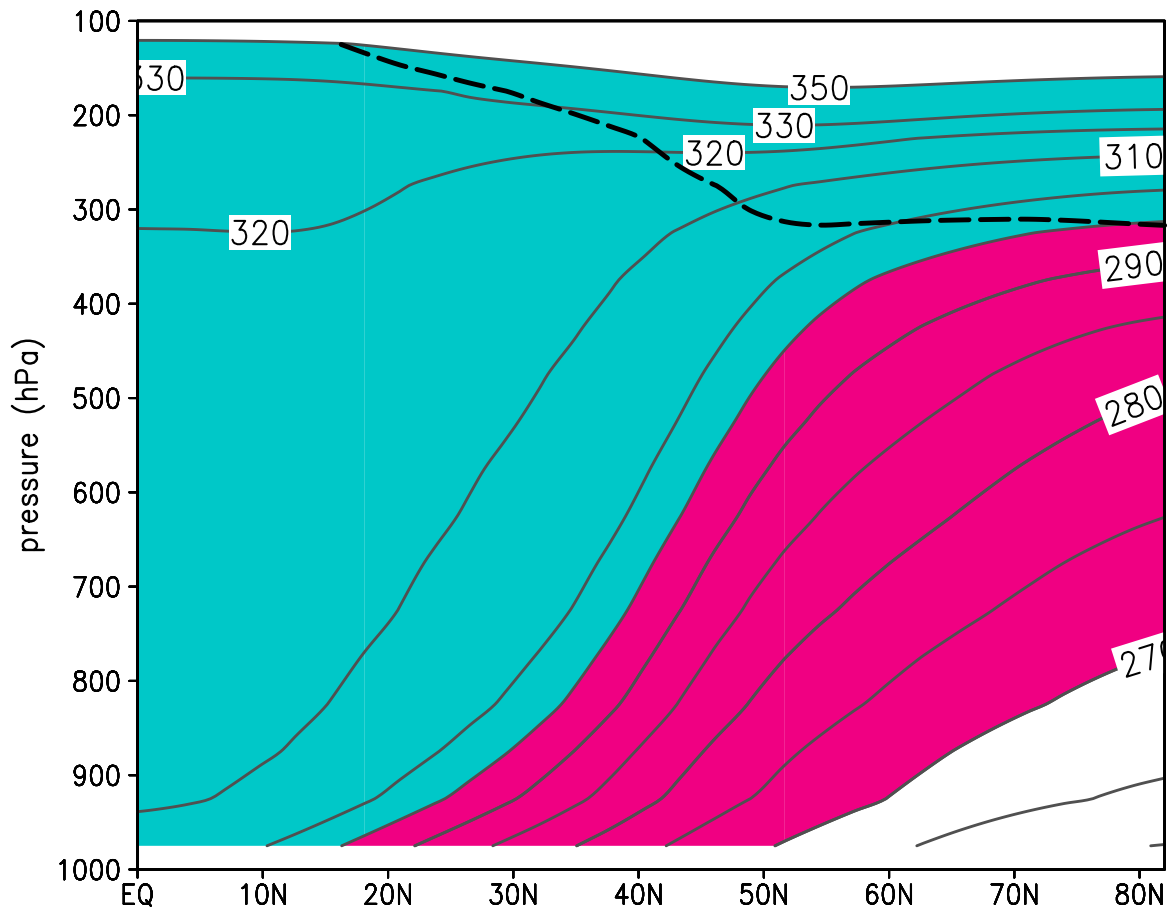
FIG. 4.3. Climatology of zonal-mean potential temperature θ in the 25-year climate run (solid contours, unit: K). The dashed line denotes the climatological 2 PVU surface which represents the dynamical tropopause. Pink and light green shading denote the underworld and the middleworld analyzed here.

that cross the tropopause. In the rest of the paper, the majority of the results are shown on these isentropes or as an average over the underworld or the middleworld.

The spatial pattern of the climatological eddy diffusivity is shown in Fig. 4.4a along with the jet stream (black solid contour). In Fig 4.4a, eddy diffusivity minimize at the jet core near the tropopause, indicating that jet acts as a mixing barrier in the middleworld (e.g. Haynes and Shuckburgh 2000b; Chen and Plumb 2014). The eddy diffusivity linked to RWB bears a very similar spatial pattern to the total (Fig. 4.4b), and in this model about 50% of the eddy mixing
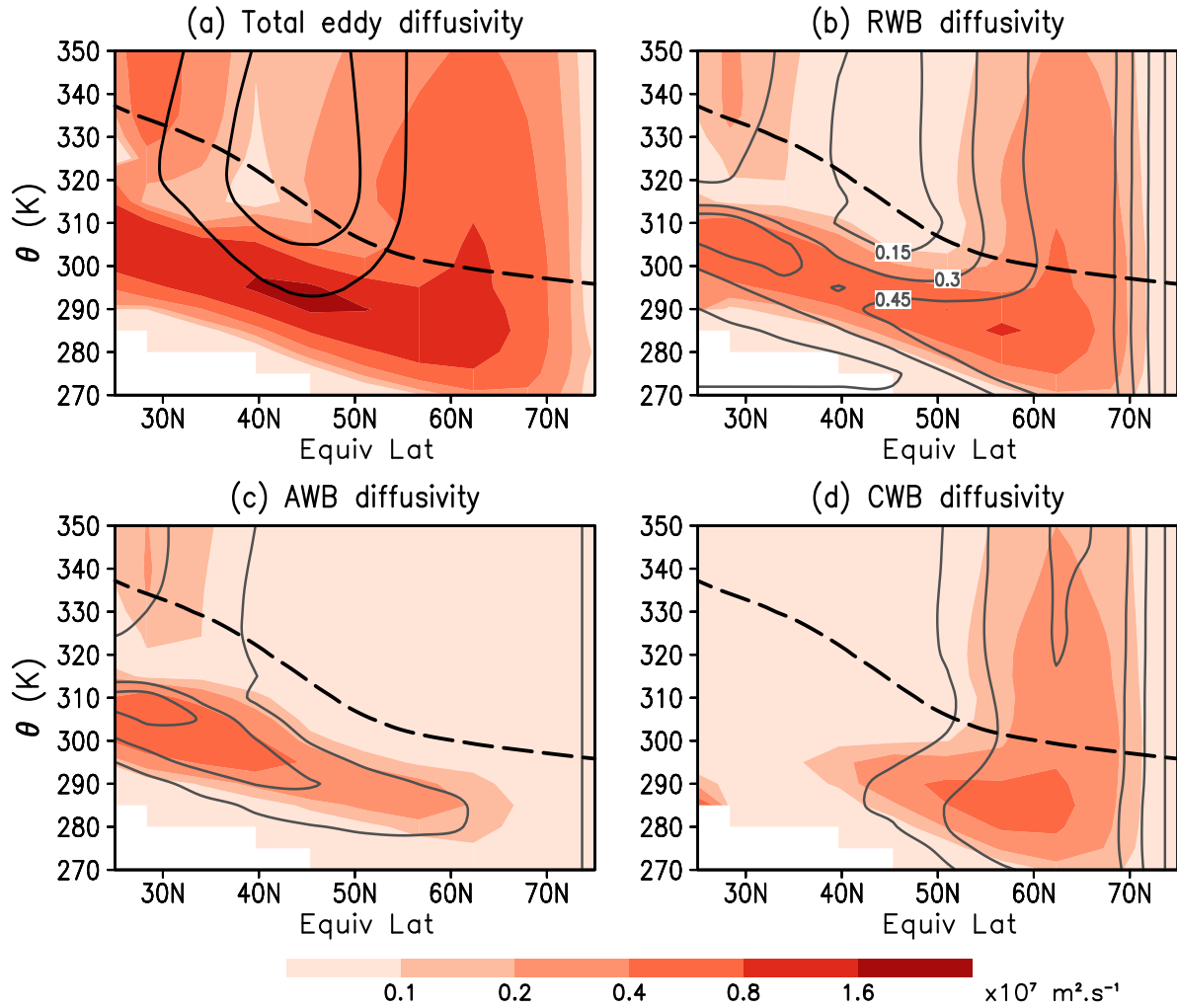
FIG. 4.4. Climatology of eddy diffusivity (shading) for the (a) total, (b) Rossby wave breaking (RWB) contribution, (c) anticyclonic wave breaking (AWB) contribution, and (d) cyclonic wave breaking (CWB) contribution. The two solid black contours in (a) denote the $20 m/s$ and $30 m/s$ contours of the zonal mean zonal wind. Contours in (b)-(d) denote the frequency of occurrence of (b) RWB, (c) AWB, and (d) CWB events, with a contour interval of 0.15. The black dashed line is the 2PVU contour that represents the dynamical tropopause.

is done by large-scale RWB. The RWB frequency of occurrence is plotted in grey in Fig. 4.4b, and agrees well with the magnitude of the eddy diffusivity, with the largest eddy diffusivities overlapping the maxima of RWB frequencies. This agreement confirms the dominant role of RWB in determining midlatitude eddy diffusivity.

The RWB contribution to eddy diffusivity is further divided into AWB contribution and CWB contribution shown in Figs. 4.4c-d (shading), along with their corresponding frequency of occurrence (grey contours). Overall, the contribution of AWB and CWB to eddy diffusivity is very well coupled to their frequency of occurrence. In particular, AWB mainly occurs at lower latitudes equatorward of the jet and so does the eddy diffusivity linked to it (Fig. 4.4c). CWB mainly occurs at higher latitudes poleward of the jet and so does the eddy diffusivity linked to it (Fig. 4.4d). In the middleworld, there is a clear separation between the occurrence of the two types of wave breaking. Therefore, there exists a region with minimum wave breaking frequency that also exhibits a minimum in wave breaking mixing strength (Figs. 4.4b). In the underworld however, there is substantial overlap between the two types of wave breaking (Figs. 4.4c-d) and the total wave breaking frequency stays relatively constant across the entire mid-to-high latitudes (Fig. 4.4b). Correspondingly, the total eddy diffusivity in the underworld does not exhibit a minima near 45°N where zonal wind is strongest. (Figs. 4.4a-b)

A true comparison of the eddy diffusivity between the two types of RWB can be obtained by dividing their climatological mean values by the frequency of RWB occurrence. Through this normalization, we factor out the contribution of frequency and compare the eddy diffusivity per occurrence of AWB/CWB, i.e. their mixing efficiency. Figures. 4.5c-d compare the mixing efficiency of the two types of RWB in the climate simulation, along with their counterparts in the idealized eddy lifecycle simulations shown in Figs. 4.5a-b. In both the lifecycle and climate simulations, CWB (LC2) exhibits a larger diffusivity than AWB (LC1) in the midlatitude underworld. The difference is evident in the majority of midlatitudes from 35°N to 50°N equivalent latitude. Recall that the lifecycle simulations are only made of one event, while the climate simulation is composed of thousands. Thus, we do not expect the results to be identical. However, the lifecycle
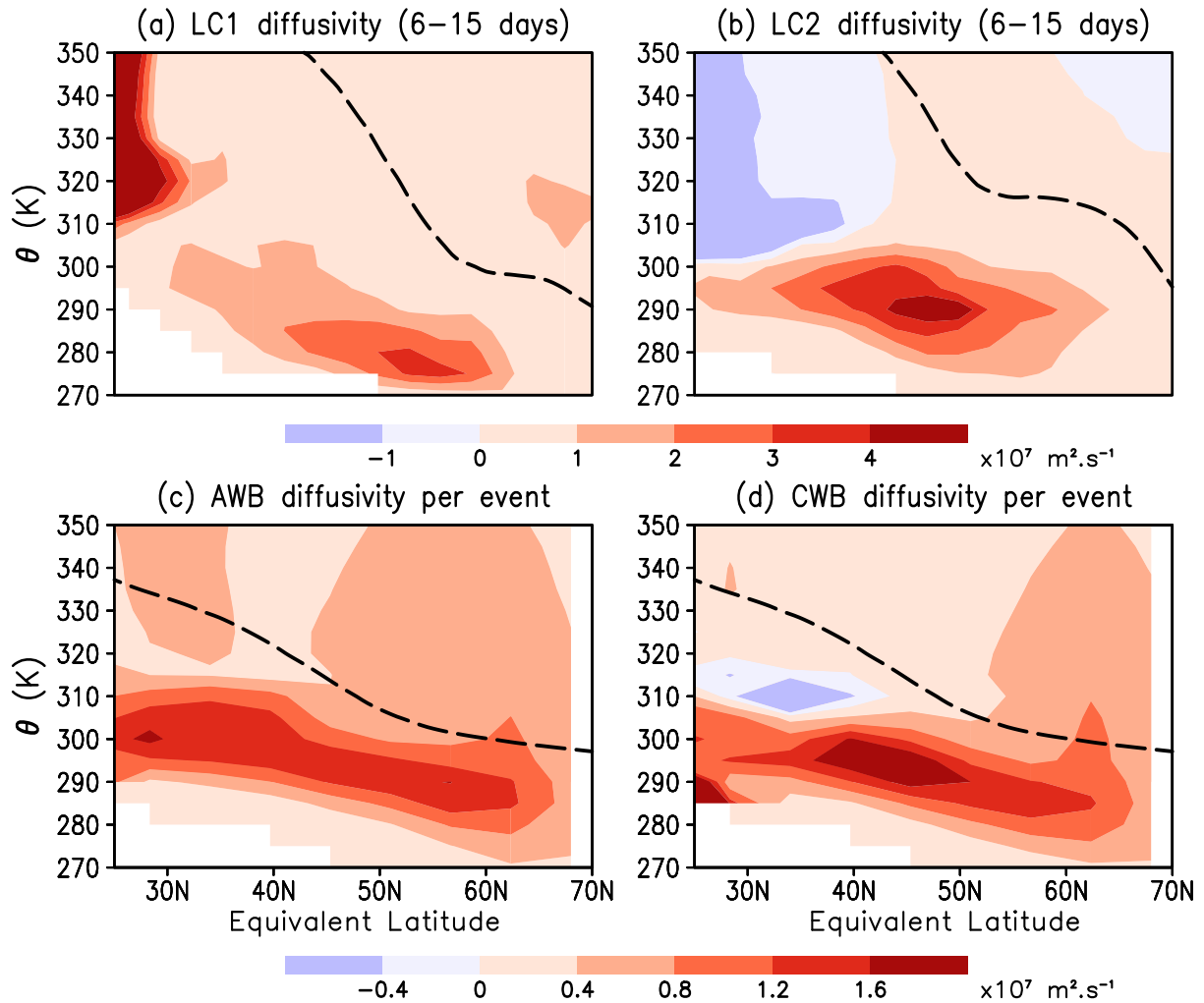
FIG. 4.5. **Upper row**: Eddy diffusivity (shading) in the idealized lifecycle simulations averaged over days 6-15 for (a) LC1, and (b) LC2. **Lower row**: Climatology of eddy diffusivity in the 25-year climate simulation for (c) anticyclonic wave breaking (AWB), and (d) cyclonic wave breaking (CWB), normalized by their respective frequency of occurrence.

simulations bear much resemblance to the climate simulations in Fig. 4.5, indicating the relevance of the idealized lifecycle simulations to more realistic climate settings. Interestingly, they also agree on the existence of negative eddy diffusivity equatorward of the jet stream in the subtropics linked to CWB (Figs. 4.5b and 4.5d). Note such negative diffusivity might be an artifact arising from the hyperdiffusion used in our model. In addition, as discussed in Section 4.3.3, the negative diffusivity in Fig. 4.5d could also arise from the fact that local contribution to the eddy diffusivity

is not guaranteed to be positive. Nevertheless, such up-gradient mixing behavior has been documented in reanalysis data within a similar latitude range (Birner et al. 2013), and more study is needed to tell whether the negative eddy diffusivity linked to CWB in Fig. 7 is an artifact or has physical implications.

4.4.1. SECTION SUMMARY

We quantify the climatology of isentropic mixing linked to the two types of RWB and find,

- In both idealized eddy lifecycle simulations and a long climate simulation, CWB has stronger mixing efficiency (eddy diffusivity per event) than AWB in the underworld.
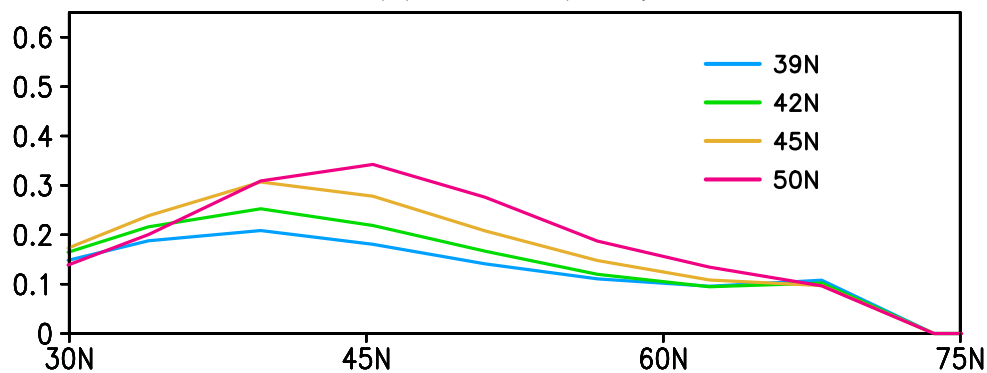- The mixing efficiency in lifecycle simulations bears resemblance to that in the climate simulations.

In the next section, we show how such asymmetry in RWB mixing efficiency translates into a dependence of total isentropic mixing on jet variability.

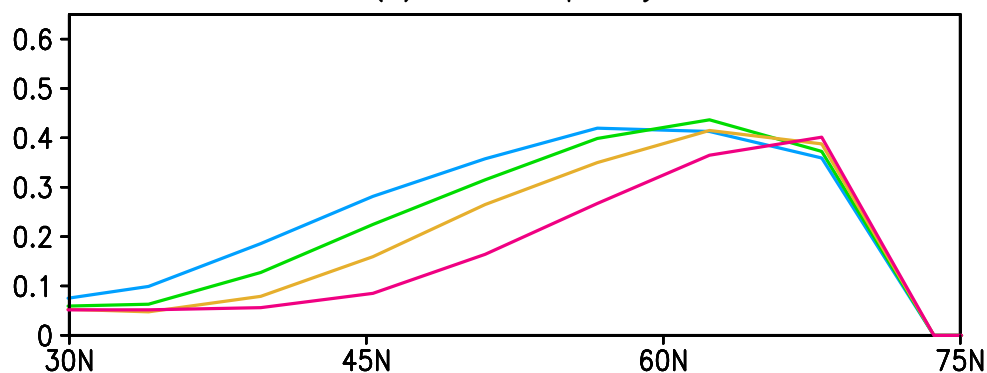### 4.5. DEPENDENCE ON JET STREAM VARIABILITY

The dependence of isentropic mixing strength on the internal variability of the jet, specifically the latitudinal shifts of jet, is explored by compositing the eddy diffusivity with respect to various jet latitudes. We calculate the jet latitude as the latitude of maximum 850hPa zonal-mean zonal wind at 6-hour resolution (e.g. Barnes and Hartmann 2010; Woollings et al. 2010). We group the jet latitudes into four bins centered at $39°N$, $42°N$, $45°N$, and $50°N$, and then composite RWB frequency, eddy diffusivity, and the contribution by RWB according to these jet latitude bins.
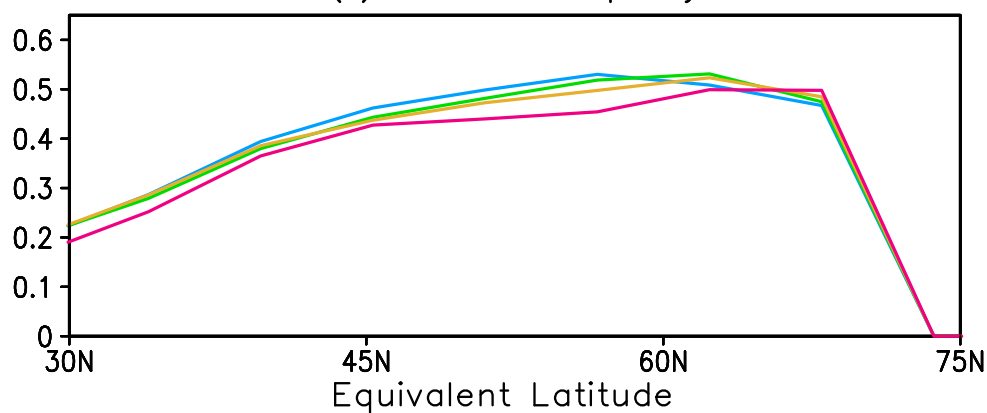
FIG. 4.6. Composite frequency of occurrence of Rossby wave breaking (RWB) with respect to various jet positions for (a) anticyclonic wave breaking (AWB), (b) cyclonic wave breaking (CWB), and (c) the total RWB in the upper underworld (285-295K).

4.5.1. TROPOSPHERIC MIXING

The tropospheric isentropic mixing is investigated by focusing on the upper underworld (285-295K), which constitutes a corridor between the subtropical boundary layer and the polar middle-to-upper troposphere (Fig. 4.3). The average frequency of RWB in this corridor is shown in Fig. 4.6 as a function of equivalent latitude. Consistent with previous studies, AWB occurs more frequently while CWB occurs less frequently as the jet shifts poleward. The extent of the frequency change associated with AWB and CWB are comparable in midlatitudes around $45°N$, indicating a compensation between the two types of RWB. Thus, total RWB frequency decreases only slightly in the midlatitudes as the jet shifts (Fig. 4.6c).

Figures 4.7a and 4.7b show the total eddy diffusivity and the contribution from RWB as a function of equivalent latitude. RWB contributes approximately half of the total and both the total and RWB contribution to eddy diffusivity decrease when the jet is more poleward. This is mainly due to the fact that CWB has a significantly larger eddy diffusivity than AWB (Figs. 4.5c and 4.5d). As a result, the decrease in CWB diffusivity due to decreasing CWB frequency overwhelms the increase in AWB diffusivity due to increasing AWB frequency (Figs. 4.7c-d) and the magnitude of the total decrease is much larger than one would expect from the slight decrease in total RWB frequency (Fig. 4.6c). This effect is most evident in the midlatitudes around $45°N$ equivalent latitude. In this case, the difference between AWB and CWB symmetric mixing efficiency is key to determining the change in total eddy diffusivity linked with changes in the jet position.

4.5.2. STRATOSPHERE-TROPOSPHERE EXCHANGE (STE)

As shown in Fig. 4.2, RWB promotes STE by distorting the tropopause. The vertical distortion of the tropopause by AWB and CWB in the idealized lifecycle simulations is demonstrated in Fig. 4.8 as snapshots on day 6 and day 7 respectively. The two dates are chosen based on the peak stage
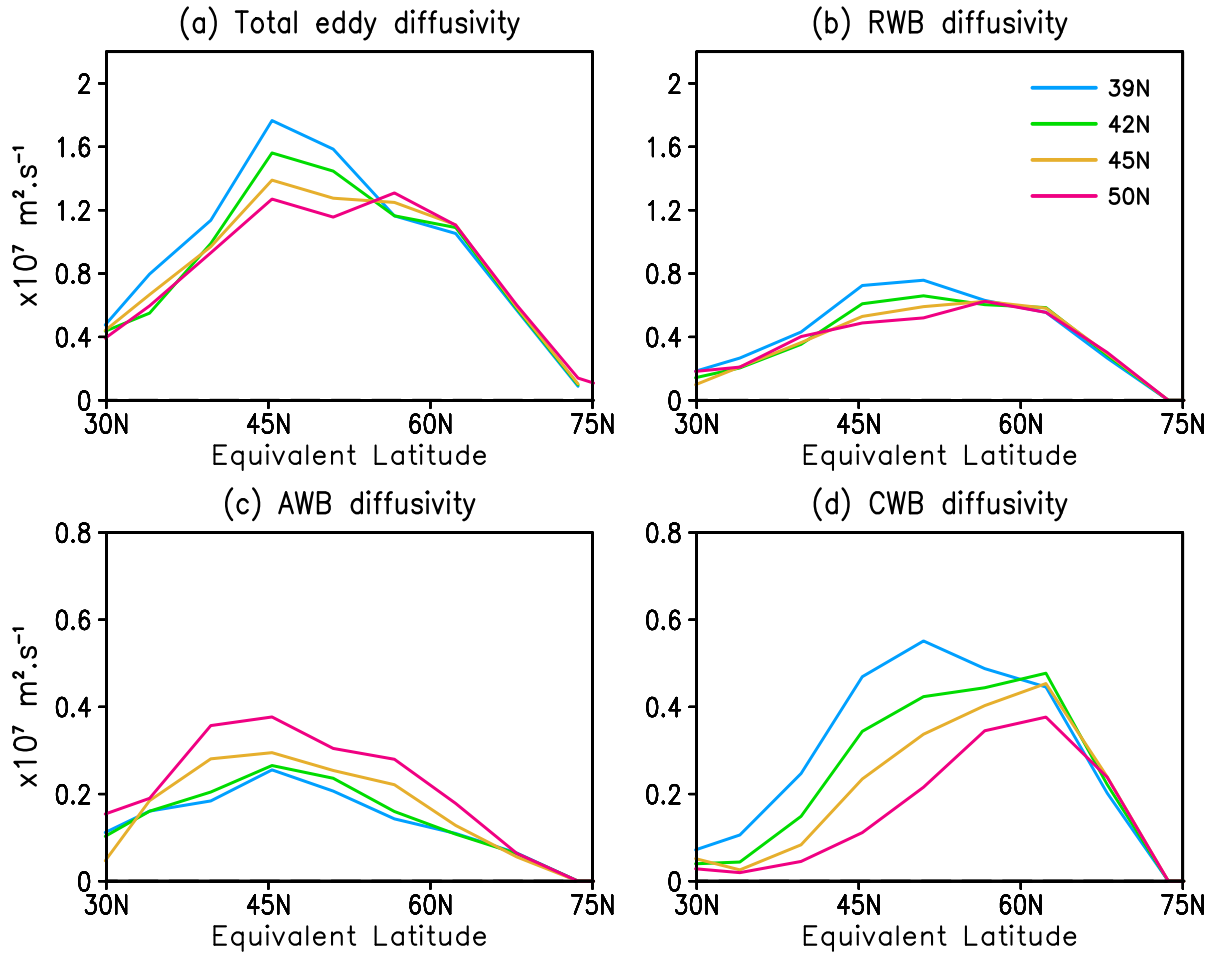
FIG. 4.7. Composite eddy diffusivity (unit: $1 \times 10^7 m^2 s^{-1}$) in the upper underworld with respect to various jet positions for (a) the total, (b) Rossby wave breaking (RWB), (c) anticyclonic wave breaking (AWB), and (d) cyclonic wave breaking (CWB).

of AWB and CWB mixing. As in Fig. 4.2, orange denotes stratospheric air and blue indicates tropospheric air. Both AWB and CWB are associated with an intrusion of stratospheric air that extends to the middle troposphere. Around the intrusion, there exists a mixing area where both stratospheric air is mixed into the troposphere (light blue) and tropospheric air is mixed into the stratosphere (light orange). These streamers are also prevalent in nature (e.g. Shapiro 1980) and the two-way exchange across the tropopause was supported by Lagrangian trajectory studies (e.g.
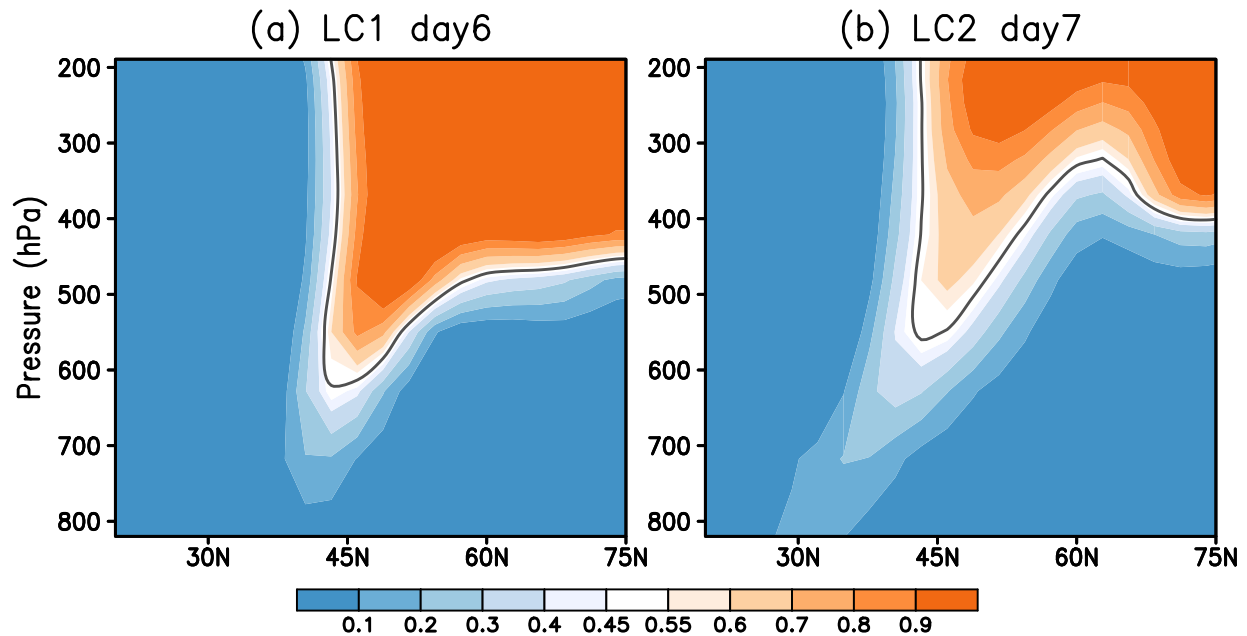
FIG. 4.8. Snapshots of stratospheric tracer concentration S (shading) in the (a) LC1, and (b) LC2 idealized lifecycle simulations on the day of maximum intensity. The grey solid line is $S = 0.5$ contour that represents the tropopause in the simulations.

Sprenger and Wernli 2003; Skerlak et al. 2014). Quantifying the variability of RWB-related two-way STE as shown in Fig. 4.8 is hence of great interest. To serve this purpose, the tropopause is first defined as the equivalent latitude closest to the 2PVU on isentropic surfaces for the four jet latitudes. Then composite eddy diffusivity are extracted along the corresponding tropopauses for the four jet latitudes.

Following the same line of thought as that for tropospheric mixing, we assume the variability of stratosphere-troposphere exchange is also mainly determined by mixing efficiency and frequency of the two types of RWB. We begin by looking at the mixing efficiency. Figure 4.9 shows the eddy diffusivity per RWB occurrence on the tropopause in both idealized eddy lifecycle simulations and climate simulations (red lines), which is essentially a subset of what is shown in Fig. 4.5. In idealized lifecycle simulations, the cross-tropopause diffusivity is much larger in LC2/CWB than LC1/AWB (Figs. 4.9a-b), consistent with a larger mixing area associated with LC2/CWB (Fig.
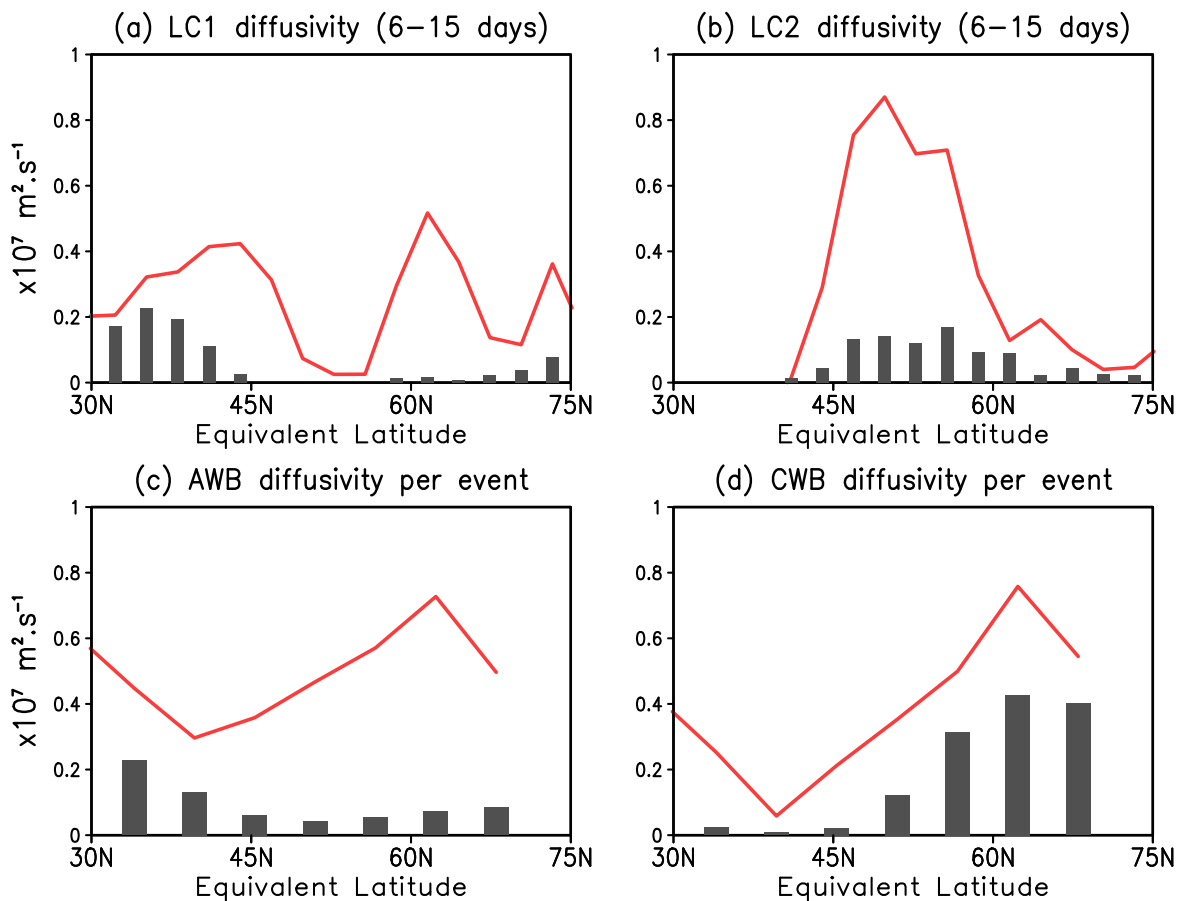
On the tropopause

FIG. 4.9. **Upper row**: Eddy diffusivity on the tropopause (red line) in the idealized lifecycle simulations averaged over days 6-15 for (a) LC1, and (b) LC2. Grey bar denotes averaged frequency of anitcyclonic wave breaking (AWB) in LC1 and cyclonic wave breaking (CWB) in LC2. All the values associated with negative diffusivity are masked out. **Lower row**: Climatology of eddy diffusivity on the tropopause (red line) in the 25-year climate simulation for (c) AWB, and (d) CWB, normalized by their respective frequency of occurrence (grey bar).

4.8). In the climate simulation, the mixing efficiency of CWB at higher latitudes is slightly larger than that of AWB at lower latitudes (Figs. 4.9a-b), but the difference is not as dramatic as in idealized lifecycle simulations (Figs. 4.9c-d).

The composite frequencies of occurrence of the two types of RWB along the tropopause are shown in Fig. 4.10 with respect to jet latitude. As also shown in Fig. 4.9 (grey bars), AWB and CWB occur on two sides of jet and there is little overlap. When the jet shifts poleward,

On the tropopause

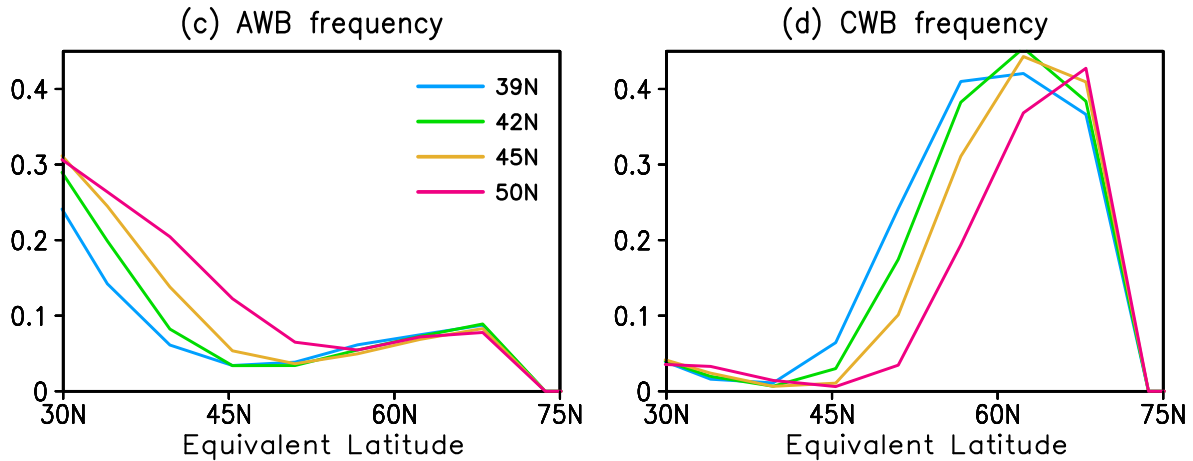(c) AWB frequency   (d) CWB frequency

FIG. 4.10. Composite frequency of occurrence of Rossby wave breaking with respect to various jet positions for (a) anticyclonic wave breaking (AWB), and (b) cyclonic wave breaking (CWB) along the dynamical tropopause.

AWB occurs more frequently while CWB occurs less frequently. Figures 4.11a and 4.11b show the eddy diffusivity across the tropopause and the contribution from RWB. As in the underworld, RWB contributes about half of the total eddy diffusivity and exhibits an almost identical meridional distribution compared to the total. Both the total and RWB eddy diffusivity peaks on the poleward side of jet, due to combined effects of much higher frequency and slightly higher mixing efficiency associated with CWB there. This is also consistent with STE climatology revealed by Lagrangian trajectories (e.g. Sprenger and Wernli 2003; Skerlak et al. 2014). In terms of the variability associated with the jet shifting, a substantial portion of the total can be explained by the RWB contribution (compare Figs. 4.11a and 4.11b), which in turn, is explained by the AWB and CWB frequency changes on the both sides of the jet (compare Figs. 4.11c-d and Figs. 4.10a-b). On the poleward side of the jet, the eddy diffusivity across the tropopause weakens as the jet shifts poleward as a result of decreased CWB frequency. On the equatorward side of the jet, the

eddy diffusivity increases as a result of increased AWB frequency. While AWB and CWB do exhibit different mixing efficiencies, these changes are predominantly explained by changes in RWB frequency itself.

4.5.3. SECTION SUMMARY

As the jet shifts poleward,

- upper underworld eddy diffusivity decreases due to the difference in AWB and CWB mixing efficiencies.

- across the tropopause, eddy diffusivity decreases poleward of the jet due to decreased CWB frequency and increases equatorward of the jet due to increased AWB frequency.

4.6. CONCLUSIONS

A modified-Lagrangian-mean framework to quantify isentropic mixing is applied to Rossby wave breaking (RWB) in both free eddy lifecycle simulations and a forced climate simulation. The focus of this study is on the difference between the two flavors of RWB – anticyclonic wave breaking (AWB) and cyclonic wave breaking (CWB). It is found that in both sets of simulations and throughout different regions of the atmosphere, CWB has either comparable or stronger isentropic mixing efficiency than AWB. This result has implications for the influence of climate variability on isentropic mixing. In the upper underworld, since CWB occurs less frequently and AWB occurs more frequently as the jet shifts poleward, mixing differences translate into a decrease in total mixing strength (eddy diffusivity). Across the tropopause, AWB increases on the equatorward flank of the jet, leading to increased eddy diffusivity there. CWB decreased on the equatorward flank of the jet, leading to decreased eddy diffusivity there.
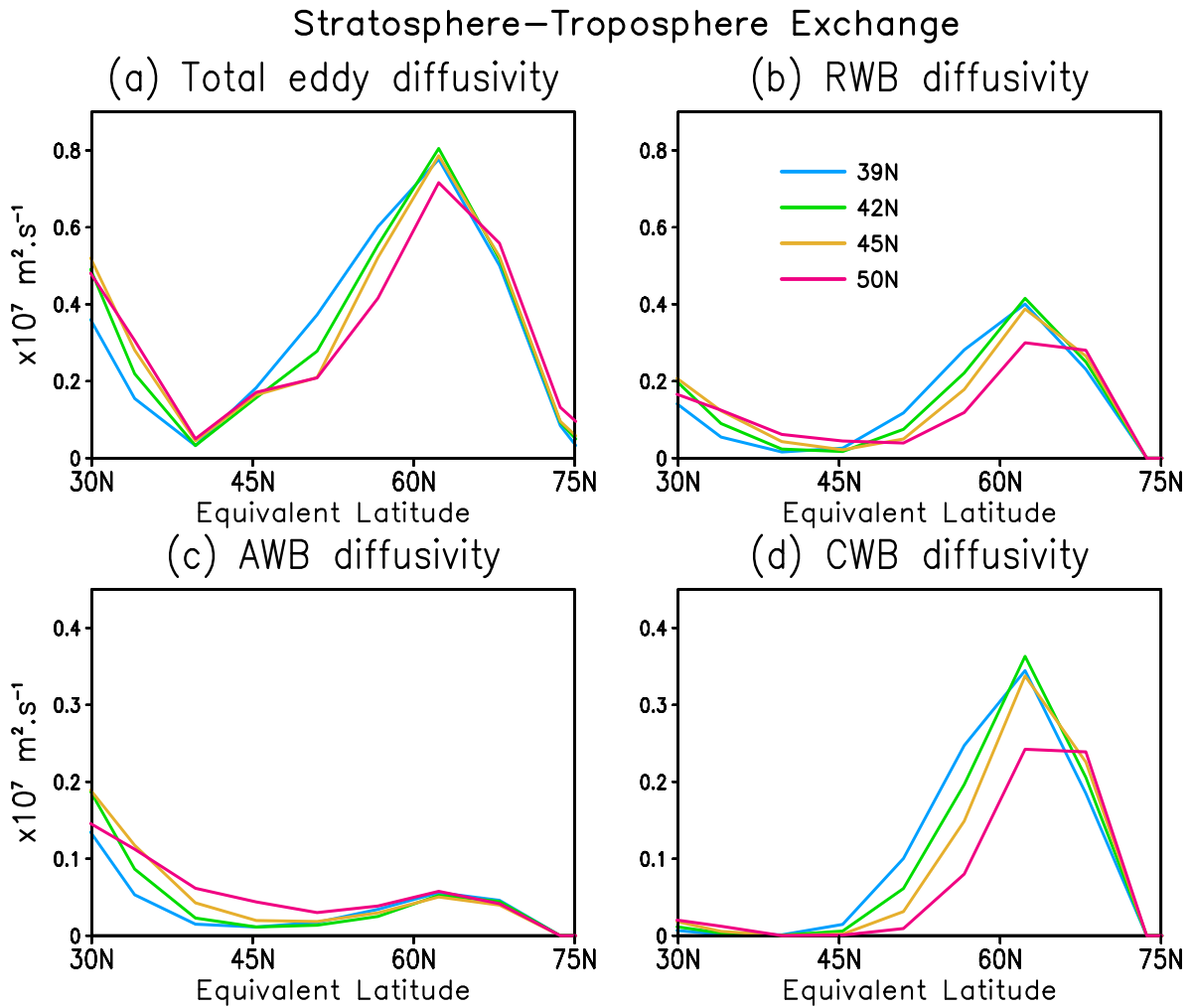
FIG. 4.11. Composite eddy diffusivity (unit: $1 \times 10^7 m^2 s^{-1}$) along the dynamical tropopause with respect to various jet positions for (a) the total, (b) Rossby wave breaking (RWB), (c) anticyclonic wave breaking (AWB), and (d) cyclonic wave breaking (CWB).

Although the simulations in this study are highly idealized, we argue that the conclusions obtained are applicable to the real atmosphere. Abalos et al. (2016) used ERA-Interim to show that in winter the effective diffusivity across the tropopause decreases in the mid-to-high latitudes during a positive Northern Annular Mode when the jet is more poleward, and increases during positive ENSO when the jet is more equatorward. These results are consistent with the modulation by the jet stream of the two types of RWB. Although our study does not directly address the jet

shift in response to external forcing (e.g. anthropogenic climate change), we expect similar results to what is found here due to the same relationship between RWB and the jet stream in climate change simulations (e.g. Barnes and Polvani 2013). In fact, Orbe et al. (2015) demonstrated that isentropic mixing from the midlatitude boundary layer to the Arctic increases over the northeast Pacific with climate change in a state-of-the-art GCM where the jet stream shifts equatorward. This is consistent with our argument that an equatorward jet shift increases the frequency of the more efficient cyclonic wave breaking, and thus, increases the mid-latitude mixing strength.

In the real atmosphere, certain constituents whose spatial distributions are impacted by climate change, also contribute to the climate forcing. Examples include carbon dioxide, ozone, various species of aerosols and water vapor. Thus understanding the passive response of atmospheric constituents to climate change is an important step towards understanding the entire feedback loop. This study provides a mechanistic explanation for how the isentropic mixing of constituents may respond to future jet shifts.

CHAPTER 5

STRATOSPHERE-TROPOSPHERE EXCHANGE OF OZONE IN REANALYSIS DATA

5.1. MOTIVATION AND OVERVIEW

The stratosphere-troposphere exchange of ozone is important for both impacting climate through radiative forcing (e.g. Forster et al. 1997) and influencing air quality (e.g. Lin et al. 2012). Therefore, the dynamical processes driving its variability are of great interest. When long-term trends or hemispheric scales are of interest, the processes in the stratosphere such as Brewer-Dobson circulation has been shown to explain the ozone variability in the mid-to-high-latitude upper troposphere (e.g. Hegglin and Shepherd 2009; Hess et al. 2015). They attribute global scale ozone changes to the changes in the slow downwelling in the mid-to-high latitudes. When short-term, extreme local ozone variability is of interest, stratospheric intrusions deep into the troposphere are known to be responsible for high ozone concentrations in the mid-to-upper troposphere (e.g. Shapiro 1980), suggesting an important role for tropospheric Rossby wave breaking (RWB) (e.g. Appenzeller et al. 1996a; Waugh and Polvani 2000). However, for temporal and spatial scales in between these two ends, the mechanisms responsible for the variability of ozone is poorly understood. For example, interannual variability of upper tropospheric ozone over the North Pacific and North America is strongly influenced by the El-Niño Southern Oscillation (ENSO) (e.g. Langford et al. 1998; Lin et al. 2015), but no consensus has been reached regarding the processes that dominate this variability (e.g. Langford 1999; Neu et al. 2014; Albers et al. 2017). The goal of this chapter is to shorten this gap of understanding.

Starting from the basis of the previous chapters, our hypothesis is that RWB events contribute significantly to the regional intraseasonal and interannual variability of upper tropospheric ozone.

To test this, we first investigate the composite behavior of individual RWB events in terms of driving stratospheric ozone intrusions. Then we composite RWB frequency and the associated ozone anomalies to study month-to-month variability in ozone driven by the North Pacific jet shifting and interannual variability influenced by ENSO. Only springtime (MAM) is considered in the composites, as it is when stratospheric to troposphere transport is the strongest in the Northern Hemisphere (e.g. Appenzeller et al. 1996b; Yang et al. 2016). The chapter is organized as follows. Section 5.2 describes the data and methods used. Section 5.3 addresses individual RWB behavior and Section 5.4 addresses the ozone variability contributed by RWB. A brief summary is given in Section 5.5.

5.2. DATA AND METHOD

We use the Modern-Era Retrospective analysis for Research and Applications, Version 2 (MERRA2) data (Gelaro et al. 2017) for ozone (O_3), zonal wind (u), meridional wind (v), and temperature (T) on 17 pressure levels. Following the methods described in Chapter 2, potential vorticity (PV) on isentropes is calculated from u, v, and T, and Rossby wave breaking (RWB) is identified using the PV contours and classified into anticyclonic wave breaking (AWB) and cyclonic wave breaking (CWB) according to the direction of overturning. For two consecutive time steps, two RWB of the same type are grouped into the same event if the distance between the two centroids is less than $3r_c$. r_c is a measure of RWB spatial scale and we refer readers to Chapter 2 for its definition.

The quality of ozone data in MERRA2 was evaluated in Wargan et al. (2017) by comparison to independent satellite and ozone sonde data. It was found that MERRA2 realistically represent the near-tropopause ozone variability, lending support to the use of MERRA2 ozone in this study. In addition, Albers et al. (2017) analyze the MERRA2 ozone along with the ERA-Interim ozone

and concluded that reanalysis ozone is adequate for studying stratosphere-troposphere exchange of ozone.

To estimate the contribution of RWB to tropospheric ozone load, we calculate two sets of variables. The first set is $O3_{RWB} = O3_{AWB} + O3_{CWB}$ on isentropes. $O3_{RWB}$ has actual ozone concentration within the equatorward lobes of RWB but zero elsewhere. Note that $O3_{RWB}$ quantifies the amount of ozone within the intrusion plumes which does not necessarily equate to the amount of ozone irreversibly mixed into the troposphere. Nevertheless, the comparison between $O3_{RWB}$ and actual upper tropospheric ozone shows that it is a reasonable approximation (later in the chapter). The second set is $RWB_{freq} = AWB_{freq} + CWB_{freq}$. RWB_{freq} has a value of 1 within the equatorward lobes of RWB but zero elsewhere. RWB_{freq} quantifies the frequency of occurrence of RWB on isentropes.

To study the intraseasonal variability of upper tropospheric ozone influenced by the jet, monthly North Pacific jet latitude is calculated using MERRA2 zonal wind at 850hPa. The zonal wind is first averaged over the longitude range from 140°E to 130°W. Then the jet latitude is determined as the latitude of maximum zonal mean zonal wind. We only search for jet latitudes equatorward of 65°N.

To investigate the interannual variability of upper tropospheric ozone influenced by ENSO, we use the monthly NOAA Oceanic Niño Index (ONI). ONI is calculated by averaging sea surface temperature (SST) anomalies over the Niño 3.4 region (5°S-5°N, 170°W-120°W).

The impact of the jet and ENSO is evaluated by compositing monthly anomaly data with respect to high/low jet latitudes and warm/cold ENSO phases. The monthly anomaly is obtained by subtracting the monthly seasonal cycle, which is calculated as the calendar mean of each month

over 1982-2016. To focus on springtime stratospheric ozone intrusions, we only consider March-April-May (MAM) in this study.

5.3. STRATOSPHERIC INTRUSIONS DRIVEN BY THE TWO TYPES OF ROSSBY WAVE BREAKING

A stratospheric intrusion of ozone driven by anticyclonic wave breaking (AWB) is shown in Fig. 5.1. The intrusion occurs near the equatorward lobe of the breaking wave from 30°N to 40°N (Figs. 5.1a). Viewed in a cross section, the intrusion of high ozone air (greater than 135 ppb) reaches 600 hPa in the mid-troposphere approximately following isentropic surfaces (Figs. 5.1b). Intrusion events like this have been shown to account for extreme ozone concentration in the troposphere (e.g. Shapiro 1980; Appenzeller et al. 1996a). Besides their impact on extreme events, we aim to demonstrate that they are also important for intraseasonal and interannual variability of tropospheric ozone load and that much can be learned by studying the average behavior of individual wave breaking events that drive these intrusions in reanalysis data.

To shed light on RWB driven stratospheric ozone intrusions, centered composites of ozone concentration with respect to AWB and CWB are shown in Fig. 5.2a-b respectively. The upper panels show the composite ozone concentration in ppb on 300h Pa and the lower panels show the corresponding cross sections across the equatorward intrusion lobes of RWB. On 300 hPa, CWB contains substantially more ozone in its equatorward lobe than AWB. The cross sections show an additional asymmetry between AWB and CWB. In particular, CWB features narrower and deeper intrusions than AWB south of the 0° relative latitude (Figs. 5.2c-d). These features combined suggest stronger ozone flux associated with CWB compared to AWB, consistent with the idealized results shown in Chapter 4.
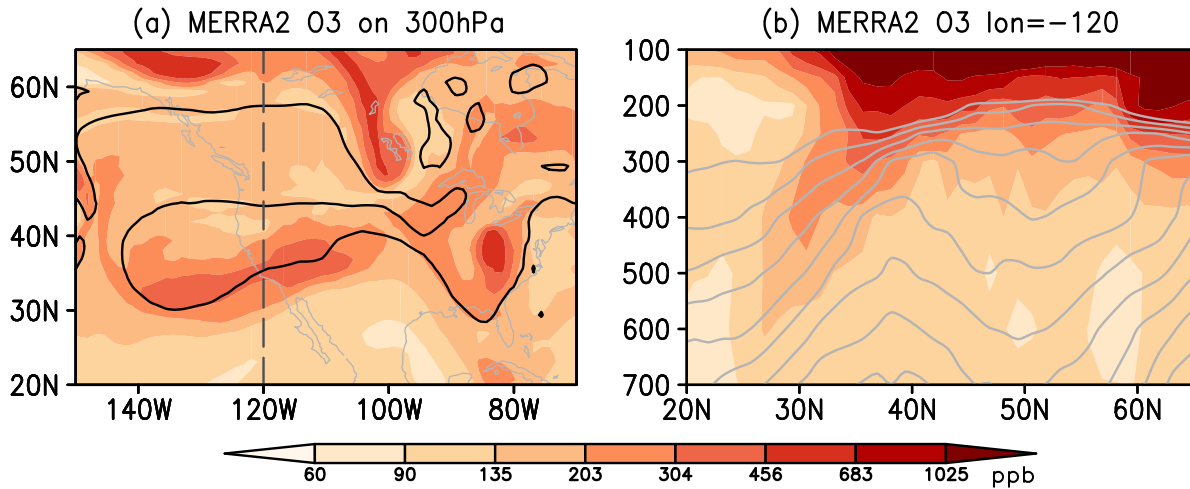
FIG. 5.1. Snapshots of ozone concentration (shading) during a Rossby wave break-
ing event on May 4, 1998. (a) Ozone concentration on 300 hPa. Grey contours
denote potential temperature on 2 PVU surface. (b) Cross section of ozone concen-
tration along 120°W. Grey contours denote potential temperature at an interval of
5K, with the maxima being 340K.

To test the robustness of this asymmetry in reanalysis, a bootstrapping test is conducted. We

first assume AWB is no different from CWB (our null hypothesis). Accordingly, as we composite

for CWB events, we randomly substitute CWB with arbitrary AWB. We repeat this procedure

1000 times and rank ozone anomalies at each grid. Finally, the actual CWB composite value is

compared with the highest 1 percentile value from random sampling to assess the significance of

the difference. The significant high ozone values in CWB are denoted by cyan hatches in Fig. 5.2d.

The main intrusion during CWB from -15° to 0° relative latitude has significantly higher ozone than

that associated with AWB/CWB combined, confirming the robustness of this asymmetry between

the two types of wave breaking.

The average evolution of AWB/CWB and the corresponding ozone intrusions are shown by

lead-lag composites in Figs. 5.3 and 5.4 respectively. The left columns show the ozone concen-

tration on 300 hPa from 2 days before the mature phase of breaking to the first day of the mature

breaking phase. The right columns show corresponding cross sections of ozone anomalies across
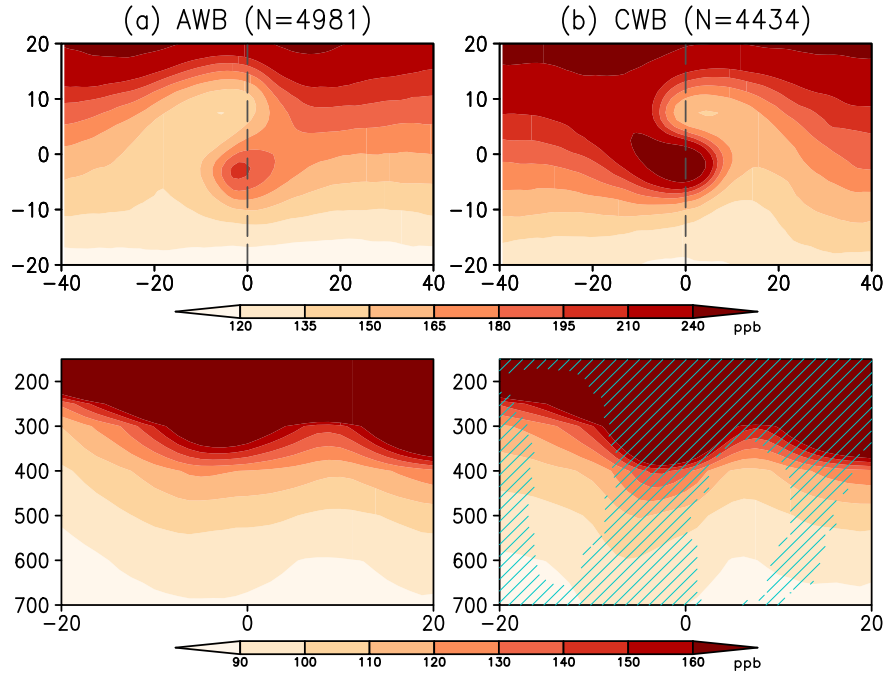
FIG. 5.2. Composite ozone concentrations for anticyclonic wave breaking (AWB) in the left column and cyclonic wave breaking (CWB) in the right column. The fields are moved horizontally so that the centers for each type of wave breaking overlap. The longitude and latitude shown on the axes are relative to the wave breaking centers. **Upper row**: Composite ozone on 300 hPa. **Lower row:** Cross section of composite ozone across the grey dashed line shown in the upper panels. The numbers in the titles denote the sample size of wave breaking events that goes into each composite. The hatches denote the regions where composite ozone concentrations for CWB are significantly higher than that for AWB/CWB combined at 0.01 level.

relative longitudes denoted by grey dashed lines in the left columns. The ozone anomaly is obtained by subtracting the ozone concentration 3 days before the mature phase at each grid. For AWB in Fig. 5.3, the composite ozone field in the left column depicts the amplification and subsequent breaking of the Rossby wave, featured by anticyclonic overturning of the wave lobes. The poleward lobe contains below normal ozone while the equatorward lobe contains above normal ozone. The right column shows that the equatorward moving lobe descends at the same time, featuring downward propagation of positive ozone anomalies equatorward of the RWB centroid.
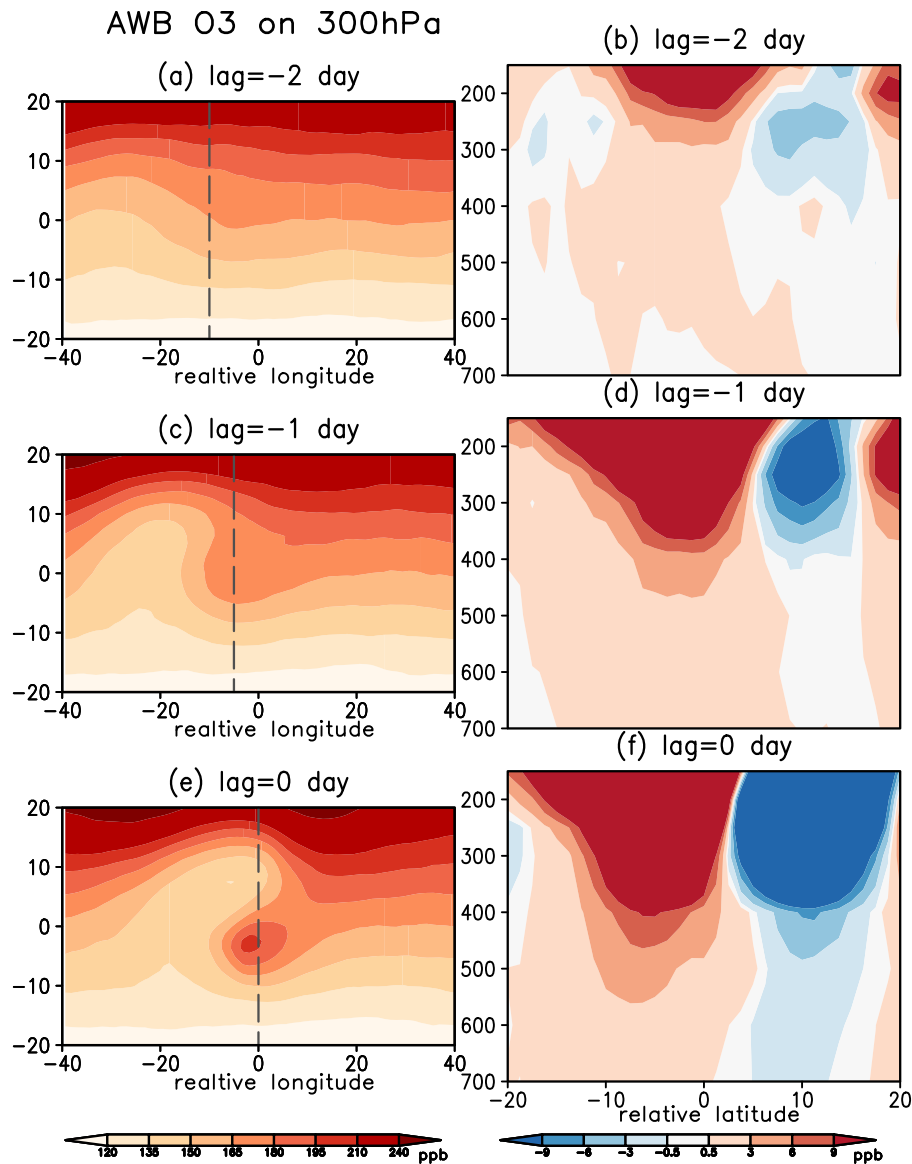
Fig. 5.3. **Left Column:** Lead-lag composite ozone concentration on 300hPa with respect to anticyclonic wave breaking (AWB). The fields are moved horizontally so that the centers for each type of wave breaking overlap. The longitude and latitude shown on the axes are relative to the wave breaking centers. **Right Column:** The corresponding cross sections across the longitudes shown as grey dashed lines in the left column.

For CWB in Fig. 5.4, the left column also shows the progression of horizontal overturning but in cyclonic fashion. The right column demonstrates a more well defined downward intrusion of ozone anomalies than for AWB. Correspondingly, both the strength and depth of the intrusion is

FIG. 5.4. As in Fig. 5.3, but for cyclonic wave breaking (CWB).

significantly larger for CWB than for AWB. Note that the ozone anomalies appear narrower during

CWB than during AWB events, a feature also alluded to in Fig. 5.2.

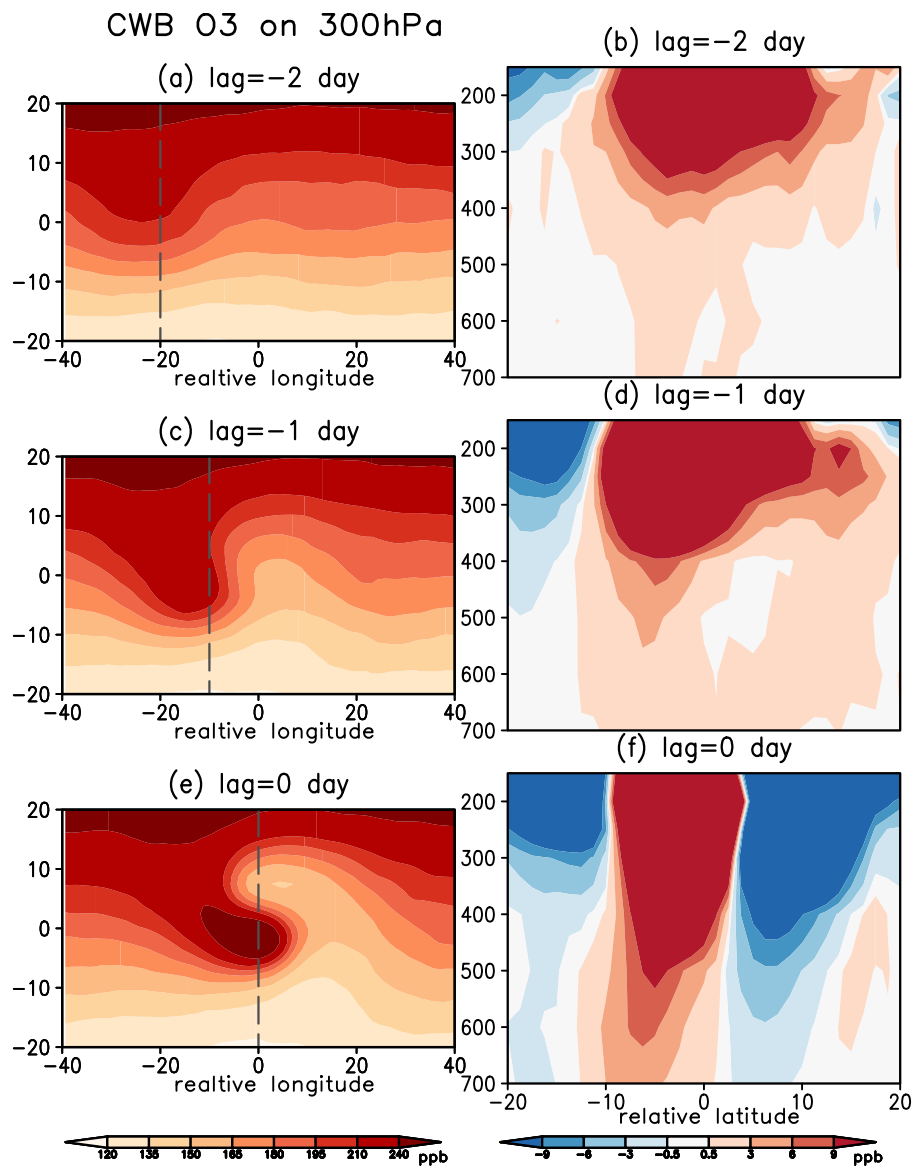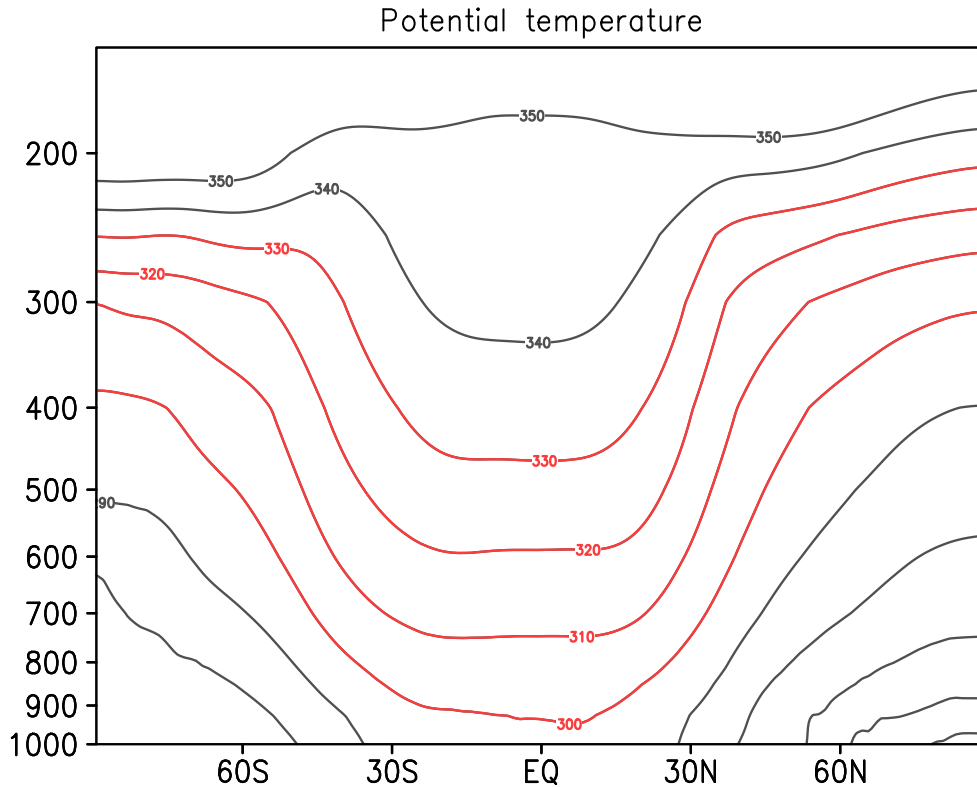FIG. 5.5. Climatological zonal mean potential temperature in MAM. The isentropes used for composites are colored red.

5.4. CONTRIBUTION OF RWB DRIVEN OZONE INTRUSIONS TO UPPER TROPO-SPHERIC OZONE VARIABILITY

As shown by Fig. 5.1 and previous studies, stratosphere-troposphere exchange in the mid-latitudes mainly occurs along isentropic surfaces (e.g. Shapiro 1980; Thorncroft et al. 1993; Madonna et al. 2014). In this section, the ozone intrusions and the RWB events that drive them are considered on isentropes ranging from 300K-330K. These isentropes are chosen because they are important for connecting the lower stratosphere and the mid-to-upper troposphere (Fig. 5.5), and medium to deep intrusions mostly occur along these isentropes (e.g. Škerlak et al. 2015). The anomalies of RWB frequency and RWB driven ozone intrusions are then averaged over isentropes 300-330K and composited with respect to the North Pacific jet latitude and ENSO phases.
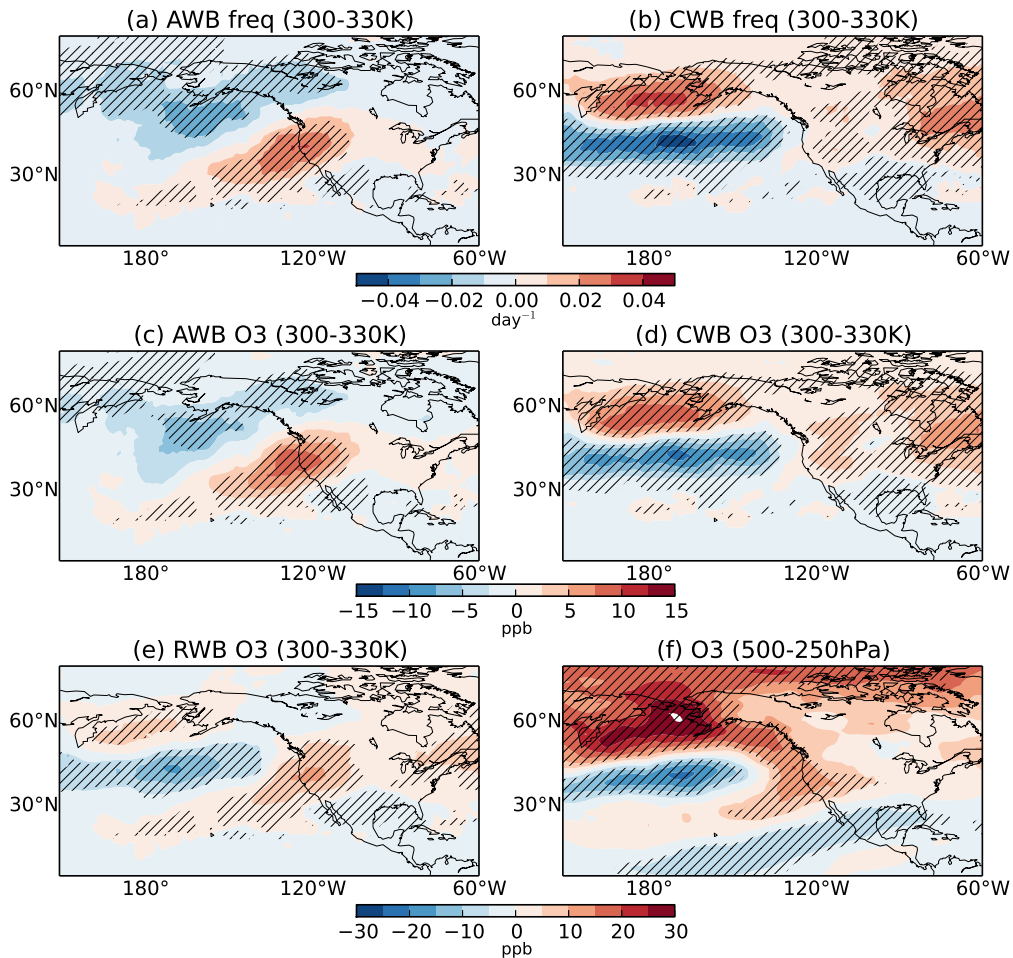
FIG. 5.6. Difference in composite monthly variables between high and low North Pacific jet latitudes. (a)(b) Anticyclonic wave breaking (AWB) and cyclonic wave breaking (CWB) frequency anomalies. (c)(d) Ozone linked to AWB and CWB ($O3_{AWB}$ and $O3_{CWB}$). (e) $O3_{RWB} = O3_{AWB} + O3_{CWB}$. (f) Ozone averaged over 500-250hPa.

Fig. 5.6 shows composite monthly variables for high North Pacific jet latitude minus those for low jet latitude in spring (MAM), with hatches denoting anomalies significant at 0.05 level by a bootstrapping test. The high and low jet latitude are defined as one standard deviation above and below climatological jet latitude in MAM. The first row shows the frequency anomalies of AWB and CWB (AWB_{freq} and CWB_{freq}) for the poleward shifted North Pacific jet. AWB occurs more frequently in a region extending from U.S. West to Hawaii, and less frequently to the south of the Aleutian Islands. CWB frequency exhibits a dipole anomaly pattern over the North

Pacific, showing a poleward shift as the jet shifts poleward. Over most of the U.S. and southern Canada, CWB occurs more frequently. The second row of Fig. 5.6 shows the contribution to ozone concentrations by the two types of RWB ($O3_{AWB}$ and $O3_{CWB}$). Both $O3_{AWB}$ and $O3_{CWB}$ anomalies resemble their respective frequency anomaly patterns. In the third row, Fig. 5.6e shows the total RWB driven ozone anomalies ($O3_{RWB}$). The similarity between Fig. 5.6e and Fig. 5.6d demonstrates the dominance of CWB over AWB in $O3_{RWB}$ anomalies, due to a combined effect of both larger frequency anomalies (Figs. 5.6a-b) and higher efficiency per event (Figs. 5.3 and 5.4). The composite of the total upper tropospheric ozone difference is also shown in Fig. 5.6f, bearing much resemblance to $O3_{RWB}$ anomaly (Fig. 5.6e), and hence, the $O3_{CWB}$ anomaly (Fig. 5.6d). All of these panels combined show that CWB explains the majority of upper tropospheric ozone variability associated with North Pacific jet wobbling.

Given the power of RWB in explaining the month-to-month connection between the North Pacific jet and ozone variability, it is justified to also study the connection between ENSO and ozone variability on interannual time scales and see how much RWB statistics can explain this connection. Fig. 5.7 shows composite MAM-mean anomalies for El-Niño subtracting those for La-Niña years. El-Niño and La-Niña years are defined as years with MAM average ONI one standard deviation above and below climatology respectively. During ENSO, CWB has larger frequency anomalies than AWB (Figs. 5.7a-b), as was also the case for the North Pacific jet wobbling. Correspondingly, the $O3_{CWB}$ anomaly also dominates over the $O3_{AWB}$ anomaly (Fig. 5.7c-d) and largely determines the $O3_{RWB}$ anomaly (Fig. 5.7e), which resembles the actual upper tropospheric ozone anomaly related to ENSO (Fig. 5.7f). In particular, during El-Niño the significant positive anomaly spanning from the North Pacific to the southern U.S. coincides with the $O3_{RWB}$ anomaly
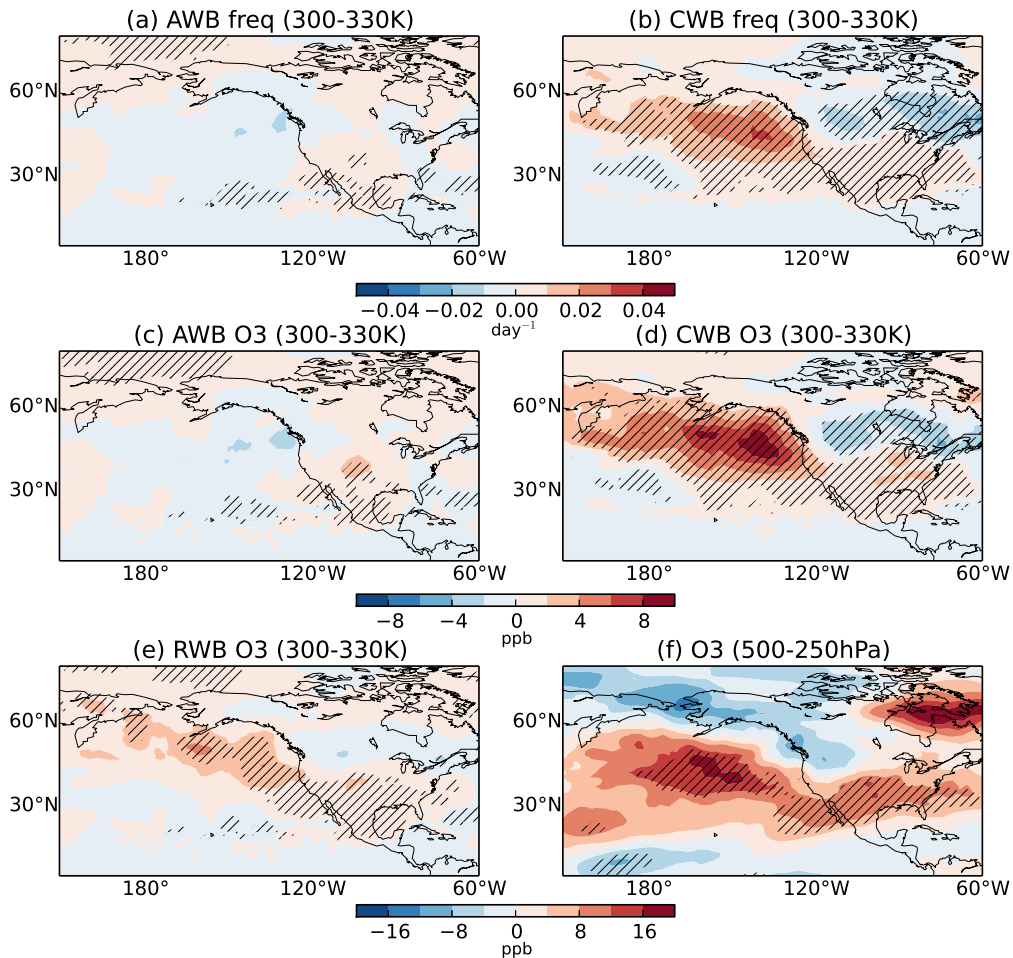
FIG. 5.7. Difference in composite monthly variables between warm and cold phases of ENSO. (a)(b) Anticyclonic wave breaking (AWB) and cyclonic wave breaking (CWB) frequency anomalies. (c)(d) Ozone linked to AWB and CWB ($O3_{AWB}$ and $O3_{CWB}$). (e) $O3_{RWB} = O3_{AWB} + O3_{CWB}$. (f) Ozone averaged over 500-250hPa.

(compare Fig. 5.7e and f), which is due to increased CWB frequency over the region (Fig. 5.7d) as a response to ENSO (e.g. Liu et al. 2014)

5.5. SUMMARY

Using the MERRA2 reanalysis ozone concentration data, we investigate the average spatial pattern and temporal evolution of ozone during AWB and CWB events. It is found that compared to AWB, CWB features stronger ozone anomalies within the equatorward lobe, and deeper, narrower

intrusions into the troposphere. This is consistent with stronger mixing strength associated with CWB in idealized lifecycle and climate simulations (Chapter 4).

On both intraseasonal and interannual time scales over the North Pacific and North America, the upper tropospheric ozone variability can be largely explained by RWB related ozone intrusions, which are in turn, dominated by CWB variability. Specifically, for month-to-month wobbling of the North Pacific jet, a poleward jet is linked to a poleward shift of CWB over the North Pacific and increased CWB over the U.S. and Canada. The upper tropospheric ozone increases where CWB frequency increases and decreases where CWB frequency decreases in mid-to-high latitudes. For interannual ENSO variability, CWB increases over the North Pacific and the southern U.S. and so does the upper tropospheric ozone.

Based on these results, we argue that in the real atmosphere, the accumulated effects of RWB variability can influence ozone variability on time scales much longer than a synoptic lifecycle and over a region much larger than synoptic scale.

CHAPTER 6

CONCLUSIONS AND OUTLOOK

Rossby wave breaking's role in transporting and mixing constituents on synoptic time scales has been documented in observations (e.g. Waugh 2005; Homeyer et al. 2011) and in idealized lifecycle simulations (Stone et al. 1999; Polvani and Esler 2007). The contribution of this thesis is demonstrating the extent to which Rossby wave breaking contributes to the climate variability of transport and mixing, both horizontally, across a range of latitudes, and vertically, across the tropopause. In particular, by leveraging the robust relationship between jet streams and the frequency of the two types of wave breaking – anticyclonic wave breaking (AWB) and cyclonic wave breaking (CWB) – our work improves understanding of the variability of atmospheric constituents such as moisture and ozone influenced by climate variability (e.g. ENSO, NAO and jet shifting).

Although this thesis does not address climate change explicitly, we expect our results to improve understanding of the influence of climate change on RWB related transport and mixing as well, due to the similar relationship between AWB/CWB and jet streams under climate change (e.g. Barnes and Polvani 2013). Specifically, as the jet shifts poleward with climate change, AWB occurs more frequently at lower latitudes and CWB occurs less frequently at higher latitudes. Based on the results from the previous sections, the strength of transport/mixing is expected to increase where RWB occurs more frequently and decrease where RWB occurs less frequently. More research is warranted to test this.

In addition, caveats should be raised regarding several aspects of this work. Firstly, in Chapter 5 the ozone anomalies in MERRA2 are not guaranteed to purely result from stratosphere-troposphere exchange. Chemistry no doubt plays a role in observational upper tropospheric ozone and here we

assume it is smaller than the role of mass exchange across the tropopause. A numerical simulation with tagged stratospheric ozone in a chemical transport model would be a good next step to quantify stratosphere-troposphere exchange more rigorously. Secondly, when assessing the contribution of RWB to global stratosphere-troposphere exchange in the idealized GCM (Chapter 4), we neglect the Brewer-Dobson circulation as the model setup does not represent a realistic stratosphere. The Brewer-Dobson circulation has been shown to play a role in driving the variability of global stratosphere-troposphere exchange (e.g. Hegglin and Shepherd 2009; Neu et al. 2014; Hess et al. 2015), so in the real atmosphere, the mechanisms involving tropospheric RWB must compete with those involving the Brewer Dobson circulation. It would be interesting and worthwhile to evaluate the relative importance of these two mechanisms in the real atmosphere.

One of the most robust results in this thesis is the asymmetry in mixing strength between AWB and CWB. In idealized lifecycle simulations, climate simulations, and reanalysis data, CWB consistently exhibits stronger mixing efficiency than AWB. It is demonstrated in an idealized climate simulation (Chapter 4) that this asymmetry translates into a decrease in total diffusivity in the upper underworld as the jet shifts poleward. However, the importance of this mechanism in the real atmosphere has not been tested. A possible test would be conducting tracer studies in chemical transport models for the southern hemisphere where the atmospheric setup is similar to the idealized climate simulation.

Why CWB exhibits stronger mixing than AWB is an interesting theoretical question. The cross section figures (e.g. Figs. 5.3 and 5.4) suggest the mechanism may be non-barotropic, making the cyclonic lobe in CWB descend lower. From a quasi-geostrophic (QG) perspective, the large-scale vertical motion is mainly determined by advection of absolute vorticity which might explain the

difference between AWB and CWB in the extent of descending vertical motion. Appropriately designed idealized simulations may shed more light on this.

This thesis focuses only on tropospheric climate variability impacting RWB and the related transport and mixing. It is known that stratospheric variability strongly influences the tropospheric jet and RWB occurrence as well. For example, sudden stratospheric warmings can lead to an equatorward shift of the jet stream and storm tracks in the northern hemisphere (e.g. Baldwin and Dunkerton 2001). Based on this thesis study, such an influence is expected to project onto a change in large-scale transport, both within the troposphere and across the tropopause. Since sudden stratospheric warmings are important sources of intraseasonal predictability, studying this linkage would likely benefit the prediction of the large-scale distribution of various constituents.

RWB may be used to explain some of the biases of tracer distributions in free running GCMs. For example, GCMs have an equatorward bias in the jet latitude (Kidston and Gerber 2010; Barnes and Polvani 2013). The bias in the jet latitude may translate into a bias in RWB frequency of occurrence which, based on our study, is essential for realistically simulating the large-scale transport and mixing. In addition, if the asymmetry between AWB and CWB mixing strength is not accurately represented, the model might suffer from a bias in total mixing as well. Much more research awaits to understand the model bias/spread of large-scale transport in light of this RWB-circulation relationship.

REFERENCES

Abalos, M., B. Legras, and E. Shuckburgh, 2016: Interannual variability in effective diffusivity in the upper troposphere/lower stratosphere from reanalysis data. *Quarterly Journal of the Royal Meteorological Society*, **142 (697)**, 1847–1861.

Albers, J. R., et al., 2017: Mechanisms governing interannual stratosphere to troposphere ozone transport. *Journal of Geophysical Research*, **submitted**.

Añel, J. A., J. C. Antuna, L. de la Torre, J. M. Castanheira, and L. Gimeno, 2008: Climatological features of global multiple tropopause events. *Journal of Geophysical Research: Atmospheres*, **113 (D7)**.

Añel, J. A., L. de la Torre, and L. Gimeno, 2012: On the origin of the air between multiple tropopauses at midlatitudes. *The Scientific World Journal*, **2012**.

Appenzeller, C., H. Davies, and W. Norton, 1996a: Fragmentation of stratospheric intrusions. *J. Geophys. Res.*, **101 (D1)**, 1435–1456.

Appenzeller, C. and H. C. Davies, 1992: Structure of stratospheric intrusions into the troposphere. *Nature*, **358 (6387)**, 570–572, URL http://dx.doi.org/10.1038/358570a0.

Appenzeller, C., J. R. Holton, and K. H. Rosenlof, 1996b: Seasonal variation of mass transport across the tropopause. *Journal of Geophysical Research: Atmospheres*, **101 (D10)**, 15 071–15 078.

Baldwin, M. P. and T. J. Dunkerton, 2001: Stratospheric harbingers of anomalous weather regimes. *Science*, **294 (5542)**, 581–584.

Barnes, E. A. and D. L. Hartmann, 2010: Influence of eddy-driven jet latitude on north atlantic jet persistence and blocking frequency in cmip3 integrations. *Geophysical Research Letters*, **37 (23)**, doi:10.1029/2010GL045700, URL http://dx.doi.org/10.1029/2010GL045700, l23802.

Barnes, E. A. and D. L. Hartmann, 2012: Detection of rossby wave breaking and its response to shifts of the midlatitude jet with climate change. *Journal of Geophysical Research: Atmospheres*, **117 (D9)**, doi:10.1029/2012JD017469, URL http://dx.doi.org/10.1029/2012JD017469, d09117.

Barnes, E. A. and L. Polvani, 2013: Response of the midlatitude jets, and of their variability, to increased greenhouse gases in the CMIP5 models. *Journal of Climate*, **26 (18)**, 7117–7135.

Barnes, E. A., J. Slingo, and T. Woollings, 2012: A methodology for the comparison of blocking climatologies across indices, models and climate scenarios. *Climate dynamics*, **38 (11-12)**,

2467–2481.

Barnston, A. G. and R. E. Livezey, 1987: Classification, seasonality and persistence of low-frequency atmospheric circulation patterns. *Monthly weather review*, **115 (6)**, 1083–1126.

Barrie, L. A., 1986: Arctic air pollution: an overview of current knowledge. *Atmospheric Environment (1967)*, **20 (4)**, 643–663.

Bekryaev, R. V., I. V. Polyakov, and V. A. Alexeev, 2010: Role of polar amplification in long-term surface air temperature variations and modern Arctic warming. *Journal of Climate*, **23 (14)**, 3888–3906.

Bengtsson, L., K. I. Hodges, S. Koumoutsaris, M. Zahn, and N. Keenlyside, 2011: The changing atmospheric water cycle in polar regions in a warmer climate. *Tellus A*, **63 (5)**, 907–920.

Berrisford, P., B. Hoskins, and E. Tyrlis, 2007: Blocking and Rossby wave breaking on the dynamical tropopause in the Southern Hemisphere. *J. Atmos. Sci.*, **64 (8)**, 2881–2898.

Birner, T., 2006: Fine-scale structure of the extratropical tropopause region. *Journal of Geophysical Research: Atmospheres*, **111 (D4)**.

Birner, T., 2010: Residual circulation and tropopause structure. *J. Atmos. Sci.*, **67 (8)**, 2582–2600.

Birner, T., A. Dörnbrack, and U. Schumann, 2002: How sharp is the tropopause at midlatitudes? *Geophysical research letters*, **29 (14)**.

Birner, T., D. J Thompson, and T. Shepherd, 2013: Up-gradient eddy fluxes of potential vorticity near the subtropical jet. *Geophys. Res. Lett.*, **40 (22)**, 5988–5993.

Birner, T., D. Sankey, and T. Shepherd, 2006: The tropopause inversion layer in models and analyses. *Geophysical research letters*, **33 (14)**.

Butchart, N. and E. E. Remsberg, 1986: The area of the stratospheric polar vortex as a diagnostic for tracer transport on an isentropic surface. *J. Atmos. Sci.*, **43 (13)**, 1319–1339.

Butler, A. H., D. W. Thompson, and R. Heikes, 2010: The steady-state atmospheric circulation response to climate change-like thermal forcings in a simple general circulation model. *Journal of Climate*, **23 (13)**, 3474–3496.

Castanheira, J. and L. Gimeno, 2011: Association of double tropopause events with baroclinic waves. *Journal of Geophysical Research: Atmospheres*, **116 (D19)**.

Castanheira, J., T. Peevey, C. Marques, and M. Olsen, 2012: Relationships between brewer-dobson circulation, double tropopauses, ozone and stratospheric water vapour. *Atmospheric Chemistry and Physics*, **12 (21)**, 10 195–10 208.

Chapman, W. L. and J. E. Walsh, 1993: Recent variations of sea ice and air temperature in high latitudes. *Bulletin of the American Meteorological Society*, **74 (1)**, 33–47.

Chen, G. and A. Plumb, 2014: Effective isentropic diffusivity of tropospheric transport. *J. Atmos. Sci.*, **71 (9)**, 3499–3520.

Chen, P., 1995: Isentropic cross-tropopause mass exchange in the extratropics. *J. Geophys. Res.*, **100 (D8)**, 16 661–16 673.

Chen, W. Y. and H. M. van den Dool, 1999: Significant change of extratropical natural variability and potential predictability associated with the El Nino/Southern Oscillation. *Tellus A*, **51 (5)**, 790–802.

Curry, J., J. Schramm, M. Serreze, and E. Ebert, 1995: Water vapor feedback over the Arctic Ocean. *J. Geophys. Res.*, **100 (D7)**, 14 223–14 229.

Davey, M., et al., 2002: Stoic: a study of coupled model climatology and variability in tropical ocean regions. *Climate Dynamics*, **18 (5)**, 403–420.

Davies, F. J., H. Renssen, and H. Goosse, 2014: The Arctic freshwater cycle during a naturally and an anthropogenically induced warm climate. *Climate Dynamics*, 1–14.

Dee, D., et al., 2011: The ERA-Interim reanalysis: Configuration and performance of the data assimilation system. *Quarterly Journal of the Royal Meteorological Society*, **137 (656)**, 553–597.

Doyle, J., G. Lesins, C. Thackray, C. Perro, G. Nott, T. Duck, R. Damoah, and J. Drummond, 2011: Water vapor intrusions into the High Arctic during winter. *Geophysical Research Letters*, **38 (12)**.

Eckhardt, S., A. Stohl, H. Wernli, P. James, C. Forster, and N. Spichtinger, 2004: A 15-year climatology of warm conveyor belts. *Journal of climate*, **17 (1)**, 218–237.

Edouard, S., R. Vautard, and G. Brunet, 1997: On the maintenance of potential vorticity in isentropic coordinates. *Quart. J. Roy. Meteorol. Soc.*, **123 (543)**, 2069–2094.

Ferreira, A., J. Castanheira, and L. Gimeno, 2015: Water vapour stratification and dynamical warming behind the sharpness of the earth's midlatitude tropopause. *Quarterly Journal of the Royal Meteorological Society*.

Forster, F., M. Piers, and K. P. Shine, 1997: Radiative forcing and temperature trends from stratospheric ozone changes. *Journal of Geophysical Research: Atmospheres*, **102 (D9)**, 10 841–10 855.

Francis, J. A. and E. Hunter, 2006: New insight into the disappearing Arctic sea ice. *Eos, Transactions American Geophysical Union*, **87 (46)**, 509–511.

Gelaro, R., et al., 2017: The modern-era retrospective analysis for research and applications, version 2 (merra-2). *Journal of Climate*, **(2017)**.

Graversen, R. G. and M. Wang, 2009: Polar amplification in a coupled climate model with locked albedo. *Climate Dynamics*, **33 (5)**, 629–643.

Hansen, J., et al., 2005: Efficacy of climate forcings. *J. Geophys. Res.*, **110 (D18)**.

Haynes, P. and E. Shuckburgh, 2000a: Effective diffusivity as a diagnostic of atmospheric transport: 1. stratosphere. *J. Geophys. Res.*, **105 (D18)**, 22 777–22 794.

Haynes, P. and E. Shuckburgh, 2000b: Effective diffusivity as a diagnostic of atmospheric transport: 2. troposphere and lower stratosphere. *J. Geophys. Res.*, **105 (D18)**, 22 795–22 810, doi:10.1029/2000JD900092, URL `http://dx.doi.org/10.1029/2000JD900092`.

Hegglin, M. I. and T. G. Shepherd, 2009: Large climate-induced changes in ultraviolet index and stratosphere-to-troposphere ozone flux. *Nature Geoscience*, **2 (10)**, 687–691.

Held, I. M. and M. J. Suarez, 1994: A proposal for the intercomparison of the dynamical cores of atmospheric general circulation models. *Bull. Amer. Meteor. Soc.*, **75 (10)**, 1825–1830.

Hess, P., D. Kinnison, and Q. Tang, 2015: Ensemble simulations of the role of the stratosphere in the attribution of northern extratropical tropospheric ozone variability. *Atmospheric Chemistry and Physics*, **15 (5)**, 2341–2365.

Holland, M. M. and C. M. Bitz, 2003: Polar amplification of climate change in coupled models. *Climate Dynamics*, **21 (3-4)**, 221–232.

Holton, J. R., P. H. Haynes, M. E. McIntyre, A. R. Douglass, R. B. Rood, and L. Pfister, 1995: Stratosphere-troposphere exchange. *Reviews of Geophysics*, **33 (4)**, 403–439.

Homeyer, C. R., K. P. Bowman, L. L. Pan, E. L. Atlas, R.-S. Gao, and T. L. Campos, 2011: Dynamical and chemical characteristics of tropospheric intrusions observed during start08. *Journal of Geophysical Research: Atmospheres*, **116 (D6)**.

Hoskins, B. J., 1991: Towards a PV-θ view of the general circulation. *Tellus A*, **43 (4)**, 27–35.

Jing, P., D. Cunnold, H. Wang, and E. Yang, 2004: Isentropic cross-tropopause ozone transport in the northern hemisphere. *J. Atmos. Sci.*, **61 (9)**, 1068–1078.

Kattsov, V. M. and J. E. Walsh, 2000: Twentieth-century trends of Arctic precipitation from observational data and a climate model simulation. *Journal of Climate*, **13 (8)**, 1362–1370.

Kidston, J. and E. Gerber, 2010: Intermodel variability of the poleward shift of the austral jet stream in the CMIP3 integrations linked to biases in 20th century climatology. *Geophysical Research Letters*, **37 (9)**.

Kochanski, A., 1955: Cross sections of the mean zonal flow and temperature along 8o w. *Journal of Meteorology*, **12 (2)**, 95–106.

Kug, J.-S., D.-H. Choi, F.-F. Jin, W.-T. Kwon, and H.-L. Ren, 2010: Role of synoptic eddy feedback on polar climate responses to the anthropogenic forcing. *Geophysical Research Letters*, **37 (14)**.

Kunkel, D., P. Hoor, and V. Wirth, 2016: The tropopause inversion layer in baroclinic life-cycle experiments: the role of diabatic processes. *Atmospheric Chemistry and Physics*, **16 (2)**, 541–560.

Langford, A., 1999: Stratosphere-troposphere exchange at the subtropical jet: Contribution to the tropospheric ozone budget at midlatitudes. *Geophysical research letters*, **26 (16)**, 2449–2452.

Langford, A., T. O'Leary, C. Masters, K. Aikin, and M. Proffitt, 1998: Modulation of middle and upper tropospheric ozone at northern midlatitudes by the el niño/southern oscillation. *Geophysical research letters*, **25 (14)**, 2667–2670.

Latif, M., A. Sterl, E. Maier-Reimer, and M. Junge, 1993: Climate variability in a coupled GCM. Part I: The tropical Pacific. *Journal of climate*, **6 (1)**, 5–21.

Leibensperger, E. M. and R. A. Plumb, 2014: Effective diffusivity in baroclinic flow. *Journal of the Atmospheric Sciences*, **71 (3)**, 972–984.

Lelieveld, J. and F. J. Dentener, 2000: What controls tropospheric ozone? *J. Geophys. Res.*, **105 (D3)**, 3531–3551.

Lin, M., A. M. Fiore, L. W. Horowitz, A. O. Langford, S. J. Oltmans, D. Tarasick, and H. E. Rieder, 2015: Climate variability modulates western us ozone air quality in spring via deep stratospheric intrusions. *Nature communications*, **6**.

Lin, M., et al., 2012: Springtime high surface ozone events over the western united states: Quantifying the role of stratospheric intrusions. *Journal of Geophysical Research: Atmospheres*, **117 (D21)**.

Liou, Y.-A., A. G. Pavelyev, S.-F. Liu, A. A. Pavelyev, N. Yen, C.-Y. Huang, and C.-J. Fong, 2007: Formosat-3/cosmic gps radio occultation mission: Preliminary results. *IEEE Transactions on Geoscience and Remote Sensing*, **45 (11)**, 3813–3826.

Lippmann, M., 1989: Health effects of ozone a critical review. *Japca*, **39 (5)**, 672–695.

Liu, C. and E. Barnes, 2017a: Quantifying isentropic mixing in a modified Lagrangian coordinate: Applications to Rossby wave breaking. *Journal of the Atmospheric Sciences*, **submitted**.

Liu, C. and E. A. Barnes, 2015: Extreme moisture transport into the Arctic linked to Rossby wave breaking. *J. Geophys. Res.*, **120 (9)**, 3774–3788.

Liu, C. and E. A. Barnes, 2017b: Synoptic formation of double tropopauses. *Journal of Geophysical Research*, **submitted**.

Liu, C., X. Ren, and X. Yang, 2014: Mean flow-storm track relationship and Rossby wave breaking in two types of El-Niño. *Adv. Atmos. Sci.*, **31 (1)**, 197–210.

Liu, J., J. A. Curry, H. Wang, M. Song, and R. M. Horton, 2012: Impact of declining Arctic sea ice on winter snowfall. *Proceedings of the National Academy of Sciences*, **109 (11)**, 4074–4079.

Madonna, E., H. Wernli, H. Joos, and O. Martius, 2014: Warm conveyor belts in the ERA-Interim dataset (1979–2010). Part I: Climatology and potential vorticity evolution. *J. Climate*, **27 (1)**, 3–26.

Manabe, S. and R. J. Stouffer, 1980: Sensitivity of a global climate model to an increase of CO2 concentration in the atmosphere. *Journal of Geophysical Research: Oceans (1978–2012)*, **85 (C10)**, 5529–5554.

Manabe, S. and R. T. Wetherald, 1975: The effects of doubling the CO2 concentration on the climate of a general circulation model. **32 (3–15)**.

Masato, G., B. Hoskins, and T. J. Woollings, 2012: Wave-breaking characteristics of midlatitude blocking. *Quarterly Journal of the Royal Meteorological Society*, **138 (666)**, 1285–1296.

McIntyre, M., 1980: Towards a lagrangian-mean description of stratospheric circulations and chemical transports. *Philosophical Transactions of the Royal Society of London A: Mathematical, Physical and Engineering Sciences*, **296 (1418)**, 129–148.

Miller, R., G. Schmidt, and D. Shindell, 2006: Forced annular variations in the 20th century Intergovernmental Panel on Climate Change Fourth Assessment Report models. *J. Geophys. Res.*, **111 (D18)**.

Monahan, A. H. and J. C. Fyfe, 2006: On the nature of zonal jet EOFs. *Journal of climate*, **19 (24)**, 6409–6424.

Nakamura, N., 1995: Modified lagrangian-mean diagnostics of the stratospheric polar vortices. part I. Formulation and analysis of GFDL SKYHI GCM. *J. Atmos. Sci.*, **52 (11)**, 2096–2108.

Nakamura, N., 1996: Two-dimensional mixing, edge formation, and permeability diagnosed in an area coordinate. *J. Atmos. Sci.*, **53 (11)**, 1524–1537.

Nakamura, N., 2004: Quantifying asymmetric wave breaking and two-way transport. *J. Atmos. Sci.*, **61 (22)**, 2735–2748.

Nakamura, N. and D. Zhu, 2010: Finite-amplitude wave activity and diffusive flux of potential vorticity in eddy-mean flow interaction. *J. Atmos. Sci.*, **67 (9)**, 2701–2716.

Neelin, J., et al., 1992: Tropical air-sea interaction in general circulation models. *Climate Dynamics*, **7 (2)**, 73–104.

Neu, J. L., T. Flury, G. L. Manney, M. L. Santee, N. J. Livesey, and J. Worden, 2014: Tropospheric ozone variations governed by changes in stratospheric circulation. *Nature Geoscience*, **7 (5)**, 340.

Newman, M., G. N. Kiladis, K. M. Weickmann, F. M. Ralph, and P. D. Sardeshmukh, 2012: Relative contributions of synoptic and low-frequency eddies to time-mean atmospheric moisture transport, including the role of atmospheric rivers. *Journal of Climate*, **25 (21)**, 7341–7361.

Orbe, C., P. A. Newman, D. W. Waugh, M. Holzer, L. D. Oman, F. Li, and L. M. Polvani, 2015: Air-mass origin in the Arctic. Part II: Response to increases in greenhouse gases. *J. Climate*, **28 (23)**, 9105–9120.

Pan, L. L., et al., 2009: Tropospheric intrusions associated with the secondary tropopause. *Journal of Geophysical Research: Atmospheres*, **114 (D10)**, doi:10.1029/2008JD011374, URL `http://dx.doi.org/10.1029/2008JD011374`, d10302.

Payne, A. E. and G. Magnusdottir, 2014: Dynamics of landfalling atmospheric rivers over the North Pacific in 30 years of MERRA reanalysis. *Journal of Climate*, **(2014)**.

Peevey, T., J. Gille, C. Homeyer, and G. Manney, 2014: The double tropopause and its dynamical relationship to the tropopause inversion layer in storm track regions. *Journal of Geophysical Research: Atmospheres*, **119 (17)**.

Peevey, T. R., J. C. Gille, C. E. Randall, and A. Kunz, 2012: Investigation of double tropopause spatial and temporal global variability utilizing high resolution dynamics limb sounder temperature observations. *Journal of Geophysical Research: Atmospheres*, **117 (D1)**.

Pelly, J. L. and B. J. Hoskins, 2003: A new perspective on blocking. *Journal of the atmospheric sciences*, **60 (5)**, 743–755.

Plumb, R. and J. Mahlman, 1987: The zonally averaged transport characteristics of the gfdl general circulation/transport model. *Journal of the atmospheric sciences*, **44 (2)**, 298–327.

Polvani, L. M. and J. G. Esler, 2007: Transport and mixing of chemical air masses in idealized baroclinic life cycles. *Journal of Geophysical Research: Atmospheres*, **112 (D23)**, doi:10.1029/2007JD008555, URL `http://dx.doi.org/10.1029/2007JD008555`, d23102.

Raatz, W. E. and G. E. Shaw, 1984: Long-range tropospheric transport of pollution aerosols into the alaskan arctic. *Journal of Climate and Applied Meteorology*, **23 (7)**, 1052–1064.

Randel, W. J., D. J. Seidel, and L. L. Pan, 2007a: Observational characteristics of double tropopauses. *Journal of Geophysical Research: Atmospheres*, **112 (D7)**, doi: 10.1029/2006JD007904, URL `http://dx.doi.org/10.1029/2006JD007904`, d07309.

Randel, W. J., F. Wu, and P. Forster, 2007b: The extratropical tropopause inversion layer: Global observations with GPS data, and a radiative forcing mechanism. *Journal of the Atmospheric Sciences*, **64 (12)**, 4489–4496.

Rasmusson, E. M. and J. M. Wallace, 1983: Meteorological aspects of the El Nino/Southern Oscillation. *Science*, **222 (4629)**, 1195–1202.

Ren, X., Y. Zhang, and Y. Xiang, 2008: Connections between wintertime jet stream variability, oceanic surface heating, and transient eddy activity in the north pacific. *Journal of Geophysical Research: Atmospheres*, **113 (D21)**, doi:10.1029/2007JD009464, URL `http://dx.doi.org/10.1029/2007JD009464`, d21119.

Rienecker, M. M., et al., 2011: MERRA: NASA's modern-era retrospective analysis for research and applications. *Journal of Climate*, **24 (14)**, 3624–3648.

Riese, M., F. Ploeger, A. Rap, B. Vogel, P. Konopka, M. Dameris, and P. Forster, 2012: Impact of uncertainties in atmospheric mixing on simulated utls composition and related radiative effects. *Journal of Geophysical Research: Atmospheres*, **117 (D16)**.

Rinke, A., C. Melsheimer, K. Dethloff, and G. Heygster, 2009: Arctic total water vapor: comparison of regional climate simulations with observations, and simulated decadal trends. *Journal of Hydrometeorology*, **10 (1)**, 113–129.

Rivière, G., 2011: A dynamical interpretation of the poleward shift of the jet streams in global warming scenarios. *J. Atmos. Sci.*, **68 (6)**, 1253–1272.

Ryoo, J.-M., Y. Kaspi, D. W. Waugh, G. N. Kiladis, D. E. Waliser, E. J. Fetzer, and J. Kim, 2013: Impact of Rossby wave breaking on US west coast winter precipitation during ENSO events. *Journal of Climate*, **26 (17)**, 6360–6382.

Schwartz, M., G. Manney, M. Hegglin, N. Livesey, M. Santee, and W. Daffer, 2015: Climatology and variability of trace gases in extratropical double-tropopause regions from mls, hirdls, and ace-fts measurements. *Journal of Geophysical Research: Atmospheres*, **120 (2)**, 843–867.

Seidel, D. J. and W. J. Randel, 2006: Variability and trends in the global tropopause estimated from radiosonde data. *Journal of Geophysical Research: Atmospheres*, **111 (D21)**.

Serreze, M. C., R. G. Barry, and J. E. Walsh, 1995: Atmospheric water vapor characteristics at 70 N. *Journal of Climate*, **8 (4)**, 719–731.

Shapiro, M., 1980: Turbulent mixing within tropopause folds as a mechanism for the exchange of chemical constituents between the stratosphere and troposphere. *J. Atmos. Sci.*, **37 (5)**, 994–1004.

Shaw, N. and E. Austin, 1930: Manual of meteorology, vol. 3: the physical processes of weather. Cambridge University Press.

Singarayer, J. S., J. L. Bamber, and P. J. Valdes, 2006: Twenty-first-century climate impacts from a declining Arctic sea ice cover. *Journal of Climate*, **19 (7)**, 1109–1125.

Škerlak, B., M. Sprenger, S. Pfahl, E. Tyrlis, and H. Wernli, 2015: Tropopause folds in era-interim: Global climatology and relation to extreme weather events. *Journal of Geophysical Research: Atmospheres*, **120 (10)**, 4860–4877.

Skerlak, B., M. Sprenger, and H. Wernli, 2014: A global climatology of stratosphere-troposphere exchange using the era-interim data set from 1979 to 2011. *Atmospheric Chemistry and Physics*, **14 (2)**, 913.

Skific, N. and J. A. Francis, 2013: Drivers of projected change in arctic moist static energy transport. *Journal of Geophysical Research: Atmospheres*, **118 (7)**, 2748–2761.

Skific, N., J. A. Francis, and J. J. Cassano, 2009a: Attribution of projected changes in atmospheric moisture transport in the Arctic: A self-organizing map perspective. *Journal of Climate*, **22 (15)**, 4135–4153.

Skific, N., J. A. Francis, and J. J. Cassano, 2009b: Attribution of seasonal and regional changes in Arctic moisture convergence. *Journal of Climate*, **22 (19)**, 5115–5134.

Solomon, S., K. H. Rosenlof, R. W. Portmann, J. S. Daniel, S. M. Davis, T. J. Sanford, and G.-K. Plattner, 2010: Contributions of stratospheric water vapor to decadal changes in the rate of global warming. *Science*, **327 (5970)**, 1219–1223.

Son, S.-W., N. F. Tandon, and L. M. Polvani, 2011: The fine-scale structure of the global tropopause derived from cosmic gps radio occultation measurements. *Journal of Geophysical Research: Atmospheres*, **116 (D20)**.

Sprenger, M. and H. Wernli, 2003: A northern hemispheric climatology of cross-tropopause exchange for the era15 time period (1979–1993). *Journal of Geophysical Research: Atmospheres*, **108 (D12)**.

Stone, E. M., W. J. Randel, and J. L. Stanford, 1999: Transport of passive tracers in baroclinic wave life cycles. *Journal of the atmospheric sciences*, **56 (10)**, 1364–1381.

Stramler, K., A. D. Del Genio, and W. B. Rossow, 2011: Synoptically driven Arctic winter states. *Journal of Climate*, **24 (6)**, 1747–1762.

Strong, C. and G. Magnusdottir, 2008: Tropospheric Rossby wave breaking and the NAO/NAM. *J. Atmos. Sci.*, **65 (9)**, 2861–2876.

Swart, N. and J. Fyfe, 2012: Observed and simulated changes in the Southern Hemisphere surface westerly wind-stress. *Geophysical Research Letters*, **39 (16)**.

Thompson, D. W. and S. Solomon, 2002: Interpretation of recent southern hemisphere climate change. *Science*, **296 (5569)**, 895–899.

Thorncroft, C., B. Hoskins, and M. McIntyre, 1993: Two paradigms of baroclinic-wave life-cycle behaviour. *Quart. J. Roy. Meteorol. Soc.*, **119 (509)**, 17–55.

Trepte, C. R., R. E. Veiga, and M. P. McCormick, 1993: The poleward dispersal of mount pinatubo volcanic aerosol. *J. Geophys. Res.*, **98 (D10)**, 18 563–18 573.

U.S. Environmental Protection Agency (U.S. EPA), 2006: Air quality criteria for ozone and related photoche mical oxidants (2006 final).

Walker, C. C. and T. Schneider, 2006: Eddy influences on Hadley circulations: Simulations with an idealized GCM. *Journal of the atmospheric sciences*, **63 (12)**, 3333–3350.

Wang, S. and L. M. Polvani, 2011: Double tropopause formation in idealized baroclinic life cycles: The key role of an initial tropopause inversion layer. *Journal of Geophysical Research: Atmospheres*, **116 (D5)**, doi:10.1029/2010JD015118, URL http://dx.doi.org/10.1029/2010JD015118, d05108.

Wargan, K., G. Labow, S. Frith, S. Pawson, N. Livesey, and G. Partyka, 2017: Evaluation of the ozone fields in nasa?s merra-2 reanalysis. *Journal of Climate*, **30 (8)**, 2961–2988.

Waugh, D. W., 2005: Impact of potential vorticity intrusions on subtropical upper tropospheric humidity. *Journal of Geophysical Research: Atmospheres*, **110 (D11)**.

Waugh, D. W. and L. M. Polvani, 2000: Climatology of intrusions into the tropical upper troposphere. *Geophysical Research Letters*, **27 (23)**, 3857–3860.

Wickert, J., G. Beyerle, R. König, S. Heise, L. Grunwaldt, G. Michalak, C. Reigber, and T. Schmidt, 2005: Gps radio occultation with champ and grace: A first look at a new and promising satellite configuration for global atmospheric sounding. *Annales Geophysicae*, **23 (3)**, 653–658, doi:10.5194/angeo-23-653-2005, URL http://www.ann-geophys.net/23/653/2005/.

Winton, M., 2006: Amplified Arctic climate change: What does surface albedo feedback have to do with it? *Geophysical Research Letters*, **33 (3)**.

Wirth, V., 2001: Cyclone–anticyclone asymmetry concerning the height of the thermal and the dynamical tropopause. *Journal of the atmospheric sciences*, **58 (1)**, 26–37.

Wittman, M. A., A. J. Charlton, and L. M. Polvani, 2005: On the meridional structure of annular modes. *Journal of climate*, **18 (12)**, 2119–2122.

Woods, C., R. Caballero, and G. Svensson, 2013: Large-scale circulation associated with moisture intrusions into the Arctic during winter. *Geophysical Research Letters*, **40 (17)**, 4717–4721, doi:10.1002/grl.50912.

Woollings, T., A. Hannachi, and B. Hoskins, 2010: Variability of the North Atlantic eddy-driven jet stream. *Quarterly Journal of the Royal Meteorological Society*, **136 (649)**, 856–868.

Woollings, T., B. Hoskins, M. Blackburn, and P. Berrisford, 2008: A new Rossby wave-breaking interpretation of the North Atlantic Oscillation. *J. Atmos. Sci.*, **65 (2)**, 609–626.

World Meteorological Organization, W., 1957: A three-dimensional science: Second session of the commission for aerology. *WMO Bull*, **4 (2)**, 134–138.

Yang, H., G. Chen, Q. Tang, and P. Hess, 2016: Quantifying isentropic stratosphere-troposphere exchange of ozone. *Journal of Geophysical Research: Atmospheres*, **121 (7)**, 3372–3387, doi:10.1002/2015JD024180, URL `http://dx.doi.org/10.1002/2015JD024180`, 2015JD024180.

Yin, J. H., 2005: A consistent poleward shift of the storm tracks in simulations of 21st century climate. *Geophysical Research Letters*, **32 (18)**.

A.1. QUANTIFICATION OF ϕ_A^{DIFF} AND ϕ_A^{MEAN}

To quantify the advection patterns corresponding to each GPS profile, ERA-Interim data is used to calculate the equivalent latitude anomaly profile $\phi_a(\theta)$ colocated with the GPS profiles. By summing and subtracting ϕ_a in the vertical direction, we isolate two aspects of the advection patterns – differential advection (ϕ_a^{diff}) and mean advection (ϕ_a^{mean}), respectively. Differential advection represents the shear of advection in meridional plane and is calculated as:

$$\phi_a^{diff} = \frac{\phi_a(380K) - \phi_a(\theta_{TP})}{380K - \theta_{TP}} \tag{A.1}$$

where θ_{TP} is the potential temperature θ at the first tropopause. $380K$ is used here for an upper level above the first tropopause. The result is not sensitive as we vary this value between 380K and 450K (not shown).

The mean advection represents the average advection direction above the lowest tropopause and is calculated as:

$$\phi_a^{mean} = \frac{\phi_a(380K) + \phi_a(\theta_{TP})}{2} \tag{A.2}$$

Positive values denote poleward mean advection and negative values denote equatorward mean advection.